FINE SCALE REMOTE SENSING OF FOREST STRUCTURE AND CONDITION

Jonathan Lamont Batchelor

A dissertation

submitted in partial fulfillment of the

requirements for the degree of

Doctor of Philosophy

University of Washington

2023

Reading Committee:

L. Monika Moskal, Chair

Andrew T. Hudak

Ernesto Alvarado

Program Authorized to Offer Degree:

School of Environmental and Forest Sciences

University of Washington

Abstract

Fine Scale Remote Sensing of Forest Structure and Condition

Jonathan Lamont Batchelor

Chair of the Supervisory Committee:
L. Monika Moskal
School of Environmental and Forest Sciences

Forest structure refers to the three-dimensional arrangement of biophysical elements (i.e., vegetation) within a forested landscape, whereas forest condition is the characteristics of biophysical elements that are not directly related to the physical arrangement. Condition can relate to measurable quantities such as moisture content. Disturbances in forest structure, such as fire consuming woody vegetation, can result in changes to the condition of the vegetation, such as charring and reduced photosynthesis ability due to scorched leaves. Quantifying both forest structure and condition is crucial for answering a variety of ecological questions. Utilizing remote sensing techniques such as drone imagery and terrestrial lidar allows for the quantification of fine scale ecological processes and changes at a scale where direct measurement is possible.

This interdisciplinary dissertation examined three ecological questions related to forest structure and condition. The first question, “Can lidar detect changes in moisture content of potential fire fuels?”, used terrestrial lidar and field spectrometers to measure changes in surface reflectance of dead litter beds as they dried. Moisture content plays a crucial role in determining flammability and this first inquiry presents novel methods for quantifying the moisture content of leaf litter beds using laser pulses from terrestrial lidar scanners. The second question, “Can drone digital aerial photogrammetry be used to quantify fire effect in three-dimensions?”, explored the utility of multispectral drone imagery to generate three-dimensional photogrammetric point clouds to quantify fire effects at different canopy height strata, and to compare drone estimates of fire

effects to satellite-derived estimates. The third question, “How can terrestrial lidar be used to quantify habitat, and then upscale those estimates to region wide models using machine learning?”, utilized terrestrial lidar scans to quantify forest structure and viewshed in the understory to first identify areas that met habitat requirements for Canada lynx (Lynx canadensis), and then to use XGboost machine learning algorithms to produce region-wide habitat models using aerial lidar.

The unifying theme through these three questions, and the core of this dissertation, is the utilization of fine-scale remote sensing methods to quantify the structure and condition of forested systems to address ecological questions in an interdisciplinary manner.

TABLE OF CONTENTS

List of Figures

List of Tables

Acknowledgements

This work would not have been possible without the help and contribution of many people at the University of Washington and beyond. Thanks to all the faculty and staff that answered my many questions when I would show up at their doors unannounced. Thanks to the members of the Remote Sensing and Geospatial Analysis Lab, the Forest Resilience Lab, and the FLAME lab for working and collaborating with me on these, and many other projects. A huge thank you to my committee members and co-authors that collaborated with me and who inspired me to ask and refine questions.

Funding for this work was provided by: UW Precision Forestry Cooperative, Washington Cooperative Fish and Wildlife Research Unit, Washington Department of Natural Resources, USFS PNW Research Station and the Joint Fire Science Program, Stand Management Cooperative, and U.S. Department of Defense Strategic Environmental Research and Development Program Project.

Chapter 1. Introduction

1.1 Fine Scale Remote Sensing

Remote sensing is the process of measuring a quantifiable variable without physically touching an object. Typically, remote sensing is associated with airborne or spaceborne sensors that gather information about the Earth's surface, and many definitions of remote sensing limit the science to only utilizing sensor data from nadir elevated perspectives (Campbell and Wynne, 2011). While overhead imagery from aircraft and satellites has (and will continue to) provided valuable information about the earth, such platforms are limited by the resolution they are capable of producing. Currently, submeter-resolution satellite imagery is available and utilized in various environmental remote sensing applications (Li et al., 2021; Sharma, 2022; Wang et al., 2019). Additionally, airborne lidar has become an essential tool for ecological monitoring and forest characterization. Unlike aerial and satellite imagery, which provides a two-dimensional top-down view of the landscape, lidar can penetrate forest canopies through small gaps in the foliage to model midstory structural elements as well as the ground. In many respects, aerial lidar and submeter satellite imagery can be considered fine scale remote sensing. However, for the purpose of this research, fine scale remote sensing is defined more stringently.

Remote sensing data is characterized by several scales: spatial, temporal, spectral, and radiometric resolution. The terms "fine" and "coarse" are used to describe the relative resolution of the data, with "fine" referring to a higher resolution than "coarse." However, the terms "fine" and "coarse" are only meaningful when used in relation to each other. In the context of this research, "fine scale remote sensing" refers to imagery collected via drone with a spatial resolution of a few centimeters and a temporal resolution of data collection before and after a disturbance event. Additionally, "fine scale remote sensing", in the context of this research, includes terrestrial lidar scans that can be used to model, with a high level of fidelity, understory vegetation structure and can rapidly resample (temporal resolution) vegetation to detect changes in its condition. The terminology used to classify the scale of data collection methods, such as "fine" and "coarse," is subjective in nature. However, data collected by drone imagery and terrestrial lidar, in comparison to airborne data, is significant enough to justify referring to them as "fine scale" data, based on their ability to accurately measure forest structure and condition with such high precision.

1.2 Forest Structure

Forest structure can be defined in a multitude of ways. For this body of work, forest structure is considered to be the arrangement and amount of aboveground biophysical components present in a forested landscape (Batchelor et al., 2023b; Lindenmayer and Franklin, 2002). The arrangement and complexity of these biophysical elements has profound effects on the ecological functioning and health of forests (Carey, 2007; Shugart et al., 2010). The forest structural elements explored in this dissertation are canopy closure and occlusion of ground-level vegetation cover, the change in the structure of understory vegetation pre- and post-fire, and quantification of the horizontal viewshed 1.5 m above ground level.

Canopy closure and how it relates to forest health has been studied extensively, and numerous studies have explored how canopy closure and gaps relate to the overall forest structure, light penetration, species habitat, and gap formation (Jennings et al., 1999; Schliemann and Bockheim, 2011; Smith and Ramsay, 2018; Valverde and Silvertown, 1997). That canopy closure is important is well established, however, canopy closure by its very definition occludes the understory from overhead observation (e.g., aerial or spaceborne imagery). This limits the ability to observe and quantify change in the understory. This is a well-known confounding factor for many estimates of fire severity, as a surface fire can potentially consume all vegetation in the understory without moving into the overstory (Hoe et al., 2018; Lentile et al., 2006; Morgan et al., 2014). Top-down imagery, such as aerial and satellite imagery, is limited to observations of the live upper canopy and can potentially miss the fire effect size in the understory. This is less of an issue in areas of a relatively open upper canopy, but even in forested stands that have relatively large gaps between trees, a high percentage of the ground can still be occluded from overhead observation.

Traditionally, understory vegetation structure measurements have required field measurements and observations using methods such as the Composite Burn Index (CBI) to quantify structural changes due to fire (Saberi et al., 2022) or the use of cover boards for more generalized estimations of horizontal cover generally related to habitat characterization (Griffith and Youtie, 1988; Nudds, 1977). Horizontal cover and understory forest structure are key factors in habitat selection for many species, including the Canadian lynx (*Lynx canadensis*) (Batchelor et al., 2023a; Murray et al., 1994; Vanbianchi et al., 2017). However, field estimations often suffer

from observer bias (Vales and Bunnell, 1988) and the inherently limited spatial extent possible from field observations. Remote sensing technologies such as aerial lidar have been utilized to create landscape-level models from field observations (Fekety et al., 2019), but aerial lidar, while providing more information about forest structure than possible from imagery, has been limited in its utility to model understory vegetation, largely because of the variability in the overstory canopy closure.

1.3 Forest Condition

Forest condition can also be defined in many ways, depending on the discipline and objectives of the observers. Condition, in relation to this research, is defined as the characteristics of the biophysical components that are not directly related to the three-dimensional structure. Examples of condition can be the moisture content of potential fire fuels or the reflectance values of vegetation surfaces before and after a fire. Condition in this context is directly related to fire as either a potential future disturbance (i.e., flammability of litter beds and moisture content), or the condition of vegetation post fire compared to pre fire. While fire inevitably leads to a change in forest structure as vegetation is consumed, the change in electromagnetic radiation reflectance values is a measurement in the condition change of the vegetation. This change in reflectance values at defined wavelengths is how many indices of burn severity, such as the differenced normalized burn ratio (dNBR) or the differenced normalized difference vegetation index (dNDVI), are used to derive their estimated values. While a change in structure due to disturbance is usually accompanied by a change in reflectance values (Kato et al., 2019), a change in one does not inherently imply a change in the other. For example, water content or stress in vegetation can eventually lead to a change in structure, but initial changes in water content can have little to no discernable effects on the actual structure.

The water content of vegetation is a topic that has been extensively researched because water stress can cause significant changes in composition and structure of vegetation. Monitoring the water content of vegetation using lidar intensity values is a relatively new method that can link the condition of vegetation to structural measurements (Junttila et al., 2019). Rapid repeat measurements of moisture content are possible using fixed-location lidar scanners (Junttila et al., 2021), and this method has been effectively used to monitor changes in live vegetation moisture content. However, leveraging this ability to detect changes in the moisture content of dead

potential fire fuels has not yet been explored. Moisture content in dead fuels is controlled by vapor pressure deficit and bulk of cellulose while moisture content in live fuels is controlled by physiology and processes such as evapotranspiration (Matthews, 2014). Even with this difference in how moisture levels are controlled in dead VS live vegetation, the absorption rate of electromagnetic radiation (i.e., a laser pulse from a lidar sensor) by water is constant. Because lidar has been demonstrated to be effective in measuring live fuel moisture content, it is reasonable to explore its utility in quantifying the moisture content of dead fine fuels. Especially because fine fuels, such as leaf litter, can undergo rapid changes in moisture content that can affect the flammability and behavior of fire (Matthews, 2006; Viney, 1991) and lidar offers a rapid way to sample vegetation moisture content in a spatially explicit manner.

1.4 Research Objectives

This dissertation is comprised of three research topics that utilize fine scale remote sensing methods to address current gaps in knowledge and develop novel methods of quantifying forest structure and condition applied to fire and wildlife ecology. In the three chapters, which represent independent research objectives, terrestrial lidar and drone digital aerial photogrammetry (dDAP) are used, and methods are developed specifically to leverage the power of fine scale data. The approach of this research is to apply remote sensing technologies and methodology in an interdisciplinary manner and to work with domain experts in fire and wildlife ecology to address topics relevant to these fields.

1.4.1 *Fuel Moisture Content*

Because moisture content is highly variable in space and time and influences flammability thresholds, field measurements of fuel moisture must be taken before activities such as prescribed burning can occur. A number of methods are used to determine moisture content in the field, such as ground probes and wooden dowels of known dry weight. These methods are limited to point sampling and can miss variations in moisture content owing to vegetation cover or fine scale topography. In this chapter, the principles of using lidar intensity returns to model live vegetation fuel moisture content were applied to dry fuel beds. This chapter details the exploration and establishment of methods that can be used to employ terrestrial lidar scanners to estimate fuel moisture content based on the mean intensity returns as well as the variation in intensity values

within a defined area. Both time-of-flight and phase-shift terrestrial lidar scanners were used to determine whether one type of lidar technology performed better at modeling moisture content. To validate the change in spectral reflectance measured by the lidar scanner, a field spectrometer was used to quantify the change in spectral reflectance at 1550 nm as the material was dried. This was the first study, as far as I am aware, that utilizes lidar to measure moisture content of dead litter beds within a laboratory environment. The results were extremely promising, as they produced regression models with a high level of accuracy. There is a clear pathway forward to continue the work and further develop a methodology using lidar to rapidly sample fuel moisture content with fine spatial and temporal resolutions.

1.4.2 *Fire Effects at Differing Canopy Height Strata*

Separating the effects of fire in the understory from those in the overstory is difficult using aerial and satellite imagery. This can lead to an underestimation of the extent and severity of fire when a live and healthy overstory occludes the burned understory vegetation. Under relatively open understory conditions, low-flying drone imagery can capture normally occluded understory areas at the edges of images. Owing to the radial displacement, a more oblique look angle away from the center of the image frame can capture the ground and understory vegetation directly underneath a tree canopy. Hundreds or thousands of images can be mosaiced together to triangulate camera location at each photo point and then calculate the geometry of all three-dimensional objects (i.e., trees) that were captured in the photograph. The process of generating three-dimensional models from images is often referred to as structure from motion (SfM). For a more precise description, in this dissertation this process is referred to as drone digital aerial photogrammetry (dDAP).

Three-dimensional modeling creates point clouds that retain the spectral information from the parent images. Generating orthoimages and three-dimensional models is a common practice using drone imagery with multiple software available to perform the processing. In this chapter, point clouds are generated from multispectral imagery collected with a drone pre- and post-fire during prescribed burning in a forest with a relatively open understory. This study explores new methods of generating multispectral orthoimages of the understory by digitally removing all overstory vegetation. Fire effects in the understory are effectively separated from those in the overstory. Using multispectral photogrammetric point clouds, it was demonstrated that fire effects

at various canopy height strata can be isolated, and the methods presented allow for a complete classification of ground cover and ground cover changes due to fire.

1.4.3 *Understory Shrub Cover for Habitat Modeling*

The ability to quantify the understory vegetation structure is important for determining the appropriate habitat for many species. Because it is notoriously difficult to model understory structures using aerial imagery and lidar, new methods must be developed to generate metrics from field data collection to inform region-wide models using aerial data. In this chapter, methods that were developed to quantify understory vegetation from single-scan terrestrial lidar data using metrics based on the distance traveled by each individual laser pulse (Batchelor et al., 2023b). There are several advantages to using a single terrestrial lidar scan to derive metrics (Loudermilk et al., 2023). Data collection in the field is much faster, and there is no need to stitch multiple scans together during processing. Each scan can become its own data point used to derive the openness and depth metrics. Using these metrics from single scans to determine areas that meet habitat requirements, machine-learning models can be applied to aerial lidar to identify areas with similar structures. Hundreds of potential metrics can be derived from aerial lidar using point subsets, ratios, or statistical summaries of the point distribution. This research further explored methods of deriving ecologically meaningful metrics from aerial lidar to produce 286 values to determine which metrics were most important for developing XGboost machine learning models to associate aerial lidar metrics with in-field measurements of horizontal cover made from terrestrial lidar.

1.5 References

Batchelor, J.L., Hudak, A.T., Gould, P., Moskal, L.M., 2023a. Terrestrial and Airborne Lidar to Quantify Shrub Cover for Canada Lynx (Lynx canadensis) Habitat Using Machine Learning. Remote Sensing 15, 4434. https://doi.org/10.3390/rs15184434

Batchelor, J.L., Wilson, T.M., Olsen, M.J., Ripple, W.J., 2023b. New Structural Complexity Metrics for Forests from Single Terrestrial Lidar Scans. Remote Sensing 15, 145. https://doi.org/10.3390/rs15010145

Campbell, J.B., Wynne, R.H., 2011. Introduction to Remote Sensing, Fifth Edition. Guilford Press.

Carey, A.B., 2007. AIMing for Healthy Forests: active, intentional management for multiple values. USDA Forest Service, Pacific Northwest Research Station General Technical Report PNW-GTR-721.

Fekety, P.A., Sadak, R.B., Sauder, J.D., Hudak, A.T., Falkowski, M.J., 2019. Predicting forest understory habitat for Canada lynx using LIDAR data. Wildlife Society Bulletin 43, 619–629.

Griffith, B., Youtie, B.A., 1988. Two devices for estimating foliage density and deer hiding cover. Wildlife Society Bulletin (1973-2006) 16, 206–210.

Hoe, M.S., Dunn, C.J., Temesgen, H., 2018. Multitemporal LiDAR improves estimates of fire severity in forested landscapes. International Journal of Wildland Fire 27, 581–594.

Jennings, S.B., Brown, N.D., Sheil, D., 1999. Assessing forest canopies and understorey illumination: canopy closure, canopy cover and other measures. Forestry 72, 59–74.
Junttila, S., Holopainen, M., Vastaranta, M., Lyytikäinen-Saarenmaa, P., Kaartinen, H., Hyyppä, J., Hyyppä, H., 2019. The potential of dual-wavelength terrestrial lidar in early detection of Ips typographus (L.) infestation–Leaf water content as a proxy. Remote Sensing of Environment 231, 111264.
Junttila, S., Hölttä, T., Puttonen, E., Katoh, M., Vastaranta, M., Kaartinen, H., Holopainen, M., Hyyppä, H., 2021. Terrestrial laser scanning intensity captures diurnal variation in leaf water potential. Remote Sensing of Environment 255, 112274.
Kato, A., Moskal, L.M., Batchelor, J.L., Thau, D., Hudak, A.T., 2019. Relationships between Satellite-Based Spectral Burned Ratios and Terrestrial Laser Scanning. Forests 10, 444. https://doi.org/10.3390/f10050444
Lentile*, L.B., Holden*, Z.A., Smith*, A.M.S., Falkowski, M.J., Hudak, A.T., Morgan, P., Lewis, S.A., Gessler, P.E., Benson, N.C., 2006. Remote sensing techniques to assess active fire characteristics and post-fire effects. Int. J. Wildland Fire 15, 319–345. https://doi.org/10.1071/WF05097
Li, D., Wang, M., Jiang, J., 2021. China's high-resolution optical remote sensing satellites and their mapping applications. Geo-spatial Information Science 24, 85–94. https://doi.org/10.1080/10095020.2020.1838957
Lindenmayer, D.B., Franklin, J.F., 2002. Conserving forest biodiversity: a comprehensive multiscaled approach. Island Press.
Loudermilk, E.L., Pokswinski, S., Hawley, C.M., Maxwell, A., Gallagher, M.R., Skowronski, N.S., Hudak, A.T., Hoffman, C., Hiers, J.K., 2023. Terrestrial laser scan metrics predict surface vegetation biomass and consumption in a frequently burned southeastern US ecosystem. Fire 6, 151.
Matthews, S., 2014. Dead fuel moisture research: 1991–2012. International Journal of Wildland Fire 23, 78–92.
Matthews, S., 2006. A process-based model of fine fuel moisture. International Journal of Wildland Fire 15, 155–168.
Morgan, P., Keane, R.E., Dillon, G.K., Jain, T.B., Hudak, A.T., Karau, E.C., Sikkink, P.G., Holden, Z.A., Strand, E.K., 2014. Challenges of assessing fire and burn severity using field measures, remote sensing and modelling. Int. J. Wildland Fire 23, 1045–1060. https://doi.org/10.1071/WF13058
Murray, D.L., Boutin, S., O'Donoghue, M., 1994. Winter habitat selection by lynx and coyotes in relation to snowshoe hare abundance. Canadian Journal of Zoology 72, 1444–1451.
Nudds, T.D., 1977. Quantifying the vegetative structure of wildlife cover. Wildlife Society Bulletin 113–117.
Saberi, S.J., Agne, M.C., Harvey, B.J., 2022. Do you CBI what I see? The relationship between the Composite Burn Index and quantitative field measures of burn severity varies across gradients of forest structure. International journal of wildland fire 31, 112–123.
Schliemann, S.A., Bockheim, J.G., 2011. Methods for studying treefall gaps: a review. Forest ecology and management 261, 1143–1151.
Sharma, R.C., 2022. An Ultra-Resolution Features Extraction Suite for Community-Level Vegetation Differentiation and Mapping at a Sub-Meter Resolution. Remote Sensing 14, 3145.
Shugart, H., Saatchi, S., Hall, F., 2010. Importance of structure and its measurement in quantifying function of forest ecosystems. Journal of Geophysical Research: Biogeosciences 115.
Smith, A.M., Ramsay, P.M., 2018. A comparison of ground-based methods for estimating canopy closure for use in phenology research. Agricultural and Forest Meteorology 252, 18–26.
Vales, D.J., Bunnell, F.L., 1988. Comparison of methods for estimating forest overstory cover. I. Observer effects. Canadian Journal of Forest Research 18, 606–609.
Valverde, T., Silvertown, J., 1997. CANOPY CLOSURE RATE AND FOREST STRUCTURE. Ecology 78, 1555–1562. https://doi.org/10.1890/0012-9658(1997)078[1555:CCRAFS]2.0.CO;2
Vanbianchi, C., Gaines, W.L., Murphy, M.A., Pither, J., Hodges, K.E., 2017. Habitat selection by Canada lynx: making do in heavily fragmented landscapes. Biodivers Conserv 26, 3343–3361. https://doi.org/10.1007/s10531-017-1409-6
Viney, N.R., 1991. A review of fine fuel moisture modelling. International Journal of Wildland Fire 1, 215–234.

Wang, D., Shao, Q., Yue, H., 2019. Surveying wild animals from satellites, manned aircraft and unmanned aerial systems (UASs): A review. Remote Sensing 11, 1308.

Chapter 2. Quantifying Forest Litter Fuel Moisture Content with Terrestrial Laser Scanning

Batchelor, J.L.; Rowell, E.; Prichard, S.; Nemens, D.; Cronan, J.; Kennedy, M.C.; Moskal, L.M. Quantifying Forest Litter Fuel Moisture Content with Terrestrial Laser Scanning. *Remote Sensing* **2023**, *15*, 1482, doi:10.3390/rs15061482.

2.1 Abstract

Electromagnetic radiation at 1550 nm is highly absorbed by water and offers a novel way to collect fuel moisture data, along with 3D structure of wildland fuels/vegetation, using lidar. Two terrestrial laser scanning (TLS) units (FARO s350 [phase shift, PS] & RIEGL vz-2000 [time of flight, TOF]) were assessed in a series of laboratory experiments to determine if lidar can be used to estimate moisture content of dead forest litter. Samples consisted of two control materials where angle and position could be manipulated (pine boards and cheesecloth), and four single-species forest litter types (Douglas-fir needles, ponderosa pine needles, longleaf pine needles, and southern red oak leaves). Sixteen sample trays of each material were soaked overnight, then allowed to air dry with scanning taking place at 1-hr, 2-hr, 4-hr, 8-hr, 12-hr and then in 12-hr increments until samples reached equilibrium moisture content with the ambient relative humidity. Samples were then oven dried for final scanning and weighing. Spectral reflectance values of each material were also recorded over the same drying intervals using a field spectrometer. There was a strong correlation between the intensity and standard deviation of intensity per sample tray and the moisture content of the dead leaf litter. A multiple linear regression model with a break at 100% gravimetric moisture content produced the best model with R2 values as high as 0.97. This strong relationship was observed with both the TOF and PS lidar units. At fuel moisture contents greater than 100% gravimetric water content, the correlation between the pulse intensity values recorded by both scanners and fuel moisture content was strongest. The relationship deteriorated with distance, with the TOF scanner maintaining a stronger relationship at distance than the PS scanner. Our results demonstrate that lidar can be used to detect and quantify fuel moisture across a range of forest litter types. Based on our findings, lidar may be used to quantify fuel moisture levels in near real time and could be used to create spatial maps of wildland fuel moisture content.

2.2 Introduction

Water content within live and dead plant material, termed fuel moisture, is one of the most critical contributors to wildland fire behavior. Moisture content determines the availability and likelihood of wildland fuels to ignite and is a driver for many elements of fire behavior including rate of spread, fireline intensity, and flame length (Rothermel, 1983, 1972). Prior to ignition, moisture must first effectively be boiled off from fuels for fuel temperatures to rise above 200^{o} C and attain heat of ignition for pyrolysis (Countryman, 1974; Jolly, 2007). Live and dead fuel moistures are highly dynamic over space and time and are difficult to measure over diverse fuel types, and at differing spatial and temporal scales. Small changes in solar radiation and weather impact fuel moisture (Matthews, 2014) with fuel moisture levels in fine fuels varying throughout the day depending on time and temperature (Flannigan et al., 2016; Viney, 1991). Live and coarse dead fuels are minimally affected by daily variations. They respond to longer-term, monthly to seasonal fluctuations in weather and climate (Keane and Gray, 2013; Rowell et al., 2022; Yebra et al., 2013). Identifying techniques to increase the speed and spatial resolution of fuel moisture measurements has gained importance because fire behavior models increasingly rely on complex data that include fine scale characterization of the location and moisture content of potential fuels (Pimont et al., 2016). With longer and more severe wildfire seasons associated with climate change, real-time assessments of fuel moisture and when fuels are cured for burning are increasingly needed (Flannigan et al., 2016; Gergel et al., 2017; Ma et al., 2021). Accurate estimates of live and dead fuel moisture are a critical input for fire behavior models, with small variations in fuel moisture levels having a greater effect on model outputs as models become more advanced (Rossa and Fernandes, 2018; Viney, 1991).

Fuel moisture estimates can be made at local scales using field sampling techniques or across landscapes with remote sensing techniques. Direct measurement methods can be labor intensive and time consuming for a robust quantification. Samples must be collected of either live or dead vegetation and placed in a sealed container to avoid fluctuations due to changes in ambient relative humidity. Field-collected samples are then oven dried to ensure that all water is removed from a sample prior to measuring the dry biomass (Pollet and Brown, 2007). To calculate gravimetric fuel moisture, the dry weight of the sample is subtracted from the original weight of the sample, and this value is then divided by the dry weight of the sample, following 24-72 hours

of drying (depending on the size of the fuel element). Due to the need for laboratory processing, such measures of fuel moisture do not produce results until long after the field collection is complete. Another field method used to measure fuel moisture involves the placement of wooden dowels of a known dry weight in the field until the dowels have reached equilibrium with ambient humidity (typically after 12 hours). The dowels can then be weighed on site to determine moisture content (Haines and Frost, 1978). Electronic fuel moisture probes are also often used to collect moisture estimates digitally (Matthews, 2014; Pollet and Brown, 2007). However, both methods are limited to a single point assessment of moisture, and can miss important fuel moisture gradients across space and time. Aggregation of multiple single point moisture measurements is possible to estimate moisture content across an area, but is cumbersome to implement. A better solution is to employ remote sensing techniques, such that large areas can be accurately sampled in a continuous manner.

2.2.1 *Remote Sensing of Moisture*

Remote sensing techniques to quantify fuel moisture generally rely on the reflectance of the vegetation in sections of the electromagnetic spectrum that are more sensitive to changes in moisture content. The near infrared (NIR) wavelength 1450nm and shortwave infrared (SWIR) wavelength 1900nm are highly absorbed by water. Previous studies have demonstrated that, in these wavelengths, the reflectance of an object will increase as moisture content decreases (Ceccato et al., 2002; Datt, 1999; Tian et al., 2001; Tucker, 1980; Wang et al., 2008). As a material dries, the relative increase in reflectance will fluctuate by EM wavelength, but for many plant species the relative change in reflectance is greatest between 1400nm to 1600nm (Figure **2.2** *Using a 1550-nm wavelength scanner, scans were taken of a single section of cut pine board fully saturated with water, approximately 30% moisture content, and oven dried. At fully saturated, the board not only reflects less light, but reflectance also is more heterogenous across the surface.*
2.1). Spectral indices such as the global vegetation moisture index (GVMI) take advantage of this relationship and can be employed using data from numerous remote sensing satellites such as Landsat, MODIS, and Sentinel (Ceccato et al., 2002). Analysis of spectral signatures to quantify fuel moisture content is not limited to landscape-level satellite imagery. Fine-scale spectroscopy has also been used to quantify moisture content in various applications. Examples include determining the influence of moisture content on the combustion and consumption of Douglas-fir

(*Pseudotsuga menziesii*) wood samples (Makowiecki et al., 2020), seasonal variation of moisture content in lodgepole pine (*Pinus contorta*) and big sagebrush (*Artemisia tridentata* Nutt) litter (Qi et al., 2014), and in lumber mills to sort wood products based on dryness (Watanabe et al., 2011). When viewed with an infrared (IR) camera, dead vegetation that is fully saturated with water appears darker and more heterogeneous than dry vegetation that appears lighter and more homogenous (Figure 2.2). Infrared imagery acquired via drone has been shown to have moderate predictive power to characterize fuel moisture gradients as the radiance of ground cover picked up by a passive IR sensor increases as material dries (Barber et al., 2021).

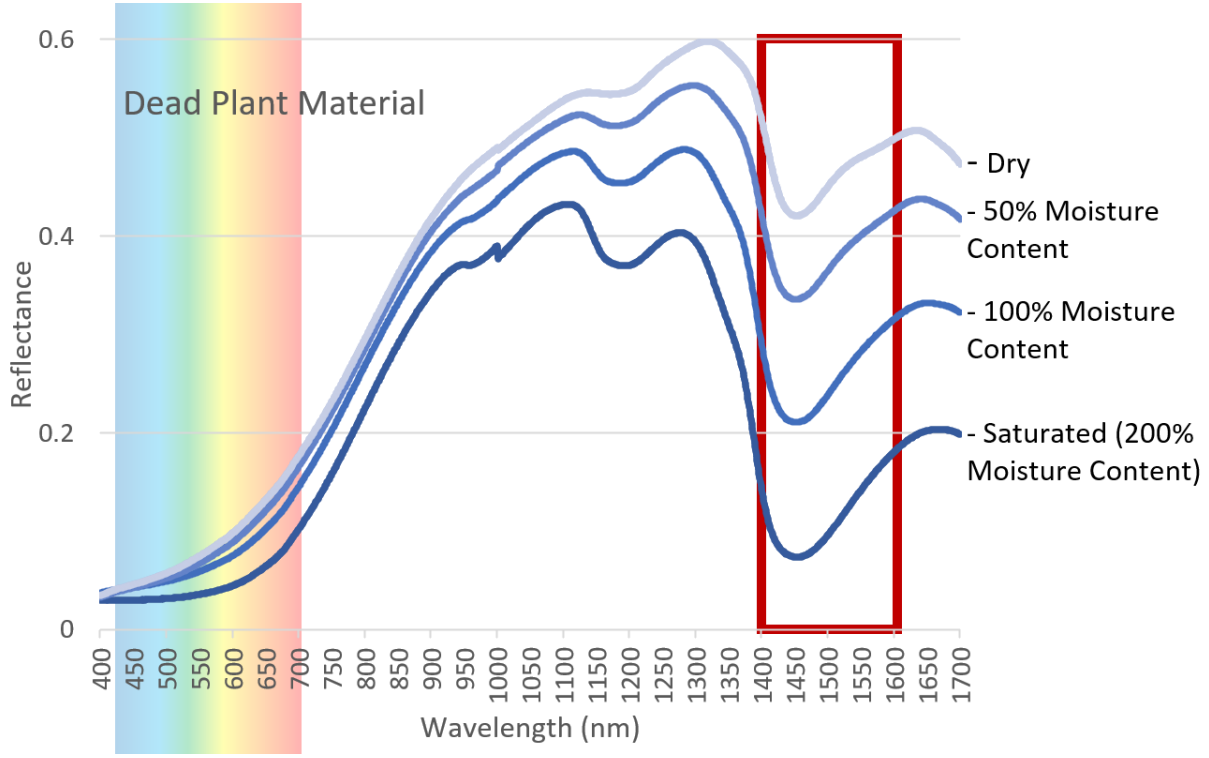

Figure 2.1 *Conceptual diagram of the reflectance of dead vegetation when it is fully saturated with water to when it is dry. The red box is the section of the NIR electromagnetic spectrum that has the greatest change as vegetation dries (1400 – 1600nm).*

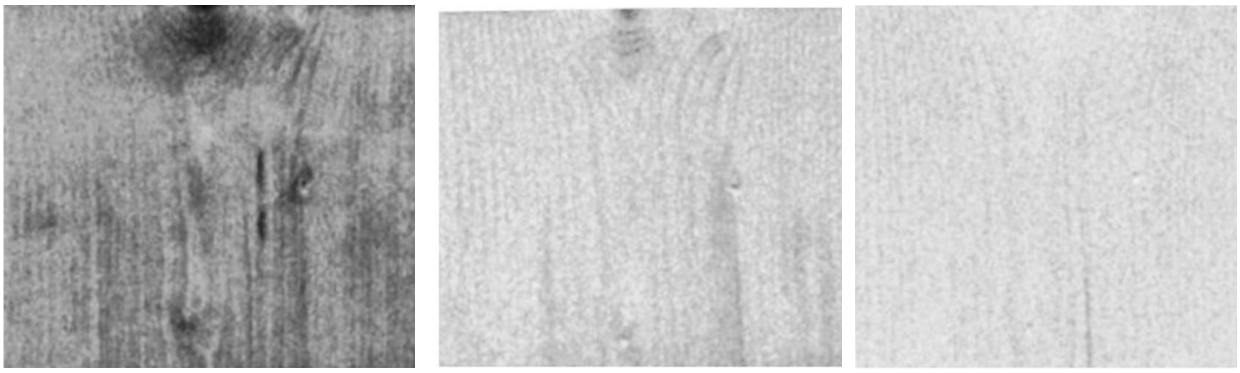

Fully saturated with water ~30% moisture content Oven dried

Figure 2.2 *Using a 1550-nm wavelength scanner, scans were taken of a single section of cut pine board fully saturated with water, approximately 30% moisture content, and oven dried. At fully saturated, the board not only reflects less light, but reflectance also is more heterogenous across the surface.*

2.2.2 *Passive VS Active Sensors*

Passive sensors rely on reflected energy from a controlled external light source or the sun and have been frequently used to quantify moisture content. This includes the use of satellite imagery for surface and soil water detection (Vinnikov et al., 1999; Wang and Qu, 2009), landscape-scale fuel moisture content quantification (Dragozi et al., 2021; Hao and Qu, 2007), and spectroscopy for single sample vegetation moisture content (Gillon et al., 2004; Qi et al., 2014). The capacity for active sensors such as light detection and ranging (lidar) to evaluate moisture content of dead wildland fuels has not been fully evaluated. This evaluation is worthwhile because active sensors offer distinct advantages over passive sensors. Passive sensors are only able to capture the reflectance of the surface of vegetation, while active sensor energy pulses can penetrate through small gaps in the vegetation coverage to sample surfaces that would be occluded to a passive sensor. Further, with active sensors, a three-dimensional (3D) location is also included with each pulse while most applications for passive sensors only supply a two-dimensional location. This allows for a 3D model to be made to quantify vegetation structure, as well as a conditional element (moisture content).

A lidar unit sends out a pulse of energy and calculates the distance traveled by each pulse along with the amount (i.e., intensity) of energy returned. A common wavelength for lidar to use

is 1550 nm, which is within the NIR section that has a relatively large change in reflectance as a material loses moisture (Figure 2.1). A large portion of lidar data is collected from aircraft (i.e., Airborne Laser Scanning (ALS)) and is used to create fine-scale terrain models from the 3D location information from each lidar return. Moisture content estimates across an area have been derived using topographic models derived from lidar (Kemppinen et al., 2018), but lidar applications extend far beyond ground topography. ALS data has been used extensively to model 3D forest structure elements such as tree height, diameter, vertical composition of forest stands, and identification of canopy gaps (Carson et al., 2004; Dubayah and Drake, 2000; Hudak et al., 2009; Wulder et al., 2012). Vertical point distributions of lidar returns have also been used to model fuel connectively to characterize fire behavior (Stavros et al., 2018).

The three dimensional point clouds of ALS returns have been used successfully to quantify a multitude of forest structural parameters, and the recorded intensity values have also been used to detect inundated areas (i.e., wetlands), identify tree species from crown architecture, and detect snags (Bright et al., 2013; Korpela et al., 2010; Lang et al., 2020). ALS has been looked at for its potential for quantifying surface moisture, but variations in the vegetation cover have contributed more to changes in intensity than the presence of water (Garroway et al., 2011). There are inherent issues with using lidar intensity values to quantify ground cover conditions. The amount of energy returned to a scanner depends on the distance traveled, the angle of incidence when contacting a surface, the material of the surface, and the texture of the surface (Krooks et al., 2013). There is an important distinction between intensity and reflectance. Intensity is the amount of energy returned to the scanner, while reflectance is an objective measurement of what proportion of incoming energy is being reflected from a surface. Reflectance can be modeled from intensity if adjustments are made for distance traveled, angle of incidence, and surface characteristics. However, calibrating intensity values to derive reflectance is often done by simply adjusting for distance traveled but not accounting for angle of incidence or surface texture (Hasegawa, 2006; Kashani et al., 2015). Further, intensity values are difficult to normalize across the full extent of an acquisition and are typically not calibrated between acquisitions. Intensity maximum thresholds are variable to preclude signal saturation by using automatic gain control. However, if lidar intensity values are normalized, and either a single scanner is used or values are calibrated between scanners, useful spectral information can be derived from intensity values. This would allow for the benefits of active sensors to be combined with spectral reflectance indices to quantify condition

information about the vegetation being sampled (i.e., to determine moisture content). Landscape-level ALS is invaluable for forest applications, but are not useful for fuel moisture mapping because ALS flights are costly and generally occur every 1-5 years whereas fuel moisture can meaningfully change on an hourly to monthly basis depending on the fuel category. Terrestrial laser scanning (TLS) offers an option where fine scale models of fuel moisture can be produced on demand.

2.2.3 *Terrestrial Laser Scanning (TLS)*

TLS has been used extensively for fine-scale modeling of forest structural elements. Using TLS to quantify the location and amount of potential wildfire fuels is a topic that has seen extensive research (Loudermilk et al., 2009; Rowell and Seielstad, 2012; Rowell et al., 2015). However, using TLS intensity returns for characterizing the condition of wildland fuels has not been fully explored. For a TLS unit using 1550 nm laser light, the amount of energy from a TLS pulse that is reflected off a surface should decrease by absorption of energy as surface moisture increases. Just as IR radiation at 1550 nm from the sun is absorbed, and not reflected, by water vapor and thin layers of water, the same principle holds true for IR radiation generated from a laser (Plyler and Sleator, 1931; Ponomarev et al., 2001). For example, TLS has been used to detect moisture in building materials and mapping moisture movement in buildings by comparing relative changes in intensity values of returns (Suchocki et al., 2018; Suchocki and Katzer, 2018). Similarly, phase-based TLS units have been successfully used to quantify surface moisture levels on a sandy beach (Jin et al., 2020).

Intensity values of TLS sensors have been used to quantify many different variables of interest in live vegetation. Much the same as how vegetation spectral indices from images (such as NDVI) can be used to quantify vegetation health, leveraging relationships between different laser wavelengths of TLS units can also provide information on live leaf health and location. Lidar sensors of differing laser wavelengths can be used in conjunction with each other to provide an index based on intensity values to more easily separate out leaves from stems (Danson et al., 2014; Gaulton et al., 2010; Hancock et al., 2017). TLS intensity values have also been used to quantify the moisture content of live leaves, using a dual wavelength approach to provide an index value (Elsherif et al., 2018; Gaulton et al., 2013; Junttila et al., 2018, 2017). Such an approach has been effective at providing a robust measurement of leaf water content and has been related to overall

plant health. Such an approach has also been used to measure fluctuation in leaf water potential on an hourly basis (Junttila et al., 2021), and to model whole tree fuel moisture content and equivalent water thickness in a three dimensional manner (Elsherif et al., 2019b, 2019a). TLS intensity values and specifically TLS intensity values of two differing wavelengths are proven tools to quantify moisture content within live vegetation. Many of the studies that use TLS intensity to quantify moisture content provide a calibrated intensity value that accounts for distance traveled by the laser pulse to attempt to report reflectance of the surface and not just the amount of energy returned to the scanner (i.e., intensity). TLS intensity value degradation with distance often does not follow a simple linear relationship and some scanners may apply a dampening effect to close returns to avoid signal saturation (Calders et al., 2017; Tan et al., 2019). While TLS intensity values have been shown to be related to moisture content on many different levels, leveraging this relationship to quantify moisture gradients in dead forest litter from a single vantage point has yet to be fully explored.

There are a wide range of lidar units that are commonly used for terrain and vegetation mapping. Two significant differences among TLS units are the wavelength used and how distances are calculated. For this study, we used 1550 nm wavelength terrestrial lidar scanners because of the sensitivity of that wavelength to moisture, and we also evaluated two types of TLS units: a time of flight (TOF) and phase-shift (PS). A TOF lidar unit sends out a discrete pulse of energy and records the time it takes for the pulse to be reflected off a surface. Using the known speed of light, the object distance is calculated (Raj et al., 2020). The advantage of TOF units is that multiple returns can be recorded for each pulse sent as a partial reflection of the energy is still recorded. Disadvantages are that surfaces at proximity are often distorted and that each pulse must be returned before the next can be sent out. A PS lidar unit emits a continuous laser, and distance is calculated by using the phase shift of the incoming reflected energy relative to phase of the outgoing energy. There are not discrete pulses of energy that are able to record multiple returns. PS tends to be faster with less distortion at close distances (Suchocki, 2020). However, PS scanners tend to have a more limited range, mainly due to energy requirements. The different technologies produce slight differences in how intensity values are calculated (Calders et al., 2020; San José Alonso et al., 2011; Suchocki, 2020).

2.2.4 *Study Objectives*

Lidar is becoming increasingly common with rapid advancements in field applications. In this study we explored the ability of TLS to quantify fuel moisture in a controlled laboratory environment. The main objective was to demonstrate that a single TLS unit can provide a reliable measurement of fuel moisture in fuel beds comprised of senesced leaf material, and to test if TOF or PS lidar technology performed better. Intermediary objectives were to measure the relative change in fuel bed reflectance in relation to water content with a passive sensor spectrometer to validate that the change in TLS intensity values correlated with a change in reflectance measured by the spectrometer. To then derive a host of potential metrics from the multiple intensity returns across a sample to determine which metric (or combination of metrics) had the strongest relationship to fuel moisture. Finally, to determine if changing the angle of the fuel bed relative to the ground affected the relationship between intensity metrics and fuel moisture content of the samples. Additionally, a table of coefficients was developed for the relationships between intensity metrics and moisture content for the different sample types and distances. A workflow diagram is presented in Figure 2.3 that outlines the study objectives and illustrates the structure of the study. If TLS scanning becomes an operational method to rapidly quantify fuel moisture in potential fire fuels, it will be a valuable tool to aid in prescribed burning and fire behavior prediction. Intensity values were not calibrated for distance in this study to allow for a more direct comparison between the two scanners at set distances.

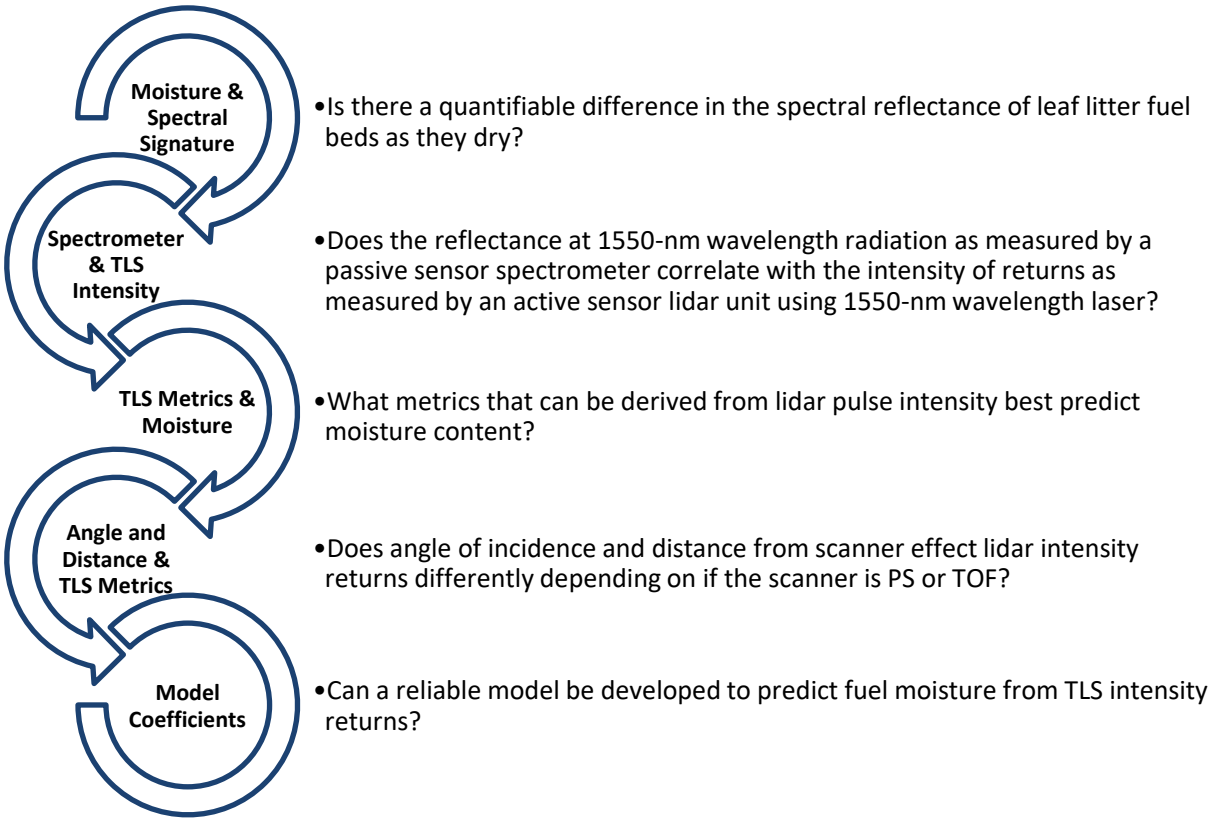

Figure 2.3 *Workflow diagram of the research questions for this study and how they build upon each other to address the final goal of model development.*

2.3 Materials and Methods

2.3.1 *Materials*

Six unique materials were used to evaluate the relationship between lidar reflectance and fuel moisture, including four common forest litter types and two controls (Table 2.1). Litter beds were constructed from senesced needle and broad leaf material collected from forest locations in Washington and northern Florida. Litter types included Douglas-fir (*Pseudotsuga menziesii*) needles, longleaf pine (*Pinus palustris*) needles, southern red oak (*Quercus falcata*) leaves, and ponderosa pine (*Pinus ponderosa*) needles. Litter samples were air dried and sorted to remove any foreign particles. When assembling leaf litter trays, care was taken to ensure that the litter completely occluded the tray to ensure all point returns were plant material and not the underlying tray. Sample trays were constructed of a non-porous white plastic material measuring 30cm x 30cm

x 5cm with a fine mesh screen as the base to allow for draining of water. Sixteen samples (trays) of each litter type and control material were assembled.

The two controls, milled pine wood and fabric mesh, were used to assess the influence of scan angle on intensity of returns. The fabric mesh consisted of uniform layers of cotton cheese cloth (a gauze-like material) to mimic the porosity of forest litter. The other control material was milled, untreated pine board approximately 30 cm x 30 cm x 1.5 cm in size. Three of the sixteen Douglas-fir samples were removed from the analysis due to fine soil contamination that impacted reflectance values.

Table 2.1 *Sample types and weights used in this study. Uncompacted indicates the samples that naturally had a lot of open area with no readily defined depth. Litter fuels were allowed to extend up out of the sample trays to mimic natural conditions.*

Sample type	Weight range (grams)	Weight mean (grams)	Depth of Sample
Douglas-fir (DF)	119 – 156	135	~3cm
Ponderosa pine (PP)	104 – 158	129	Uncompacted
Longleaf pine (LLP)	70 – 123	101	Uncompacted
Southern red oak (SRO)	27 – 35	31	Uncompacted
Fabric mesh (FM)	66 – 74	67	~0.5cm
Pine board (PB)	514 – 596	569	~1.5cm

2.3.2 *Experimental Design*

2.3.2.1 TLS Data Collection

The fuel moisture experiment was conducted at the Pacific Wildland Fire Sciences Laboratory in Seattle, WA. All samples were fully saturated by soaking them in water for a minimum of 24 hours in polyethylene bags. For scanning, samples were arranged in sets of four and placed at 3m, 6m, 9m, & 12m distance from the scanners (Figure 2.4). Samples were scanned simultaneously with PS and TOS units at 0 degrees (parallel to the ground) at each distance. Control surfaces were additionally scanned at 45 degrees and 90 degrees (perpendicular to the ground) (Table 2.2). The weight of each sample was recorded, then samples were rotated to the

next defined distance and the process was repeated three times, such that each sample was scanned at all four scan locations.

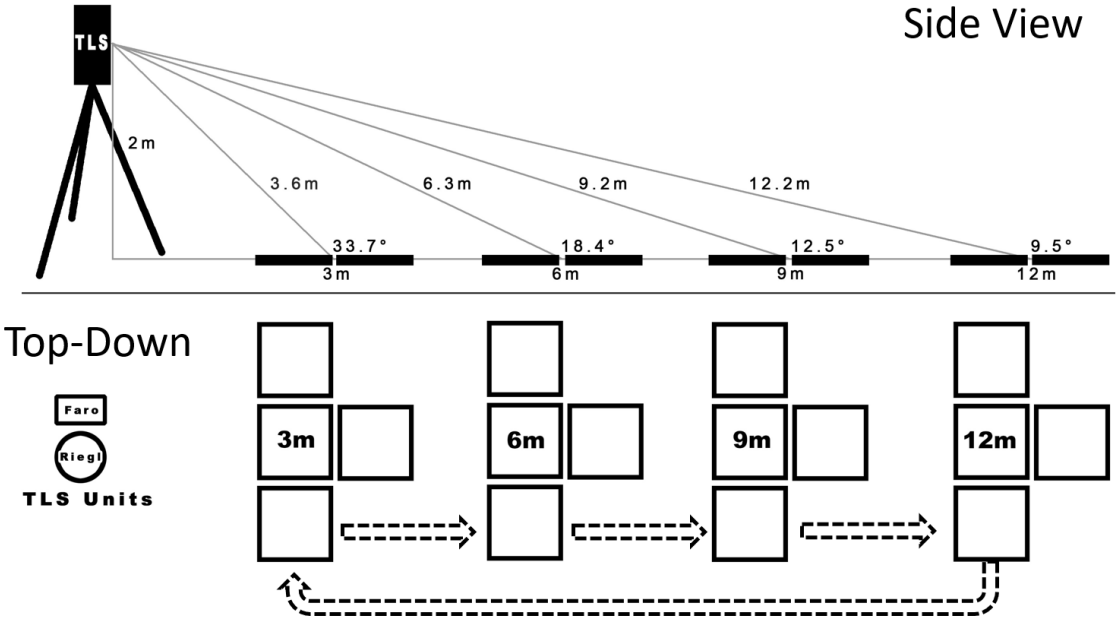

Figure 2.4 *Layout of samples during scanning. Samples were moved in groups of 4. The arrow indicates the rotation direction used to scan every sample, at every location, at every time period. Sample orientation is referred to as 0 degrees which is perpendicular to the ground, but the angle to the scanner decreases as distance from scanner increases.*

After the initial scan (hr 0), the process was repeated at the hourly time intervals of 1, 2, 4, 8, and 12 hr since removal from the water bath, and then repeated every 12 hours until samples reached equilibrium moisture content with the ambient relative humidity (i.e., their weight stabilized and was no longer decreasing due to water evaporation). Scanning at four locations, weighing the samples, and rotating samples took approximately 50 minutes to one hour. Between scan times, samples were placed in a climate-controlled room with ~25% relative humidity to allow for gradual drying. Drying times varied by material type (Table 2.2). Once samples reached a stable weight, they were placed in a drying oven set at 70˚C until samples achieved a constant weight (48 hr). A final set of scans was conducted immediately following the removal of samples from the oven, and then oven dry weights were collected. Sample gravimetric moisture content

was calculated by subtracting final dry weight of the sample from the weight recorded during the drying process, then dividing by the final oven dried weight.

Table 2.2 *Scanning intervals, starting with the time samples were removed from water bath (0). OD refers to oven dry. N is the total number of sample trays clipped from all lidar point clouds and the number of weights recorded. Only the controls were scanned at angles different than 0.*

Sample type	Scan intervals (hours from first scan)	Angle	N*
Pine board (PB)	0, 2, 4, 8, 12, 24, 48, 72, 120, OD	0, 45, 90	3840 – lidar 1280 – weight
Fabric mesh (FM)	0, 2, 4, 8, 12, 24, 36, 48, OD	0, 45, 90	3456 – lidar 1152 – weight
Douglas-fir (DF)	0, 1, 2, 4, 8, 12, 24, 36, 48, OD	0	*1280*
Ponderosa pine (PP)	0, 1, 2, 4, 8, 12, 24, 36, 48,120, OD	0	*1408*
Longleaf pine (LLP)	0, 1, 2, 4, 8, 12, 24, 36, 48, OD	0	*1280*
Southern red oak (SRO)	0, 1, 2, 4, 8, 12, 24, 36, OD	0	*1152*

*Number of samples = Number of scans (4 distances) * number of trays (16) * scan intervals * 2 scanners (FARO & RIEGL) * 3 angles (PB & FM only)

2.3.2.2 Spectrometer Data Collection

An ASD FieldSpec 4 Wide-Res Field Spectroradiometer (ASD, 2017) with a spectral resolution of 30 nm at 1400 to 2100 nm was used to collect spectral information for each sample to compare with lidar-based reflectance values. The spectrometer lens was placed 33 cm above the tray at a perpendicular angle and an 8-degree lens was used to sample the approximate central 9 cm of each tray. The spectrometer was used when the samples were rotated through the 6 m distance location. Sample trays were individually taken into a dark room dedicated for the spectrometer using a tungsten blub as a light source (approximate wavelength range of 320 nm to 2400 nm). A spectralon disk was used to calibrate the spectrometer before every measurement. Samples were checked to ensure that there were no gaps exposing the tray bottom. The white material of the tray sides likely reflected non-sample light back into the spectrometer sensor; this reflective phenomenon was same for all trays, thus constant. Moreover, for this study we were

only interested in the relative change in each sample as it dries, and not gaining a true and precise measurement of the spectral signature for each sample material nor equating an exact reflectance value as measured by the spectrometer to an exact intensity value from the TLS. In maintaining a consistent sampling environment and procedure, relative change in spectral reflectance between samples was measured.

2.3.3 *Terrestrial Laser Scanners*

Two 1550-nm wavelength TLS scanners including a time-of-flight RIEGL vz-2000 unit and phase-shift FARO s350 unit were used. A summary of the properties of each scanner is presented in Table 2.3. The scanning resolution settings of the FARO and RIEGL were chosen to provide a scanning time of approximately 3.5 min. The FARO scanned at a lower resolution than the RIEGL. A short scan time was prioritized over matching scanning resolution to minimize the evaporation of water from the samples as they were rotated through the 4 scanning locations of each time interval. The number of points per sample decreased as distance from the scanner increased in relation to the scan angle increment of each scanner (Table 2.3). The minimum number of points per sample tray was sampled at 12 m from the FARO unit (~900 points) and the maximum number of points per sample tray was sampled at 3 m from the RIEGL scanner (~103,000 points). Total area effectively sampled with each laser pulse also increased with distance as the laser footprint increased due to both the distance from the scanner as well as the angle of incidence. TLS units were placed as close as possible to each other (~20 cm) and were run simultaneously when scanning. This design was developed to balance the need to gather data rapidly (as the samples were actively losing moisture while TLS scanning was taking place) with the need to have suficient replicants for statistical inferance.

Table 2.3 *Summaries of the two TLS units used for this study. Scan time was ~3.5 min with both scanners running simultaneously using 1550 nm wavelength laser light for each unit. Laser pulses were intercepting the samples at differing angles for each distance. The footprint ellipsoid was significantly elongated at the further distances.*

	Unit Specs		*Approximate number of pulses per sample*			
TLS	Min Range	Max Range	Scan angle Increment	3m	6m	9m
FARO	0.6m	~350m	0.018°	~34,000	~6,000	~2,000
RIEGL	2.5m	~2000m	0.010°	~103,000	~18,500	~6,000
Footprint Size						
TLS	Beam Divergence	Diameter at exit	Ellipsoid at 3m (mm)	Ellipsoid at 6m (mm)	Ellipsoid at 9m (mm)	Ellipsoid at 12m (mm)
FARO	0.3mrad *	2.2mm	3.3 x 5.9	4.1 x 13	5 x 23.1	5.9 x 35.7
RIEGL	0.3mrad	18mm	19.1 x 34.4	19.9 x 63	20.8 x 96.1	21.7 x 131.5

* 0.3mrad corresponds to an increase of 30mm of beam diameter per 100m of range

2.3.4 *Data Processing*

The FARO software "Scene" (FARO, n.d.) and RIEGL software "Riscan Pro" (Riegl, 2021) were used for the intial processing and conversion of the propriatary file formats into a .las format. To ensure that all valid returns from the sample trays were preserved, point cloud filtering was not conducted. This inclusive processing method included some amount of noise from edge effects and errant reflected laser light. However, it was deemed better to use all point returns to ensure all valid returns were included rather than try to filter out noise and subsequently remove valid point returns.

RIEGL intensity values for points ranged from 0 to 50 and FARO intensity values ranged from 0 to 32,767 (scaled to a 15 bit radiometric resolution). After initial processing, the program "CloudCompare" ("CloudCompare [Computer Software]; Version 2.11; 2019. Available online:

http://www.cloudcompare.org (accessed on 1 March 2021).," 2019) was used to manually crop out all points that were returns inside each sample tray. Care was taken to ensure that no points that were returns from the sample trays or tray bottoms were included in the clip based upon the intensity values of the points and proximity to the edge or bottom. The RIEGL scanner has the ability to register multiple returns from each pulse emitted but across all samples, only first returns were within our clipping boundaries. Using only first returns was not intentional, but rather coincidental to how the data was processed. Intensity values were normalized between the FARO scans and the RIEGL by dividing each intensity value by the maxiumum value present in each scan. The normalization process scaled the intensity values between 0 to 1 for easier comparison between the two scanners. The intensity metrics derived per sample were: mean, median, 95th percentile, standard deviation (SD), variance, and skew. Due to the confounding factors of angle of incidence and surface texture, normalized intensity values w ere used in place of intensity values calibrated to represent suface reflectance.

2.3.5 *Analysis*

2.3.5.1 Spectrometer

An averaged spectral signature from the spectrometer sampling was created for each sample type at each sampling interval (e.g., the average value of each wavelength for all 16 ponderosa pine needle litter samples at the 2-hr scan time interval). The reflectance values for each sample at 1550 nm was determined and compared with the moisture content recorded for all samples at the 6-m distance. Simple ordinary least-squares (OLS) regression analysis was performed to determine if reflectance measured by the spectrometer (response) had a significant relationship with moisture content (predictor). Reflectance values recorded by the spectrometer were also compared with the TLS intensity metrics recorded for all samples at the 6-m distance. Simple regression analysis was performed to determine if there was a significant relationship between the spectrometer reflectance values and recorded mean TLS intensity.

2.3.5.2 TLS Intensity

Regression models compared the intensity mean, median, 95^{th} percentile, SD, variance, and skew of all points within each sample. Three regression forms were evaluated including a linear model, a first order polynomial transformation, and a linear broken stick model to determine what

combination of the derived lidar intensity metrics performed best as predictor variables for the measured fuel moisture. Log and squared transformations were evaluated on the predictor variables, and a reduction in AIC (Akaike information criterion) values were used for final selection of predictor variables. AIC values were only calculated for model selection between TLS variables and moisture content. There was a change in slope for metrics at 100% moisture (exception being pine board where change in slope occurred at 40%) therefore a broken stick regression approach was used. Consider a breakpoint at $X=x_b$, and define:

$$I = \begin{cases} 0 & X < x_b \\ 1 & X \geq x_b \end{cases}$$

Then, the broken stick regression model can be written as:

$$Y = \beta_0 + \beta_1 X + \beta_2 I + \beta_3 X * I,$$

where β_0 and β_1 are the intercept and slope for $X < x_b$, and β_2 and β_3 are the change in intercept and slope moving from $X < x_b$ to $X \geq x_b$. Here we set $x_b = 100$.

Finally, an analysis of covariance test was performed to determine if scan angle on the control samples significantly changed the coefficients between lidar intensity and moisture content, treating the scan angle as a simple factor.

2.4 Results

2.4.1 *Moisture & Spectral Signature*

Sample moisture content ranged from 0% (oven dried weight) to 300% (fully saturated). Red oak leaves and the fabric mesh had the highest saturated moisture content and weighed 3 times the dried sample weight. Maximum moisture content for conifer needle litter ranged between 160% to 200%. Fully saturated pine boards reached approximately 65% moisture content.

Sample reflectance values at 1550 nm ranged from 0.1 when fully saturated to 0.6 when oven dried (Figure 2.5). The highest variance between sample moisture content was generally observed at ~1450 nm but a large spread of moisture values was also observed around 1550 nm. Regression analysis showed that sample reflectance at 1550 nm had a significant negative relationship ($p < 0.05$ for all sample materials) with measured fuel moisture. Rate of the decrease, variance of the points, and shape of the relationship changed depending on the sample material. The coefficients

of determination for the sample materials in regard to reflectance measured at 1550 nm and fuel moisture was: Douglas-fir 0.93, ponderosa pine 0.9, longleaf pine 0.84, southern red oak 0.8, fabric mesh 0.77, and pine board 0.84.

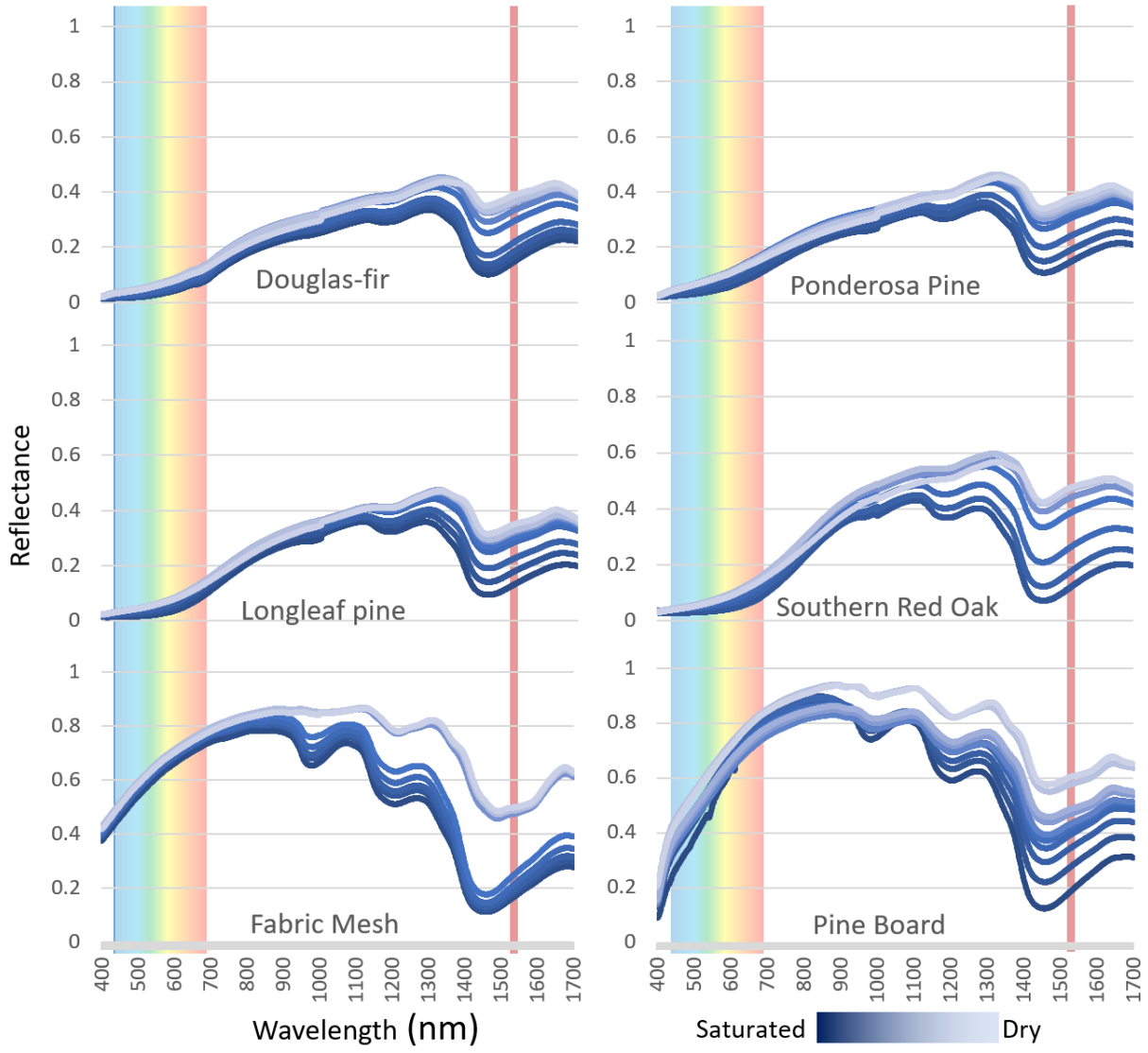

Figure 2.5 *Average reflectance values by sample material and saturation level. The dark blue line represents samples at full saturation, with the color lightening to light blue for the final oven dried reflectance values. The red line at 1550 nm represents the wavelength of the TLS units used for this experiment.*

2.4.2 *Spectrometer & TLS Intensity*

Spectral reflectance at 1550 nm measured by the ASD spectrometer had a significant positive relationship ($p<0.05$) with the normalized mean intensity values from the TLS units (Figure 2.6).

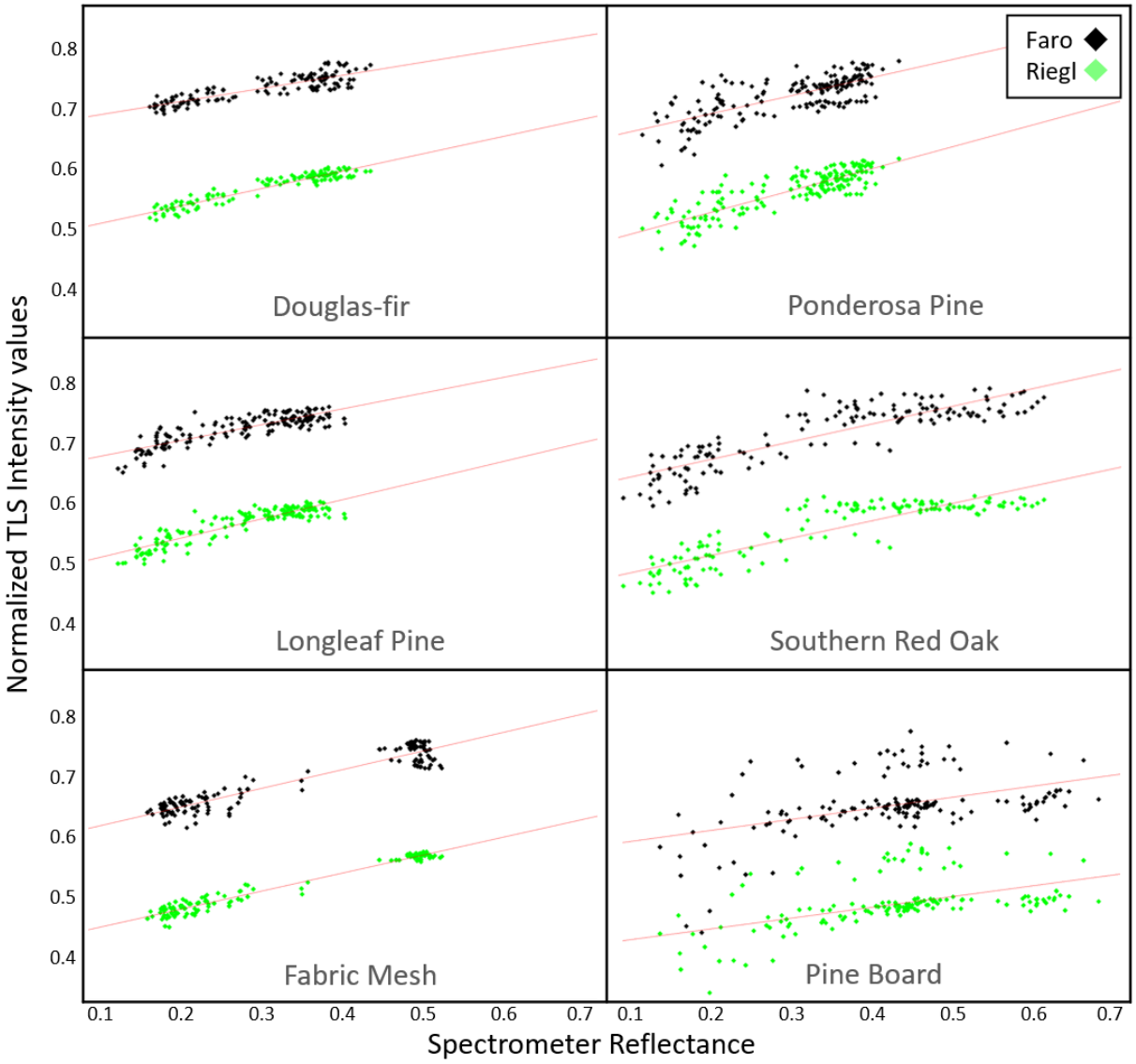

Figure 2.6 *Linear relationship between reflectance values as measured by the spectrometer at 1550 nm and the mean intensity values of all lidar points from a sample. Intensity values were normalized on a scale between 0 and 1 for a direct comparison between the FARO and RIEGL. The lower intensity values from the RIEGL are a product of this normalization and don't indicate that overall less energy was returned by each RIEGL pulse.*

2.4.3 *TLS Metrics & Moisture*

Of the 6 lidar metrics (mean, median, 95th percentile, standard deviation (SD), variance, and skew); mean, median, and 95th percentile were correlated (> 0.8 R^2, $p < 0.05$). Standard deviation and variance were also correlated (> 0.8 R^2, $p < 0.05$). However, there was no meaningful correlation between the mean and the standard deviation (< 0.25 R^2, $p < 0.05$). The best performing models with the highest coefficient of determination and lowest AIC were the linear broken stick models using the mean intensity values with the break at 100% moisture content for all sample materials except the pine board. The pine board moisture content percentage never increased above 100% but the distinct change in slope occurred at 40% moisture content. The locations of the breaks were determined by where the slope of the linear relationship visually changed with the exact subjective value of 100% being chosen as it was a value with an easily understood meaning (weight of the sample was equal parts water and vegetation) and was uniformly a location across all material types (except the pine boards) where the slope of the relationship changed. The mean of lidar intensity values had the strongest correlation with fuel moisture for the RIEGL data and performed well for the FARO data (Figure 2.7 and supplemental Figure 6.S2.1 located in the appendices). However, standard deviation of intensity returns was also strongly correlated with fuel moisture and was a better predictor for some FARO samples than mean intensity (Figure 2.8). Images were produced using the point clouds from the FARO scanner to illustrate the change in the reflectance of the samples at 1550 nm (supplemental Figure 6.S2.2).

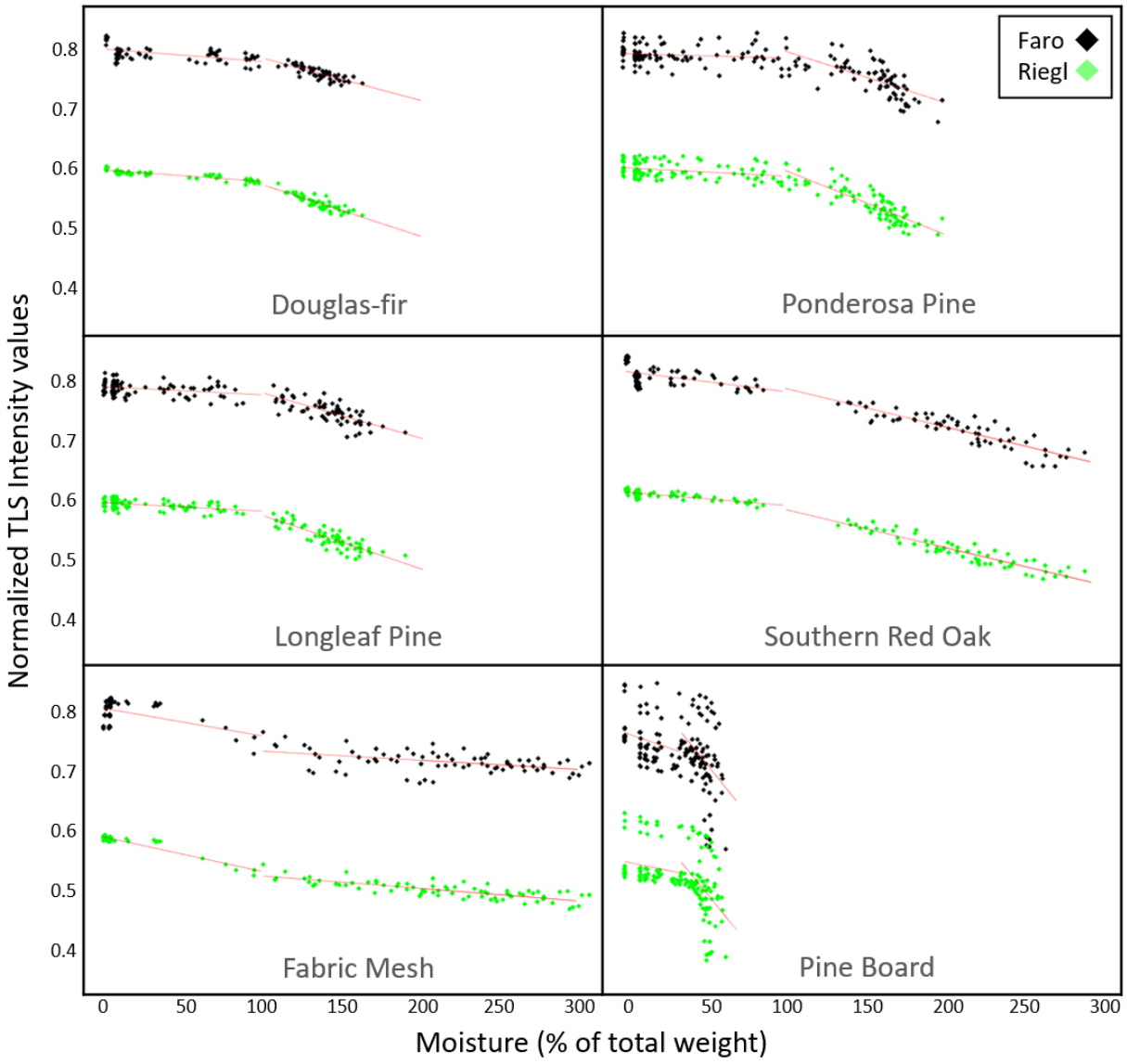

Figure 2.7 *Mean normalized intensity values of the samples placed at 3 m from FARO and RIEGL scanners. Regression lines from a broken stick linear regression model are added. The selected break location was 100% for all sample materials except pine board where the break was located at 40%.*

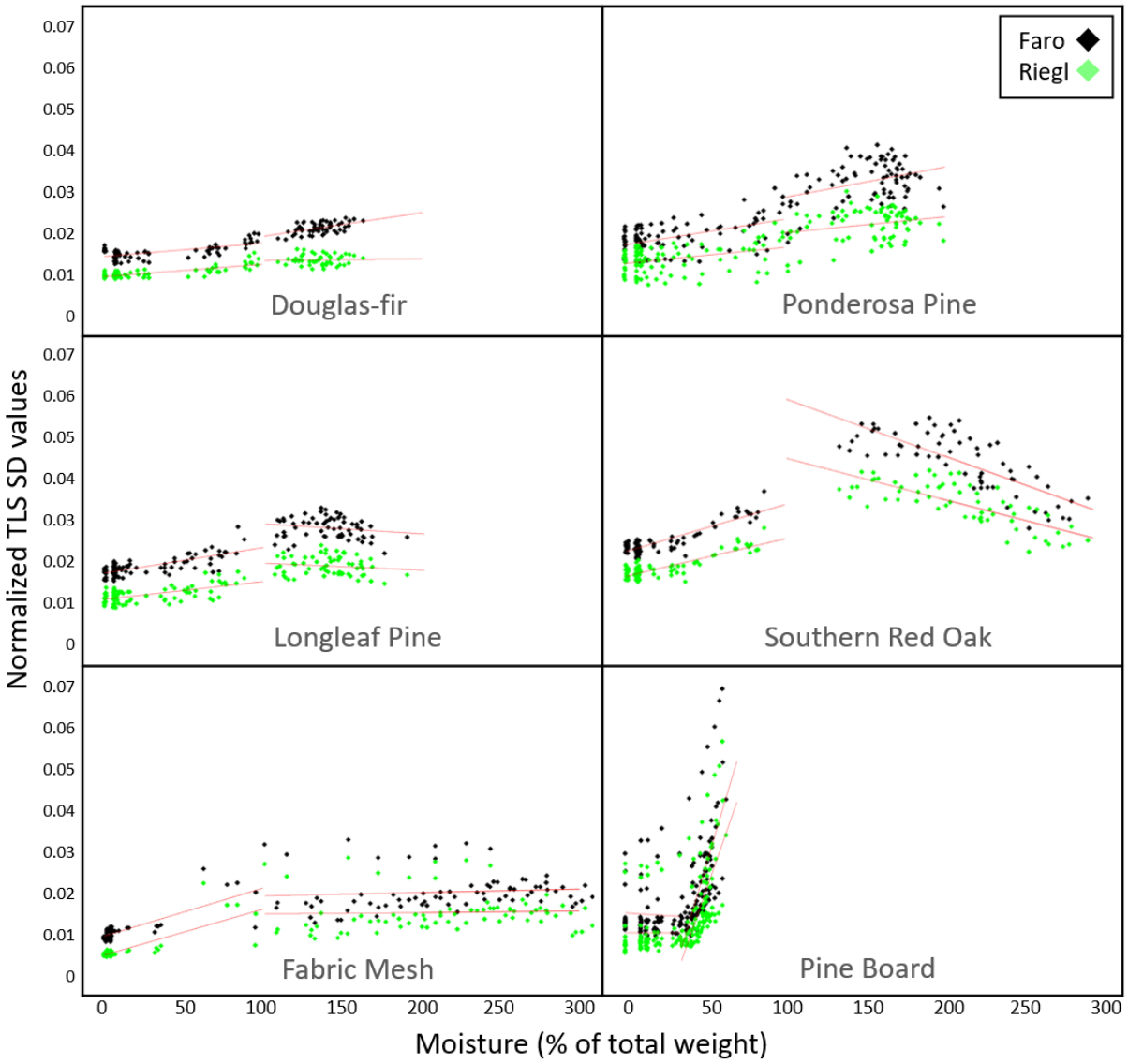

Figure 2.8 *Standard deviation of normalized intensity values of the samples placed at 3m from the FARO and RIEGL scanners. Regression lines from a broken stick linear regression model are added. The break location was 100% for all sample materials except pine board where the break was located at 40%.*

2.4.4 *Angle and Distance & TLS Metrics*

Correlations between reflectance and fuel moisture were comparable between the FARO and RIEGL units. However, beyond a distance of 3 m, the time-of-flight RIEGL unit performed much better than the FARO at modeling fuel moisture. While the relationship deteriorated with distance for the RIEGL, the rate of deterioration was much less than that of the FARO.

Deterioration was related to the distance, the angle of incidence (Figure 2.4), and the footprint size (Table 2.2).

An ANCOVA test was performed to determine if the coefficients for mean intensity values vs moisture content of the 45^o and 90^o control samples differed significantly from the 0^o control samples. The normalized linear broken stick model coefficients are presented in the supplemental table 6.S2.1 in the appendices, noting coefficient values that were significantly different than the coefficient values of 0^o samples. With the notable exception of the FARO data at 3 m, there was no significant difference between the coefficients for the 0^o and 45^o intensity values. In general, the coefficients did not significantly change until the samples were at an angle greater than 45^o.

2.4.5 *Model Coefficients*

The coefficient of determination for final broken stick models ranged from 0.98 for the southern red oak and fabric mesh samples at 3m distance to 0.07 for long leaf pine at 12 m. With few exceptions, regression models of reflectance values from the TOF RIEGL had stronger model fits than that of the PS FARO, especially at the further distances (Table 2.4). A comprehensive table of the coefficients and R^2 values for the non-normalized data in included in supplementary Table 6.S2.2. Each sample type at each distance with moisture levels before and after the break in the regression line, using a multiple linear regression model of mean and SD reflectance.

Table 2.4 *Coefficient of determination values for multiple linear regression models across sample types. Mean intensity values of each sample and the standard deviation of each sample produced the best fitting model. The 0, 45, & 90 indicate the sample angle relative to the ground. A more comprehensive table is presented in supplementary* Table 6.S2.2.

Mean & SD		DF R^2	PP R^2	LLP R^2	SRO R^2	FM 0 R^2	FM 45 R^2	FM 90 R^2	PB 0 R^2	PB 45 R^2	PB 90 R^2
FARO	ALL	0.65	0.40	0.28	0.83	0.66	0.84	0.88	0.25	0.44	0.49
RIEGL	ALL	0.86	0.56	0.69	0.95	0.92	0.94	0.92	0.32	0.54	0.50
FARO	3M	0.94	0.78	0.86	0.95	0.91	0.96	0.96	0.43	0.59	0.52
RIEGL	3M	0.95	0.76	0.90	0.98	0.96	0.98	0.98	0.46	0.65	0.61
FARO	6M	0.81	0.55	0.68	0.94	0.87	0.94	0.95	0.34	0.58	0.60
RIEGL	6M	0.92	0.60	0.79	0.97	0.94	0.97	0.98	0.38	0.58	0.63
FARO	9M	0.62	0.45	0.19	0.91	0.66	0.86	0.84	0.25	0.47	0.45
RIEGL	9M	0.83	0.51	0.72	0.96	0.93	0.97	0.97	0.30	0.55	0.67

FARO	12M	0.54	0.37	0.07	0.85	0.66	0.89	0.86	0.17	0.44	0.44
RIEGL	12M	0.88	0.49	0.68	0.93	0.92	0.97	0.97	0.26	0.50	0.67

2.5 Discussion

In this laboratory based study, we quantified changes in fuel moisture using active sensor laser pulses at set distances from two 1550 nm lidar units. Beyond the determination that lidar intensity returns can be used to estimate fuel moisture levels, we also determined that time-of-flight and a phase shift lidar units can both effectively measure changes in moisture in litter fuel beds. These findings corroborate studies that have used lidar to determine material characteristics using the intensity of the return values (Di Biase et al., 2021; Zahiri et al., 2021). They are also in line with the numerous studies that utilized dual band TLS point clouds to determine live leaf moisture content (Elsherif et al., 2018; Gaulton et al., 2013; Junttila et al., 2016). However, this study provides an important new perspective on using a single wavelength TLS unit to determine moisture content of wildland fuels. While we limited our study to common forest litter types, this is an important step in utilizing an active sensor to relate spectral qualities of wildland fuels with fuel moisture while also capturing three-dimensional positional information.

2.5.1 *Moisture & Spectral Signature*

For this study, we first used standard spectrometry to confirm that there was a quantifiable difference in the spectral reflectance of leaf litter fuel beds as they air dry. All samples increased in reflectance as they dried. Increased reflectance with decreasing moisture content is well established (Bowyer and Danson, 2004; Paltridge and Mitchell, 1990; Qi et al., 2014), but quantifying the change in reflectance with a precise spectroradiometer allowed us to employ an established method to measure spectral reflectance changes instead of fully relying on a novel use of TLS to gauge change. We used a simple sampling technique of a singular nadir view to measure the reflectance of the materials as they dried. Sampling angle, spectrometer footprint size, tray materials, light source would all affect the values recorded by the spectrometer. The fact that reflectance changes as materials dry is well established. An exhaustive analysis of how spectrometer setup affected reflectance values recorded was not the purpose of this study. The use of the spectrometer was only to establish if changes in moisture content from a well-established

methodology using a spectrometer correlated with the changes in intensity recorded by a TLS unit.

2.5.2 *Spectrometer & TLS Intensity*

Reflectance at 1550 nm as recorded by the spectrometer was strongly correlated with the intensity values from the TLS units. Model fit differed among sample types, with the lowest coefficient of determination for pine boards. This was likely due to the heterogenous reflectance, an artifact of the wood grain and knots. Aside from the pine boards, there was also a clear tendency for the more compact samples to have a higher coefficient of determination (e.g., Douglas-fir needles and the fabric mesh; Figure 2.6). Ponderosa pine, longleaf pine, and southern red oak were relatively uncompacted, with large amounts of air space within the samples. The uncompacted nature of these samples resulted in greater variability of drying rates than more compact samples. This structure also provided a more varied surface for reflected lidar pulses compared to the more homogenous surface of a compact sample. Variance in the relationship between the spectrometer readings and the intensity returns from the TLS units were similar between the FARO and RIEGL units. It is important to note that we were only interested in the relative change in the spectral reflectance as measured by the spectrometer and the intensity values of the TLS. Because conditions in the spectrometer sampling and the lidar scanning were consistent, the relative difference with the change in the moisture content was successfully measured. This relative difference is not to be confused with trying to determine absolute conversion values between spectrometer readings and TLS intensity. For absolute values to be compared, such as x value from spectrometer is equal to x value from TLS, then a more rigorous sampling regimen would have been required, and potentially confounding issues such as angle of sampling would have needed to be accounted for. The view angle of the spectrometer was consistent at nadir while the angle from the TLS scanner at 6 m was 18.4° (Figure 2.4). The spectrometer and the TLS scanner were functionally seeing different parts of the sample trays, but because we were only interested in if the relative change in reflectance measured by the spectrometer and the relative change in intensity measured by the TLS units were correlated, this difference in angle wasn't of concern.

2.5.3 *TLS Metrics & Moisture*

We evaluated a range of metrics that can be derived from lidar pulse intensity. Of the 7 metrics evaluated, mean intensity per sample and standard deviation of intensity values per sample produced the most robust models. Broken stick linear regression models had high coefficients of determination, but relationships were strongest when samples had a moisture content greater than 100%. At these moisture content levels; the strong relationship was likely only due to surface water evaporation. This result suggests lidar-based fuel moisture sensing will not be reliable in informing decisions based on fuel moisture content less than 30%, which is typically required for prescribed burn planning (Pollet and Brown, 2007; Wade, 2013, p. 201). However, lidar-based measurements could be helpful in remote stations that detect when live and dead fuel moistures are curing and potentially available for wildfires.

That intensity was related to dead fuel moisture levels is consistent with other studies that have shown a relationship between lidar intensity and live leaf moisture content or building material moisture content. That we also found a relationship between the standard deviation of pulses per sample tray and fuel moisture is a more novel finding. It is observable that the surface of a sample becomes more homogeneous in its reflectance as it dries (Figure 2.2). With leaf litter, this is likely due to the fact that the litter will have varying levels of moisture content between the upper leaves that will dry faster relative to the lower leaves that will dry more slowly. This is more pronounced in the samples that were less compacted, such as long leaf pine. Also, the samples tended to be more compact when fully saturated, giving a more uniform surface with less variation in angles for the lidar pulses to reflect off.

2.5.4 *Angle and Distance & TLS Metrics*

We also evaluated if angle of samples relative to the ground and distance of samples from scanner influenced lidar intensity returns and how results differed between PS and TOF sensors. While a strong relationship was found between laser pulse return intensity and fuel moisture, the relationship deteriorated with distance from the scanner. This result was consistent between PS and TOF scanners. Coefficients of the relationship between intensity and moisture also changed as distance increased (Table 2.4, supplemental Figure 6.S2.1). The TOF scanner maintained a stronger relationship as distance increased while the PS scanner only had a strong relationship at

close ranges. These findings are limited to a single study and are not sufficient to infer that TOF will always perform better than PS for fuel moisture characterization. However, it is a significant finding that the type of lidar technology, power of the laser, and potentially the size of the pulse footprint, can affect the relationship. The footprint of the TOF RIEGL scanner is significantly larger than the footprint of the PS FARO scanner (Table 2.3). Subsequently, each lidar return from the RIEGL is effectively sampling a larger area. Because of the larger footprint size of the RIEGL, it is more likely that (especially at further distances) the returned intensity value is a mixture of the reflectance from the materials inside the tray and the tray edge, and potentially the area outside the tray. This is likely minimized by the fact the RIEGL registers multiple returns per pulse, so the energy reflected from outside the tray should be returning to the RIEGL as a separate pulse return. It is unclear how much of an affect this had on the deteriorating strength of the relationship between intensity and moisture as distance increased.

For this study, we were interested if TLS can be used in the field, where variability is inherent in the ground surface. As such, we were interested in the relative position of the samples to the ground and did not conduct an exhaustive analysis of the loss of return intensity based on true angle of incidence. The angle of incidence of each lidar pulse is determined not only by the orientation of the sample relative to the ground, but also the distance of each sample from the scanner (Figure 2.4). When determining regression lines for the samples at the 3 tested angles, the Y intercept for all 45^{o} and 90^{o} samples was greater than the intercept for the 0^{o} samples (supplemental Figure 6.S2.3), indicating that they returned more energy than the 0^{o} samples. With a single exception of fully saturated pine boards located 3 m from the FARO scanner, there was no significant difference between the regression coefficient with samples at 45^{o} compared to samples at 0^{o} relative to the ground. While numerous samples did demonstrate a significant difference between regression coefficients with samples at 90^{o} compared to samples at 0^{o}, these findings still present strong evidence that TLS intensity values maintain a consistent relationship to moisture content at least until the ground surface is at a greater than 45^{o} angle of incidence. Further, it is important to consider that a significant difference in regression coefficients is determined not only by the linear trend of the data but also the spread of the data. Data clustered more tightly around the regression line will be more likely to have a significant difference between coefficients with a smaller change. Therefore, the RIEGL data, which tended to have a larger coefficient of determination than the FARO data, was more likely to have a significant difference

in regression coefficients with a smaller change in the coefficient values. Past studies that have looked at the effect of angle on intensity returns as they relate to moisture content have had mixed results (Hancock et al., 2017; Junttila et al., 2016; Zhu et al., 2015). That angle influences the amount of energy returned is objectively true, but at what point that change degrades relationships between moisture content and intensity of return has numerous additional variables, such as the specular nature of the reflecting surface. We speculate that angle will have less of an effect on reflectance relationships with moisture content when the surface observed is a fuel bed on the ground rather than individual leaves on a tree simply due to a more uniform and less complex spatial arrangement of surfaces.

2.5.4.1 Intensity Calibration

Calibration of intensity values can have several different meanings. Interscan calibration can be done to insure that returned values are comparable between scans taken at different times in different conditions or that two different types of scanners are returning comparable values. We normalized the intensity values on a scale of 0 to 1 to facilitate the comparison between scanners but this wasn't a true calibration to determine a transformation value that x value from the FARO scanner = x value from the RIEGL. The purpose of this study was not to derive coefficients to allow for the conversion of intensity values between two manufacturers of TLS units. Rather we were interested in if the two scanners detected the relative change and if one type of lidar technology outperformed the other in regard to its ability to quantify moisture content.

Calibration of intensity values can also be done to try and determine reflectance. This has been done in numerous studies utilizing TLS intensity values (Elsherif et al., 2018; Kaasalainen et al., 2009; Kashani et al., 2015; Tan et al., 2019). For our results to be applied in the field, distance calibration to model actual reflectance would need to be done to determine fuel moisture content at locations different than the distances sampled in this study.

2.5.5 *Model Coefficients*

The purpose of this study was to explore the relationships between different metrics derivable from TLS scans and known fuel moisture levels of samples in a laboratory setting. Our initial results indicate that this methodology has promise for future field applications to estimate fuel moisture of forest litter from TLS intensity returns. Our results, with high levels of

significance and high coefficients of determination, show that model development for field applications is possible. A variable model with distance from scanner incorporated will be necessary to provide reliable results. Further, most lidar datasets do not have calibrated intensity values, and the intensity values generally are relativized to a range of minimum and maximum of intensity values returned within a scan. This inherently makes comparison between scans difficult. There are also numerous environmental factors that can influence lidar return values such as temperature and humidity (Li et al., 2021; Strand et al., 2003). We performed our experiment in a controlled laboratory environment where we could be reasonably certain that no external factors would impact intensity return values between scans on different days.

2.5.6 *Future Research*

Given the limitations of using TLS intensity values listed above, the next step for this application of TLS to fuel moisture measurements is to take the scanners into the field for real-world data collection. This study provides the background and regression analysis parameters for application to field-collected data. The goal is to operationalize lidar scanning to quantify fuel moisture levels beyond the use of TLS for fine scale moisture mapping from a stationary location. More research needs to be done to look at potentially calibrating the intensity values for distance. Beyond simple distance calibration, it should also be investigated if the relationship between standard deviation and moisture is affected by distance. Further, we used “pure” fuel samples of leaves from a single species. More work is needed to determine if a generalized model can be produced that can be applied to mixed fuel beds found in field settings. If a reliable calibration to convert intensity to reflectance can be done, then this process has potential for mapping larger areas using drones and mobile lidar units. A drone-based lidar unit sampling at 1550 nm wavelengths could cover a much larger area with a more consistent distance from ground than a stationary tripod mounted TLS.

Applications beyond fuel moisture mapping are numerous. A drone-based lidar unit could also be used for detection and verification of wetland below canopy by isolating only the ground returns and determining locations of inundated soils and vegetation. While ALS has been used to detect inundated areas under canopy (Lang et al., 2020), a drone-based approach would allow for the intentional selection of lidar sensor using 1550 nm wavelength as well as greater temporal

resolution of resampling. Any query where detection of ground moisture is important could take advantage of the benefits of using an active sensor over a passive sensor spectroradiometer.

2.6 Conclusion

Fuel moisture is a critical variable for wildland fire management but costly and inefficient to sample with traditional methods. Drone-based techniques using spectral reflectance values are being developed (Barber et al., 2021; Levy and Johnson, 2021) to estimate moisture levels at a fine spatial scale, but the use of active sensors such as lidar can present advantages over passive sensors. Specifically, lidar can penetrate through small gaps in forest cover to derive measurements for fine-scale terrain mapping. This characteristic makes it possible to derive information about ground moisture content via intensity values of surfaces that are not detectable by passive sensors. As further studies evaluate the application of lidar for moisture sampling, this developing research will be of great interest for prescribed fire managers and scientists working on fire behavior prediction and fire ecology.

Because of weaker relationships with lower fuel moisture values, there may be limitations to the use of TLS to inform decisions about wildland fire behavior, but it can be useful to determine moisture gradients, seasonal shifts in fuel availability for combustion, and the detection of areas with high moisture and water content such as seeps and small wetlands. These are preliminary findings that indicate that active sensors such as lidar have a potential use to quantify moisture content based on the intensity and variation of intensity values. To further evaluate this method, field studies are needed to measure TLS coupled with field measurements of litter moisture to verify the ability of TLS to quantify fuel moisture outside of a laboratory environment. This study sets the groundwork for future use of lidar as a moisture detection tool that will allow for rapid, onsite, and continuous quantification of forest litter moisture content.

2.7 References

ASD, 2017. ASD FieldSpec 4 Wide-Res Field Spectroradiometer https://www.malvernpanalytical.com/.

Barber, N., Alvarado, E., Kane, V.R., Mell, W.E., Moskal, L.M., 2021. Estimating Fuel Moisture in Grasslands Using UAV-Mounted Infrared and Visible Light Sensors. Sensors 21, 6350. https://doi.org/10.3390/s21196350

Bowyer, P., Danson, F.M., 2004. Sensitivity of spectral reflectance to variation in live fuel moisture content at leaf and canopy level. Remote Sens. Environ., Forest Fire Prevention and Assessment 92, 297–308. https://doi.org/10.1016/j.rse.2004.05.020

Bright, B.C., Hudak, A.T., McGaughey, R., Andersen, H.-E., Negrón, J., 2013. Predicting live and dead tree basal area of bark beetle affected forests from discrete-return lidar. Can. J. Remote Sens. 39, S99–S111.
Calders, K., Adams, J., Armston, J., Bartholomeus, H., Bauwens, S., Bentley, L.P., Chave, J., Danson, F.M., Demol, M., Disney, M., Gaulton, R., Krishna Moorthy, S.M., Levick, S.R., Saarinen, N., Schaaf, C., Stovall, A., Terryn, L., Wilkes, P., Verbeeck, H., 2020. Terrestrial laser scanning in forest ecology: Expanding the horizon. Remote Sens. Environ. 251, 112102. https://doi.org/10.1016/j.rse.2020.112102
Calders, K., Disney, M.I., Armston, J., Burt, A., Brede, B., Origo, N., Muir, J., Nightingale, J., 2017. Evaluation of the Range Accuracy and the Radiometric Calibration of Multiple Terrestrial Laser Scanning Instruments for Data Interoperability. IEEE Trans. Geosci. Remote Sens. 55, 2716–2724. https://doi.org/10.1109/TGRS.2017.2652721
Carson, W.W., Andersen, H.-E., Reutebuch, S.E., McGaughey, R.J., 2004. LIDAR applications in forestry–an overview, in: Proceedings of the ASPRS Annual Conference. pp. 1–9.
Ceccato, P., Gobron, N., Flasse, S., Pinty, B., Tarantola, S., 2002. Designing a spectral index to estimate vegetation water content from remote sensing data: Part 1: Theoretical approach. Remote Sens. Environ. 82, 188–197.
CloudCompare [Computer Software]; Version 2.11; 2019. Available online: http://www.cloudcompare.org (accessed on 1 March 2021)., 2019. . (GPL software).
Countryman, C.M., 1974. Moisture in living fuels affects fire behavior. Fire Manag. 35 10-14 35, 10–14.
Danson, F.M., Gaulton, R., Armitage, R.P., Disney, M., Gunawan, O., Lewis, P., Pearson, G., Ramirez, A.F., 2014. Developing a dual-wavelength full-waveform terrestrial laser scanner to characterize forest canopy structure. Agric. For. Meteorol. 198, 7–14.
Datt, B., 1999. Remote Sensing of Water Content in Eucalyptus Leaves. Aust. J. Bot. 47, 909–923. https://doi.org/10.1071/bt98042
Di Biase, V., Hanssen, R.F., Vos, S.E., 2021. Sensitivity of Near-Infrared Permanent Laser Scanning Intensity for Retrieving Soil Moisture on a Coastal Beach: Calibration Procedure Using In Situ Data. Remote Sens. 13, 1645. https://doi.org/10.3390/rs13091645
Dragozi, E., Giannaros, T.M., Kotroni, V., Lagouvardos, K., Koletsis, I., 2021. Dead Fuel Moisture Content (DFMC) Estimation Using MODIS and Meteorological Data: The Case of Greece. Remote Sens. 13, 4224. https://doi.org/10.3390/rs13214224
Dubayah, R.O., Drake, J.B., 2000. Lidar remote sensing for forestry. J. For. 98, 44–46.
Elsherif, A., Gaulton, R., Mills, J., 2018. Estimation of vegetation water content at leaf and canopy level using dual-wavelength commercial terrestrial laser scanners. Interface Focus 8, 20170041.
Elsherif, A., Gaulton, R., Mills, J.P., 2019a. The potential of dual-wavelength terrestrial laser scanning in 3d canopy fuel moisture content mapping. ISPRS Geospatial Week 2019.
Elsherif, A., Gaulton, R., Shenkin, A., Malhi, Y., Mills, J., 2019b. Three dimensional mapping of forest canopy equivalent water thickness using dual-wavelength terrestrial laser scanning. Agric. For. Meteorol. 276, 107627.
FARO, n.d. Scene [Computer Software]; Version 2019.2 (7.5.5.4303); FARO: Lake Mary, FL, USA. 2021. Available online: http://www.faro.com (accessed on 25 August 2023).
Flannigan, M.D., Wotton, B.M., Marshall, G.A., De Groot, W.J., Johnston, J., Jurko, N., Cantin, A.S., 2016. Fuel moisture sensitivity to temperature and precipitation: climate change implications. Clim. Change 134, 59–71.
Garroway, K., Hopkinson, C., Jamieson, R., 2011. Surface moisture and vegetation influences on lidar intensity data in an agricultural watershed. Can. J. Remote Sens. 37, 275–284. https://doi.org/10.5589/m11-036
Gaulton, R., Danson, F.M., Pearson, G., Lewis, P.E., Disney, M., 2010. The Salford Advanced Laser Canopy Analyser (SALCA): A multispectral full waveform LiDAR for improved vegetation characterisation, in: Proceedings of the Remote Sensing and Photogrammetry Society Conference, Remote Sensing and the Carbon Cycle, London, UK.
Gaulton, R., Danson, F.M., Ramirez, F.A., Gunawan, O., 2013. The potential of dual-wavelength laser scanning for estimating vegetation moisture content. Remote Sens. Environ. 132, 32–39. https://doi.org/10.1016/j.rse.2013.01.001

Gergel, D.R., Nijssen, B., Abatzoglou, J.T., Lettenmaier, D.P., Stumbaugh, M.R., 2017. Effects of climate change on snowpack and fire potential in the western USA. Clim. Change 141, 287–299. https://doi.org/10.1007/s10584-017-1899-y

Gillon, D., Dauriac, F., Deshayes, M., Valette, J.C., Moro, C., 2004. Estimation of foliage moisture content using near infrared reflectance spectroscopy. Agric. For. Meteorol. 124, 51–62.

Haines, D.A., Frost, J.S., 1978. Weathering effects on fuel moisture sticks: corrections and recommendations. Department of Agriculture, Forest Service, North Central Forest Experiment ….

Hancock, S., Gaulton, R., Danson, F.M., 2017. Angular Reflectance of Leaves With a Dual-Wavelength Terrestrial Lidar and Its Implications for Leaf-Bark Separation and Leaf Moisture Estimation. IEEE Trans. Geosci. Remote Sens. 55, 3084–3090. https://doi.org/10.1109/TGRS.2017.2652140

Hao, X., Qu, J.J., 2007. Retrieval of real-time live fuel moisture content using MODIS measurements. Remote Sens. Environ., The Application of Remote Sensing to Fire Research in the Eastern United States 108, 130–137. https://doi.org/10.1016/j.rse.2006.09.033

Hasegawa, H., 2006. Evaluations of LIDAR reflectance amplitude sensitivity towards land cover conditions. Bull. Geogr. Surv. Inst. 53, 43–50.

Hudak, A.T., Evans, J.S., Stuart Smith, A.M., 2009. LiDAR utility for natural resource managers. Remote Sens. 1, 934–951.

Jin, J., De Sloover, L., Verbeurgt, J., Stal, C., Deruyter, G., Montreuil, A.-L., De Maeyer, P., De Wulf, A., 2020. Measuring Surface Moisture on a Sandy Beach based on Corrected Intensity Data of a Mobile Terrestrial LiDAR. Remote Sens. 12, 209. https://doi.org/10.3390/rs12020209

Jolly, W.M., 2007. Sensitivity of a surface fire spread model and associated fire behaviour fuel models to changes in live fuel moisture. Int. J. Wildland Fire 16, 503–509.

Junttila, S., Hölttä, T., Puttonen, E., Katoh, M., Vastaranta, M., Kaartinen, H., Holopainen, M., Hyyppä, H., 2021. Terrestrial laser scanning intensity captures diurnal variation in leaf water potential. Remote Sens. Environ. 255, 112274.

Junttila, S., Sugano, J., Vastaranta, M., Linnakoski, R., Kaartinen, H., Kukko, A., Holopainen, M., Hyyppä, H., Hyyppä, J., 2018. Can Leaf Water Content Be Estimated Using Multispectral Terrestrial Laser Scanning? A Case Study With Norway Spruce Seedlings. Front. Plant Sci. 9.

Junttila, S., Vastaranta, M., Liang, X., Kaartinen, H., Kukko, A., Kaasalainen, S., Holopainen, M., Hyyppä, H., Hyyppä, J., 2017. Measuring Leaf Water Content with Dual-Wavelength Intensity Data from Terrestrial Laser Scanners. Remote Sens. 9, 8. https://doi.org/10.3390/rs9010008

Junttila, S., Vastaranta, M., Liang, X., Kaartinen, H., Kukko, A., Kaasalainen, S., Holopainen, M., Hyyppä, H., Hyyppä, J., 2016. Measuring leaf water content with dual-wavelength intensity data from terrestrial laser scanners. Remote Sens. 9, 8.

Kaasalainen, S., Krooks, A., Kukko, A., Kaartinen, H., 2009. Radiometric Calibration of Terrestrial Laser Scanners with External Reference Targets. Remote Sens. 1, 144–158. https://doi.org/10.3390/rs1030144

Kashani, A.G., Olsen, M.J., Parrish, C.E., Wilson, N., 2015. A review of LiDAR radiometric processing: From ad hoc intensity correction to rigorous radiometric calibration. Sensors 15, 28099–28128.

Keane, R.E., Gray, K., 2013. Comparing three sampling techniques for estimating fine woody down dead biomass. Int. J. Wildland Fire 22, 1093–1107. https://doi.org/10.1071/WF13038

Kemppinen, J., Niittynen, P., Riihimäki, H., Luoto, M., 2018. Modelling soil moisture in a high-latitude landscape using LiDAR and soil data. Earth Surf. Process. Landf. 43, 1019–1031. https://doi.org/10.1002/esp.4301

Korpela, I., Ørka, H.O., Hyyppä, J., Heikkinen, V., Tokola, T., 2010. Range and AGC normalization in airborne discrete-return LiDAR intensity data for forest canopies. ISPRS J. Photogramm. Remote Sens. 65, 369–379.

Krooks, A., Kaasalainen, S., Hakala, T., Nevalainen, O., 2013. Correction of intensity incidence angle effect in terrestrial laser scanning. ISPRS Ann Photogramm Remote Sens Spat Inf Sci 2, 145–150.

Lang, M.W., Kim, V., McCarty, G.W., Li, X., Yeo, I.-Y., Huang, C., Du, L., 2020. Improved detection of inundation below the forest canopy using normalized LiDAR intensity data. Remote Sens. 12, 707.

Levy, J.S., Johnson, J.T.E., 2021. Remote Soil Moisture Measurement from Drone-Borne Reflectance Spectroscopy: Applications to Hydroperiod Measurement in Desert Playas. Remote Sens. 13, 1035. https://doi.org/10.3390/rs13051035
Li, Y., Duthon, P., Colomb, M., Ibanez-Guzman, J., 2021. What Happens for a ToF LiDAR in Fog? IEEE Trans. Intell. Transp. Syst. 22, 6670–6681. https://doi.org/10.1109/TITS.2020.2998077
Loudermilk, E.L., Hiers, J.K., O'Brien, J.J., Mitchell, R.J., Singhania, A., Fernandez, J.C., Cropper, W.P., Slatton, K.C., 2009. Ground-based LIDAR: a novel approach to quantify fine-scale fuelbed characteristics. Int. J. Wildland Fire 18, 676–685.
Ma, W., Zhai, L., Pivovaroff, A., Shuman, J., Buotte, P., Ding, J., Christoffersen, B., Knox, R., Moritz, M., Fisher, R., 2021. Assessing climate change impacts on live fuel moisture and wildfire risk using a hydrodynamic vegetation model. Biogeosciences. https://doi.org/10.5194/bg-18-4005-2021
Makowiecki, A.S., Steinbrenner, J.E., Wimer, N.T., Glusman, J.F., Lapointe, C.B., Daily, J.W., Hamlington, P.E., Rieker, G.B., 2020. Dual frequency comb spectroscopy of solid fuel pyrolysis and combustion: Quantifying the influence of moisture content in Douglas fir. Fire Saf. J. 116, 103185.
Matthews, S., 2014. Dead fuel moisture research: 1991–2012. Int. J. Wildland Fire 23, 78–92.
Paltridge, G.W., Mitchell, R.M., 1990. Atmospheric and viewing angle correction of vegetation indices and grassland fuel moisture content derived from NOAA/AVHRR. Remote Sens. Environ. 31, 121–135. https://doi.org/10.1016/0034-4257(90)90061-P
Pimont, F., Parsons, R., Rigolot, E., de Coligny, F., Dupuy, J.-L., Dreyfus, P., Linn, R.R., 2016. Modeling fuels and fire effects in 3D: model description and applications. Environ. Model. Softw. 80, 225–244.
Plyler, E.K., Sleator, W.W., 1931. Further study of the absorption of infrared radiation by water vapor. Phys. Rev. 37, 1493.
Pollet, J., Brown, A., 2007. Fuel moisture sampling guide. Bur. Land Manag. Utah State Off. Salt Lake City UT USA Available Httpswww Wfas Netnfmdreferencesfmg Pdf Verified 10 March 2017.
Ponomarev, O.A., Zakir'ianov, F.K., Terpugov, E.L., Fesenko, E.E., 2001. Absorption of infrared radiation by a thin water layer. Biofizika 46, 402–407.
Qi, Y., Dennison, P.E., Jolly, W.M., Kropp, R.C., Brewer, S.C., 2014. Spectroscopic analysis of seasonal changes in live fuel moisture content and leaf dry mass. Remote Sens. Environ. 150, 198–206.
Raj, T., Hashim, F.H., Huddin, A.B., Ibrahim, M.F., Hussain, A., 2020. A Survey on LiDAR Scanning Mechanisms. Electronics 9, 741. https://doi.org/10.3390/electronics9050741
Riegl, 2021. RiScan Pro.
Rossa, C.G., Fernandes, P.M., 2018. Live fuel moisture content: the 'pea under the mattress' of fire spread rate modeling? Fire 1, 43.
Rothermel, R.C., 1983. How to predict the spread and intensity of forest and range fires. US Department of Agriculture, Forest Service, Intermountain Forest and Range ….
Rothermel, R.C., 1972. A mathematical model for predicting fire spread in wildland fuels. Res Pap INT-115 Ogden UT US Dep. Agric. Intermt. For. Range Exp. Stn. 40 P 115.
Rowell, E., Prichard, S., Varner, J.M., Shearman, T.M., 2022. Re-envisioning Fire and Vegetation Feedbacks, in: Speer, K., Goodrick, S. (Eds.), Wildland Fire Dynamics. Cambridge University Press, Cambridge, pp. 156–182. https://doi.org/10.1017/9781108683241.006
Rowell, E., Seielstad, C., 2012. Characterizing grass, litter, and shrub fuels in longleaf pine forest pre-and post-fire using terrestrial LiDAR. Proc. SilviLaser 16–19.
Rowell, E.M., Seielstad, C.A., Ottmar, R.D., 2015. Development and validation of fuel height models for terrestrial lidar–RxCADRE 2012. Int. J. Wildland Fire 25, 38–47.
San José Alonso, J.I., Martínez Rubio, J., Fernández Martín, J.J., García Fernández, J., 2011. Comparing Time-Of and Phase-Shift the Survey of the Royal Pantheon in the Basilica of San Isidoro (LEÓN). ISPRS - Int. Arch. Photogramm. Remote Sens. Spat. Inf. Sci. 3816, 377–385. https://doi.org/10.5194/isprsarchives-XXXVIII-5-W16-377-2011
Stavros, E.N., Coen, J., Peterson, B., Singh, H., Kennedy, K., Ramirez, C., Schimel, D., 2018. Use of imaging spectroscopy and LIDAR to characterize fuels for fire behavior prediction. Remote Sens. Appl. Soc. Environ. 11, 41–50. https://doi.org/10.1016/j.rsase.2018.04.010
Strand, M.P., Witherspoon, N.H., Holloway Jr, J.H., Tinsley, K.R., Petee, D.A., Taylor Jr, J.S., Branham, E.A., Thomas, J.P., 2003. Environmental factors impacting the performance of airborne lidar

sensors in the surf zone, in: Detection and Remediation Technologies for Mines and Minelike Targets VIII. SPIE, pp. 274–283.
Suchocki, C., 2020. Comparison of Time-of-Flight and Phase-Shift TLS Intensity Data for the Diagnostics Measurements of Buildings. Materials 13, 353. https://doi.org/10.3390/ma13020353
Suchocki, C., Katzer, J., 2018. Terrestrial laser scanning harnessed for moisture detection in building materials – Problems and limitations. Autom. Constr. 94, 127–134. https://doi.org/10.1016/j.autcon.2018.06.010
Suchocki, C., Katzer, J., Rapiński, J., 2018. Terrestrial Laser Scanner as a Tool for Assessment of Saturation and Moisture Movement in Building Materials. Period. Polytech. Civ. Eng. 62, 694–699. https://doi.org/10.3311/PPci.11406
Tan, K., Chen, J., Qian, W., Zhang, W., Shen, F., Cheng, X., 2019. Intensity Data Correction for Long-Range Terrestrial Laser Scanners: A Case Study of Target Differentiation in an Intertidal Zone. Remote Sens. 11, 331. https://doi.org/10.3390/rs11030331
Tian, Q., Tong, Q., Pu, R., Guo, X., Zhao, C., 2001. Spectroscopic determination of wheat water status using 1650-1850 nm spectral absorption features. Int. J. Remote Sens. 22, 2329–2338. https://doi.org/10.1080/01431160118199
Tucker, C.J., 1980. Remote sensing of leaf water content in the near infrared. Remote Sens. Environ. 10, 23–32. https://doi.org/10.1016/0034-4257(80)90096-6
Viney, N.R., 1991. A review of fine fuel moisture modelling. Int. J. Wildland Fire 1, 215–234.
Vinnikov, K.Y., Robock, A., Qiu, S., Entin, J.K., Owe, M., Choudhury, B.J., Hollinger, S.E., Njoku, E.G., 1999. Satellite remote sensing of soil moisture in Illinois, United States. J. Geophys. Res. Atmospheres 104, 4145–4168. https://doi.org/10.1029/1998JD200054
Wade, D., 2013. Fuel moisture and prescribed burning. South Fire Exch Fact Sheet 5, 5–8.
Wang, J., Xu, R., Yang, S., 2008. Estimation of plant water content by spectral absorption features centered at 1,450 nm and 1,940 nm regions. Environ. Monit. Assess. 157, 459. https://doi.org/10.1007/s10661-008-0548-3
Wang, L., Qu, J.J., 2009. Satellite remote sensing applications for surface soil moisture monitoring: A review. Front. Earth Sci. China 3, 237–247. https://doi.org/10.1007/s11707-009-0023-7
Watanabe, K., Mansfield, S.D., Avramidis, S., 2011. Application of near-infrared spectroscopy for moisture-based sorting of green hem-fir timber. J. Wood Sci. 57, 288–294. https://doi.org/10.1007/s10086-011-1181-2
Wulder, M.A., White, J.C., Nelson, R.F., Næsset, E., Ørka, H.O., Coops, N.C., Hilker, T., Bater, C.W., Gobakken, T., 2012. Lidar sampling for large-area forest characterization: A review. Remote Sens. Environ. 121, 196–209.
Yebra, M., Dennison, P.E., Chuvieco, E., Riaño, D., Zylstra, P., Hunt, E.R., Danson, F.M., Qi, Y., Jurdao, S., 2013. A global review of remote sensing of live fuel moisture content for fire danger assessment: Moving towards operational products. Remote Sens. Environ. 136, 455–468. https://doi.org/10.1016/j.rse.2013.05.029
Zahiri, Z., Laefer, D.F., Gowen, A., 2021. Characterizing building materials using multispectral imagery and LiDAR intensity data. J. Build. Eng. 44, 102603. https://doi.org/10.1016/j.jobe.2021.102603
Zhu, X., Wang, T., Darvishzadeh, R., Skidmore, A.K., Niemann, K.O., 2015. 3D leaf water content mapping using terrestrial laser scanner backscatter intensity with radiometric correction. ISPRS J. Photogramm. Remote Sens. 110, 14–23.

Chapter 3. Drone Based, Multispectral Photogrammetric Point Clouds to Classify Fire Severity at Differing Canopy Height Strata

Jonathan L. Batchelor , Andrew T. Hudak , Akira Kato and L. Monika Moskal

3.1 Abstract

Utilizing digital aerial photogrammetry (dDAP), also sometimes referred to as structure from motion, we generated three-dimensional photogrammetric point clouds to quantify the effects of fire at various canopy height strata. Our research was conducted during a prescribed burn at Fort Jackson, South Carolina, where we collected both RGB and multispectral imagery pre- and post-fire for five plots, as well as for two control plots that were not burned. The plots measured approximately 0.2 ha in size. Photogrammetric point clouds were generated from the multispectral and RGB imagery, and NDVI values were calculated for each point using the NIR and red reflectance values. Point clouds were normalized by removing elevation determined from airborne lidar digital terrain models, and were then divided into 2-meter height stratum layers. This allowed for the comparison of point NDVI values for different canopy height strata pre- and post-fire, as well as the generation of orthoimages of the ground and surface vegetation only, tree canopy only, and top-down elevated view. Our results showed that the prescribed fire had a very large effect size on NDVI values up to 6 m in height, with only small effects above 6 m and within the control plots. We were also able to classify ground cover under the canopy in areas that would normally be occluded from overhead imagery, with 87% accuracy. Finally, we demonstrated that removing occluding tall vegetation increases dNDVI values and can produce a more accurate assessment of fire effects on ground and understory vegetation. Satellite imagery is limited to top-down views and cannot separate understory fire effects from overstory fire effects.

3.2 1. Introduction

Fire severity and effects on vegetation differ spatially across burns, both horizontally and vertically (Agee, 1996; Bessie and Johnson, 1995; Rothermel, 1991; Wagner, 1977). The quantification of fire severity and defining terms used have been the subject of much research

(Keeley, 2009), with definitions often determined by the scale at which fire effects are observed. Fire effects quantified at the landscape level generally rely on satellite imagery consisting only of two-dimensional, top-down imagery (Szpakowski and Jensen, 2019). To derive fire severity estimates that incorporate vertical strata conditions, visual assessments of field plots are typically performed. The composite burn index is a field method that uses height strata to evaluate fire effects (Key and Benson, 2006; Saberi et al., 2022); however, field sampling techniques still rely on subjective assessment and on generalizing conditions spatially, both horizontally and vertically.

A common modern method for deriving 3D models of forests is Airborne Laser Scanning (ALS). ALS has been used to quantify three-dimensional forest structure changes caused by fire and relate them to both satellite and drone imagery (Filippelli et al., 2019; Kato et al., 2019; McCarley et al., 2017; Viana-Soto et al., 2022). In areas where ALS was acquired both before and after a fire, fire severity can be quantified by the change in aboveground point distributions (Hoe et al., 2018). Although more limited in spatial coverage, Terrestrial Laser Scanning (TLS) can also be employed to quantify fire severity at strata of different heights based on point distributions (Kato et al., 2019). One limitation of ALS and TLS is that the spectral reflectance is not captured, except for the energy returned from each pulse (intensity). These methods still typically focus on overstory tree canopies and lack the ability to measure fine-scale changes in surface vegetation, largely because of the occlusion of the surface vegetation or fuel bed by overstory (or understory) vegetation.

3.2.1 *Limitations of 2D imagery*

Typically, the use of aerial imagery for fire severity assessment is limited to top-down, two-dimensional representations of structurally complex forested landscapes. Such images are very effective for detecting changes in overstory vegetation after a fire disturbance event (Kane et al., 2013; Lydersen et al., 2016), but any change in the understory may be difficult to detect, as the upper canopy can partially or totally occlude the lower vegetation. This is potentially problematic because a fast-moving, low-severity fire can remove all surface vegetation while leaving the upper canopy unscathed (Wright and Agee, 2004). Fires often have mixed severities across the impacted area. Although severely burned areas may experience total tree mortality, other areas within the fire perimeter may not have burned at all, or only experienced surface fires. Topography, moisture, and wind patterns are some of the factors that can lead to mixed-severity fires (Perry et al., 2011).

In such mosaicked fires, the ability to quantify surface fire compared to crown fire could enable a much more accurate assessment of overall fire severity. In areas of high-severity crown fires, there may be little to no occlusion of the ground post-fire, but in areas that have experienced a severe surface fire that did not move into the canopy, the live crown foliage can mask the severity on the understory in burn indices that rely on top-down imagery (Miller et al., 2009). In areas of relatively open overstory, there is still a large percentage of the ground level occluded under each individual tree crown. Deriving a single severity value for an area provides no information regarding the ratio of crown fire to surface fire. Although more limited in the area covered compared to global satellite imagery, new advances in drone digital aerial photogrammetry (dDAP) can provide a method of separating overstory and understory fire severity along with fine-scale fuel type mapping.

3.2.2 *Drone Digital Aerial Photogrammetry (dDAP)*

Digital aerial photogrammetry (often called Structure from Motion, SfM) is used to create photogrammetric point clouds and orthoimagery mosaics from a collection of overhead images. With the increasing availability of consumer drones and processing software, drone imagery has become a staple in ecological monitoring (Colomina and Molina, 2014; Hardin and Hardin, 2010; Sun et al., 2021). In addition to traditional RGB imagery, drones with multispectral cameras are now employed to rapidly assess vegetation health and conditions (Fawcett et al., 2020).

A major limitation of drone imagery in estimating pre-fire fuel loads is that the understory in most forested ecosystems is obscured by tree overstory and/or understory canopy. The areas that were not visible could not be photographed. However, forested ecosystems with short fire return intervals tend to have a relatively open canopy (Beaty and Taylor, 2001). An open canopy allows oblique angles from the camera to capture tree stems, understory vegetation, and ground cover. These oblique angles allow for a much more complete three-dimensional model of an area, including the ground and surface vegetation, even under tree canopies that would occlude normal top-down imagery. Because photogrammetric point clouds are generated from a multitude of images, what may be obscured in one image could be visible in another. Specifically, a nadir image directly above a tree will have all the ground under the tree obscured; however, the ground under that tree will be visible in the images taken in the surrounding area, depending on the height of the drone. With sufficient overlap between photos, it is possible to generate an orthoimage of just the surface vegetation, effectively removing all tall vegetation from the image. While drone images

are top-down nadir photos, the subsequent photogrammetric point clouds and derived orthoimagery are not. Instead, orthoimagery is derived from rasters from subsections of the point cloud, making them fundamentally different from top-down images such as those produced from aerial or satellite sensors.

Photogrammetric point clouds derived from imagery retain spectral information from the parent photos. RGB images produce point clouds with encoded reflectance values for the red, green, and blue sections of the electromagnetic spectrum. The same is true for 4-band multispectral imagery with near-infrared (NIR) reflectance values as an added band with high sensitivity to vegetation (Wallace et al., 2016). Photogrammetric point clouds are much more complex than a simple three-dimensional surface model. Typically, the workflow of creating an orthorectified image mosaic from drone images is to generate a photogrammetric point cloud and then create a digital surface model to drape the image mosaic over, to adjust for distortions in the imagery due to changes in elevation. However, the initial photogrammetric point cloud can be treated in the same way as an ALS point cloud and have the height values normalized by removing elevation effects, such as slope, to then be sliced at defined height strata to derive spectral indices in three dimensions. When using standard RGB images, it is possible to create basic spectral indices, such as a greenness index, that can be used to monitor post-fire regeneration (Larrinaga and Brotons, 2019). However, when using a multispectral or thermal camera, other spectral indices can be used to classify the vegetation cover and quantify disturbance effects using valuable NIR information (e.g., dNDVI).

3.2.3 *Spectral Indices*

The creation and use of spectral indices from multispectral images can be informative and can detect a multitude of ecological processes or disturbances. A vast archive of multispectral imagery from satellites has been used for decades to identify and quantify land cover and disturbances (French et al., 2008). One spectral index widely used to quantify vegetation cover and relative health is the Normalized Difference Vegetation Index (NDVI). NDVI utilizes the reflectance values of red (635–700 nm) and near-infrared (780–1400 nm) wavelengths to create a normalized scale of "greenness" (Fawcett et al., 2020; Pettorelli et al., 2005).

$$NDVI = (NIR-Red)/(NIR+Red)$$

NDVI is one of the earliest remote sensing spectral indices, and its use has increased with the availability of multispectral cameras on drones. Care must be taken to ensure that the imagery is processed correctly and that appropriate corrections are applied, such as radiometric calibration of incoming radiation levels (Huang et al., 2021). Healthy green vegetation has high reflectance in the NIR band and low reflectance in the red band, which results in an NDVI value closer to 1. Non-photosynthetic vegetation (dead, scorched, or charred vegetation) generally has lower NIR reflectance and higher red reflectance, which results in an NDVI value closer to 0 or potentially negative (Pettorelli et al., 2005). With historical pre-fire and repeated post-fire images, a differenced normalized difference vegetation index (dNDVI) is possible.

$$dNDVI = (NDVI)pre - (NDVI)post$$

The difference in NDVI can be used to gauge the severity of a fire and the change in vegetation cover (Escuin et al., 2008). The ability to quantify fire severity remotely over large areas has allowed regional fire severity maps to be produced; however, there are limitations to the accuracy of these landscape-level fire-severity mapping products, as they are limited to a top-down view that can miss changes in surface vegetation cover and fuels (Kolden et al., 2015).

NDVI values from points within the photogrammetric point clouds can be directly compared pre- and post-fire to determine the fire effect size at different canopy height strata (i.e., 0 m – 2 m, 2 m – 4m, 4 m – 6 m, etc.). Such binning can provide a more complete assessment of fire behavior, as fire impacts can subsequently be plotted on three axes (x, y, and z). Furthermore, because raster outputs can be generated from photogrammetric point clouds, it is possible to generate high-resolution NDVI rasters for the ground only (defined here as surface vegetation, ground fuels, and bare ground below 2 m), trees only, and a top-down view of trees with partially occluded ground below. This would allow the generation of dNDVI values for all three sets of rasters.

3.2.4 *Ground Cover Classification*

In addition to the change in values for spectral indices, high-resolution drone imagery allows for detailed ground cover classification. Pre-fire dDAP where the understory is adequately

visualized should allow for complete characterization of ground cover into categories such as fine vs coarse downed woody debris, bare soil, duff, surface vegetation (e.g., grasses, forbes, and small shrubs), & understory vegetation (e.g., shrubs and saplings). Post-fire dDAP should allow for the same characterization of fuels as pre-fire dDAP and enable a detailed quantification of the type of fuels consumed and the total consumption. Identification of high-intensity burn areas, such as "ghost logs" (Hudak et al., 2013), should be possible in contrasting areas of black char and white ash. The basic principles of land cover classification based on reflectance and texture used in satellite imagery classification can be applied to multispectral drone imagery (Franklin et al., 2000; Hansen et al., 2000; Puliti et al., 2018; Running et al., 1995). Previous work has been done to isolate overstory vs. understory in orthomosaic images from drone imagery (Herzog et al., 2022; Kolarik et al., 2019; Li et al., 2020), and we want to expand this work by generating a complete understory ortho image from photogrammetric point clouds and conducting a high-resolution classification.

3.2.5 *Research Questions*

The primary focus of this study is to develop the capabilities of dDAP to quantify fire effects and fire-induced vegetation change and to demonstrate the use of novel methods to process photogrammetric point clouds to generate NDVI values for strata of different heights. We address the following three specific questions:

- Is it possible to quantify fire effects at different canopy height strata, effectively creating separate severity assessments for understory vs overstory using multispectral photogrammetric point clouds?
- Is it possible to accurately classify ground cover types under a partially closed canopy (both pre- and post-fire) using orthoimagery and digital surface models derived from photogrammetric point clouds?
- How do 3D multispectral dDAP fire severity assessments, which can isolate understory vs. overstory, compare to fire severity assessments from top-down 2D satellite imagery?

Research outcomes will provide a methodology that can be used by fire ecologists and land managers to separate understory fire effects from overstory fire effects, to monitor changes in vegetation due to disturbance or regrowth with centimeter precision, and provide a tool to quantify

the potential underestimation of fire effects from aerial or satellite imagery. Additionally, understory vegetation quantification is also important for wildlife habitat quantification, restoration efforts, and hydrology.

3.3 Methods

3.3.1 *Site*

The study site was located in South Carolina, USA, on the US Army base Fort Jackson (Figure 3.1). Fort Jackson occupies 20,767 hectares, with the dominate forest type consisting of a fire adapted longleaf pine (*Pinus palustris*) with a sparkleberry (*Vaccinium arboreum*) understory. Longleaf pine forests have a relatively open canopy, allowing aerial images to capture much of the ground (Figure 3.2). The fort uses prescribed fires to burn approximately 12,000 ha every 3 years. Seven plots (approximately 0.2 ha) were placed in the areas before the burns to collect pre- and post-fire fuel measurements and drone imagery (Table 3.1). The size and locations of plots was partially dictated by existing roads that were used as fire breaks as well as the needs of other research projects associated with the burn. The plots had a naming convention to match these additional studies associated with these burns (Banach et al., 2021; Herzog et al., 2022; Hudak et al., 2020; Scharko et al., 2019; Weise et al., 2022). Two of the plots were used as controls (plots 2 & 3) and were not burned but were still flown twice, before and after the other plots were burned (plots 1, 5, 6, 24A, & 24B).

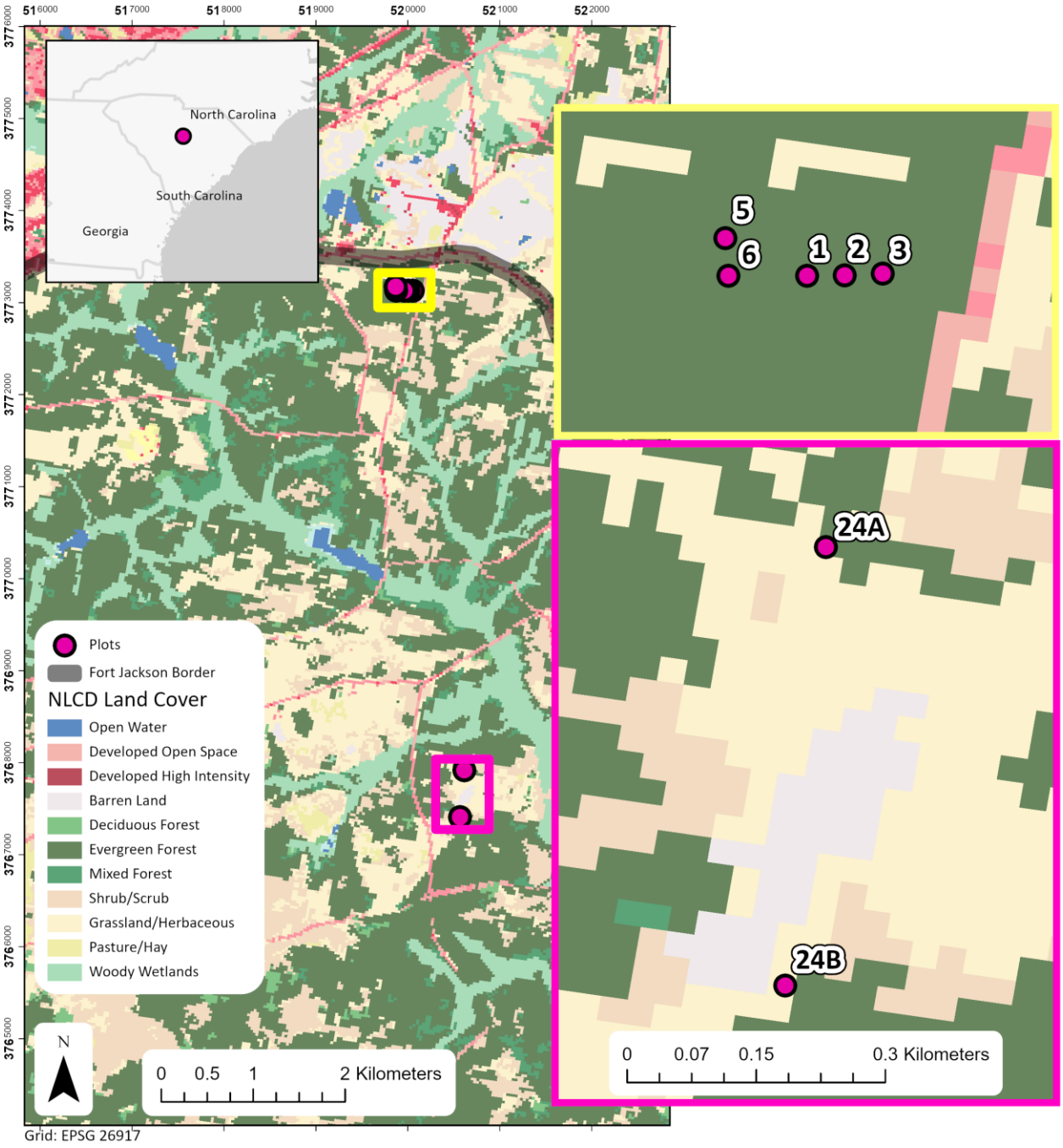

Figure 3.1. *Location of plots within Fort Jackson, near Columbia, South Carolina, USA. The 2020 National Land Cover Database (NLCD)* (Homer et al., 2012) *data in background provides the context of vegetation cover.*

Figure 3.2. *A southeast facing drone photograph of the open canopy, long leaf pine forest with cleared firebreaks between plots. The area in the lower left corner (Plot 5) had previously been burned with the area above it currently on fire (Plot 6). The area to the right was outside of the burn plot.*

Table 3.1. *Plot number, size, and time/date of each drone flight. Preexisting roads were partially used as fire breaks, so plot sizes varied. Flight times were generalized as flights averaged between 10 and 20 minutes. The times given are for RGB image collection, additional flights were required to collect multispectral imagery for some plots, and time was not recorded.*

Plot #	*Size (ha)*	*Pre-Burn Flight Time*	*Post Burn Flight Time*
1	0.18	15:00 30/4/2018	13:00 4/5/2018
5	0.15	14:00 30/4/2018	14:00 3/5/2018
6	0.19	14:00 30/4/2018	14:00 3/5/2018
24A	0.22	12:00 30/4/2018	16:00 2/5/2018
24B	0.31	10:00 30/4/2018	11:00 2/5/2018
2 (control)	0.19	15:00 30/4/2018	13:00 4/5/2018 (not burned)
3 (control)	0.2	15:00 30/4/2018	13:00 4/5/2018 (not burned)

3.3.2 *dDAP Point Clouds*

For the dDAP data, a DJI Mavic Pro drone (DJI, 2016) with a stock 12-megapixel RGB camera with a resolution of 3 cm/px at 100 m was used. A Parrot Sequoia multispectral camera (Parrot, n.d.) was also attached to the drone and images were captured in four spectral bands: Green (GRE):530-570 nm, Red (RED):640-680 nm, Red Edge (REG):730-740 nm, and NIR (NIR):770-810 nm. The resolution of the parrot Sequoia images was 9 cm/px at 100 m. For image acquisition, transects were flown over the plots at both 60 m and 120 m. Images were collected with a minimum of 80% front and side overlaps.

Image processing was performed using the photogrammetric Agisoft program, Metashape (Agisoft, 2014). Photogrammetric point clouds were generated using all bands from the parrot sequoia. Radiometric calibration of the images was performed during processing using the data recorded from the camera's sunlight sensor, as well as using a calibrated reflectance panel. Photogrammetric point clouds were also created using the RGB images from the Mavic Pro stock camera. Three-dimensional photogrammetric point clouds were created from both multispectral and RGB imagery for all plots, both before and after the fires (28 total point clouds). Each point in the resultant multispectral point clouds had the 4 sequoia spectral values associated with it. All points generated were used, as employing thresholds of minimum look angles for point generation and confidence intervals excluded a high percentage of valid vegetation points. Quality control was conducted visually to remove errant points and low-quality image inputs.

Using multispectral point clouds, the open-source program CloudCompare (CloudCompare 2019) was used to calculate the NDVI value for each point. This allowed for normalized difference vegetation index (NDVI) point clouds to be generated (Figure 3.3). Each of the seven plots (including the two control plots that were not burned), both pre- and post-burn had NDVI point clouds created. In total, there were 14 NDVI point clouds created.

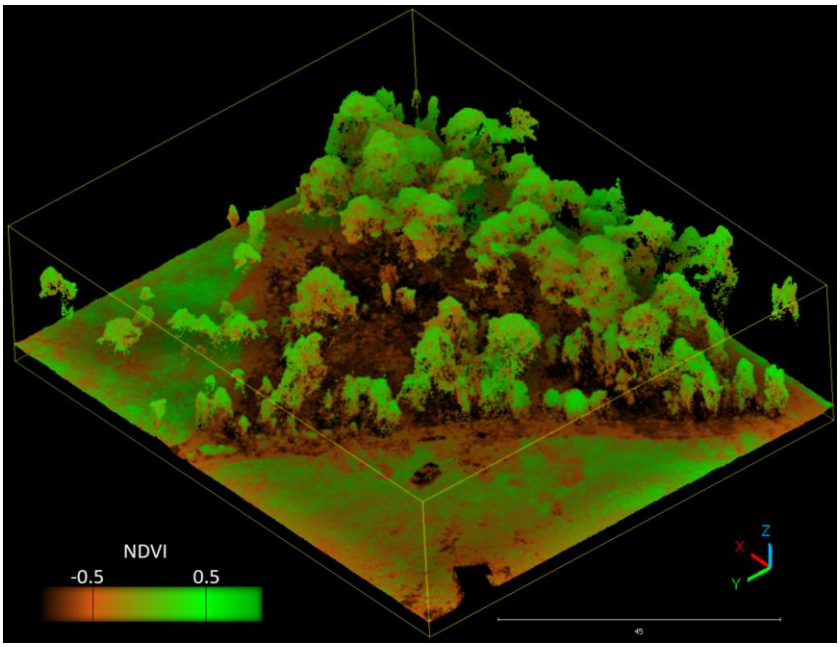

Figure 3.3. *NDVI point cloud generated from the multispectral photogrammetric point cloud of post-burn plot 24B and the surrounding area. Y is north, X is east.*

The dDAP point clouds were georectified using 2017 airborne lidar (ALS) data to perform fine-scale point-cloud matching. The use of aerial lidar and tree crown matching to georeference photogrammetric point clouds or terrestrial LiDAR point clouds is a method commonly used in place of surveying in ground control points (Batchelor et al., 2023; Hauglin et al., 2014). This ensured a direct comparison between multiple datasets without compounding location errors. A 1-m digital terrain model derived from ALS was used to "normalize" the dDAP point clouds. This normalization subtracts all ground elevation values from the dDAP point cloud values, creating a "flat" scene in which the hill slope was removed. All photogrammetric point clouds were then divided into two-meter height strata bins (Figure 3.4).

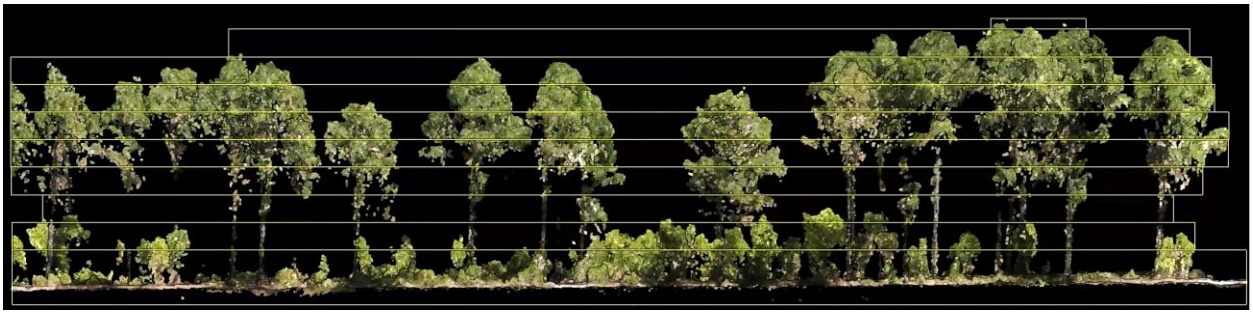

Figure 3.4. *Two-meter height strata highlighted in one of the RBG photogrammetric point clouds.*

3.3.2.1 Point Cloud Statistical Analysis

Using the height strata layers, the pre- and post-fire NDVI point clouds were compared at each site. Two sample z-tests were performed to determine if there was a change in the mean NDVI values of points within each height stratum after the fire. Cohen's d (Ben-Shachar et al., 2020; Cohen, 2013) was used to assess the effect size of the burns on the NDVI values of the points within each height stratum for the aggregated burned and control plots. The d value for Cohen's d is a measure of the number of standard deviations between the two means of the compared datasets. Thresholds of effect size were set as follows: d < 0.1, very small; d <= 0.3, small; d <= 0.5, moderate; d<= 0.8, large; and d > 1, very large. The ordinal values from small to large were subjective, and Cohen's suggested thresholds were used with the addition of the "very large" class to indicate plots in our study that had the largest effect size from fire. Cohen's d does not produce a test of significance value like a t or z test, rather the significance of effect size is subjective. Our sample sizes were very large (typically > 10,000), and with such large datasets, tests for significant differences in mean values are likely to always indicate a significant difference. Point density violin plots of pre- and post-fire NDVI values were created from the values of the point clouds to visualize the change in the distribution of the values at strata of different heights.

3.3.3 *Multispectral Orthoimage Processing*

CloudCompare was used to convert the point clouds into raster orthoimages for both multispectral photogrammetric point clouds and RGB photogrammetric point clouds. From the multispectral point clouds, 20 cm resolution orthoimages were made from all points (a top-down view of the plots) and points 2m and below (Figure 3.5). Conceptually, imagine removing all vegetation above 2 m and then take an aerial image of the ground (i.e., all points below 2 m). Points above 2m were used to create a third orthoimage raster denoting canopy cover only. The figures for all orthoimages in color infrared from all plots are included in the supplementary material (Chapter 6.2). All three sets of multispectral photogrammetric point clouds (understory-only, top-down, and tree-only) were used to create NDVI rasters of the pre- and post-burn plots, as well as dNDVI rasters.

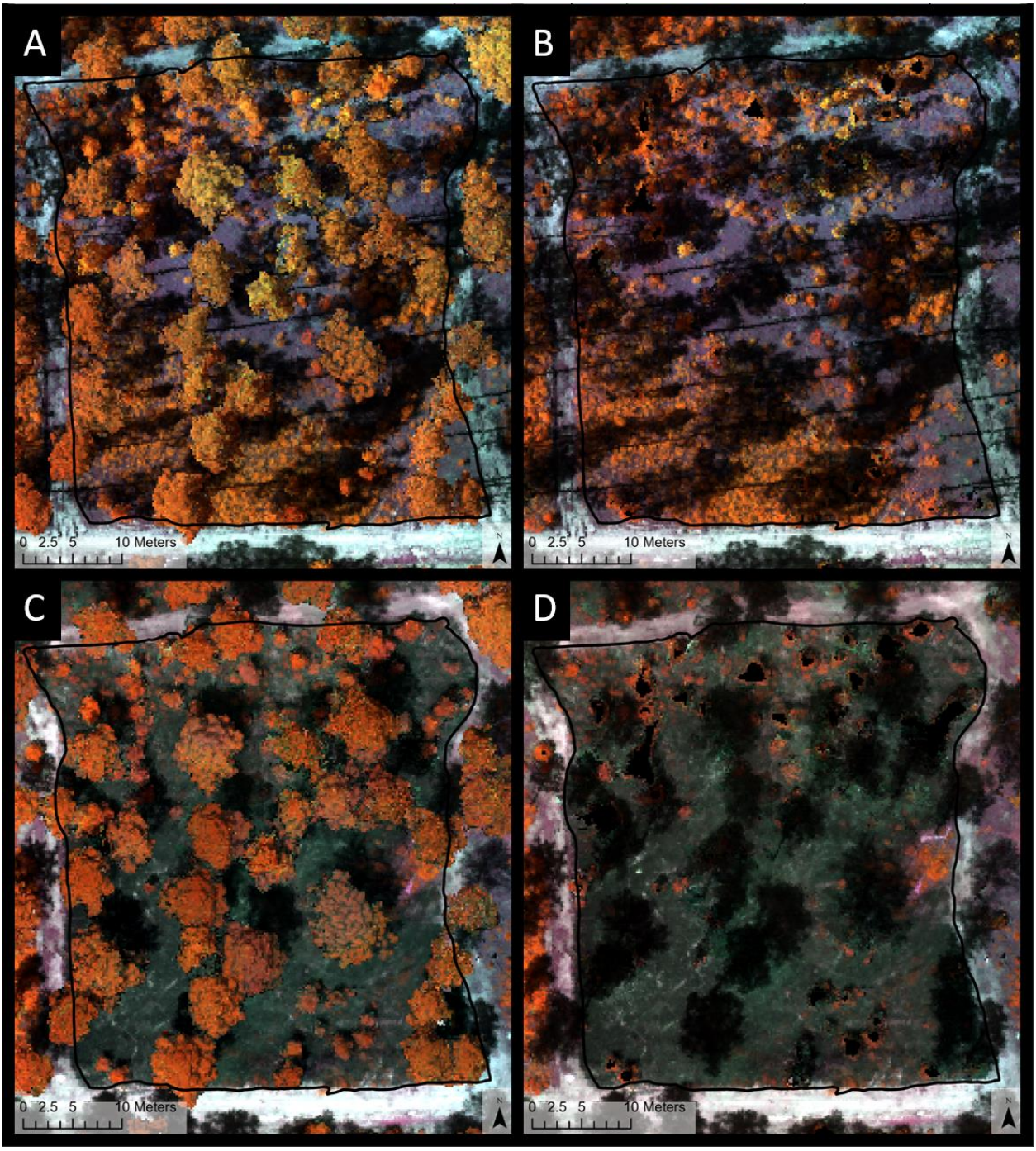

Figure 3.5. *Plot 6 as an example of a 20 cm resolution color infrared orthoimage produced from a multispectral photogrammetric point cloud. A: Pre-burn top-down, B: Pre-burn understory only, C: Post-burn top-down, D: Post-burn understory only.*

3.3.3.1 Multispectral Orthoimage Analysis

Scatter plots of matched raster cell NDVI values pre- and post-fire were created to visualize the shift in NDVI values. There were three sets of scatter plots: NDVI values for the matched cells in the understory-only orthoimages (e.g., Figure 3.5A and 3.5C), NDVI values for matched cells in top-down orthoimages (e.g., Figure 3.5B and 3.5D), and NDVI values for canopy-only matched cells. Paired z-tests were performed to determine if there was a significant difference between the pre- and post-fire NDVI values of the matched pixels. The z-tests were conducted in addition to using Cohen's d to quantify effect size. Cohen's d was performed on paired pixel data to assess the effect size of the fire on NDVI values. The same effect size thresholds were used as with the dDAP point clouds comparisons (section 3.3.2.1). Density probability plots were created for all comparisons to illustrate the change in the distribution of NDVI values when comparing understory-only, top-down, and tree-only imagery.

3.3.4 *RGB Orthoimage Processing*

Using CloudCompare, 5 cm resolution image rasters were produced from the RGB point clouds using only the points 2m and below (Figure 3.6). Images of the RGB orthoimages for all plots are included in the Supplementary Material (Chapter 6.2). The RGB values of each pixel were determined using the values of the point highest in elevation within each raster cell area. Owing to the complexity of the tree structures, 5 cm resolution images had too many gaps to effectively model the tree canopy extent. The 20 cm resolution rasters of all points greater than 2 m in height from the multispectral photogrammetric point clouds were used to determine the location and size of the canopy cover. The percentage of ground cover visible from a nadir view at each plot was calculated.

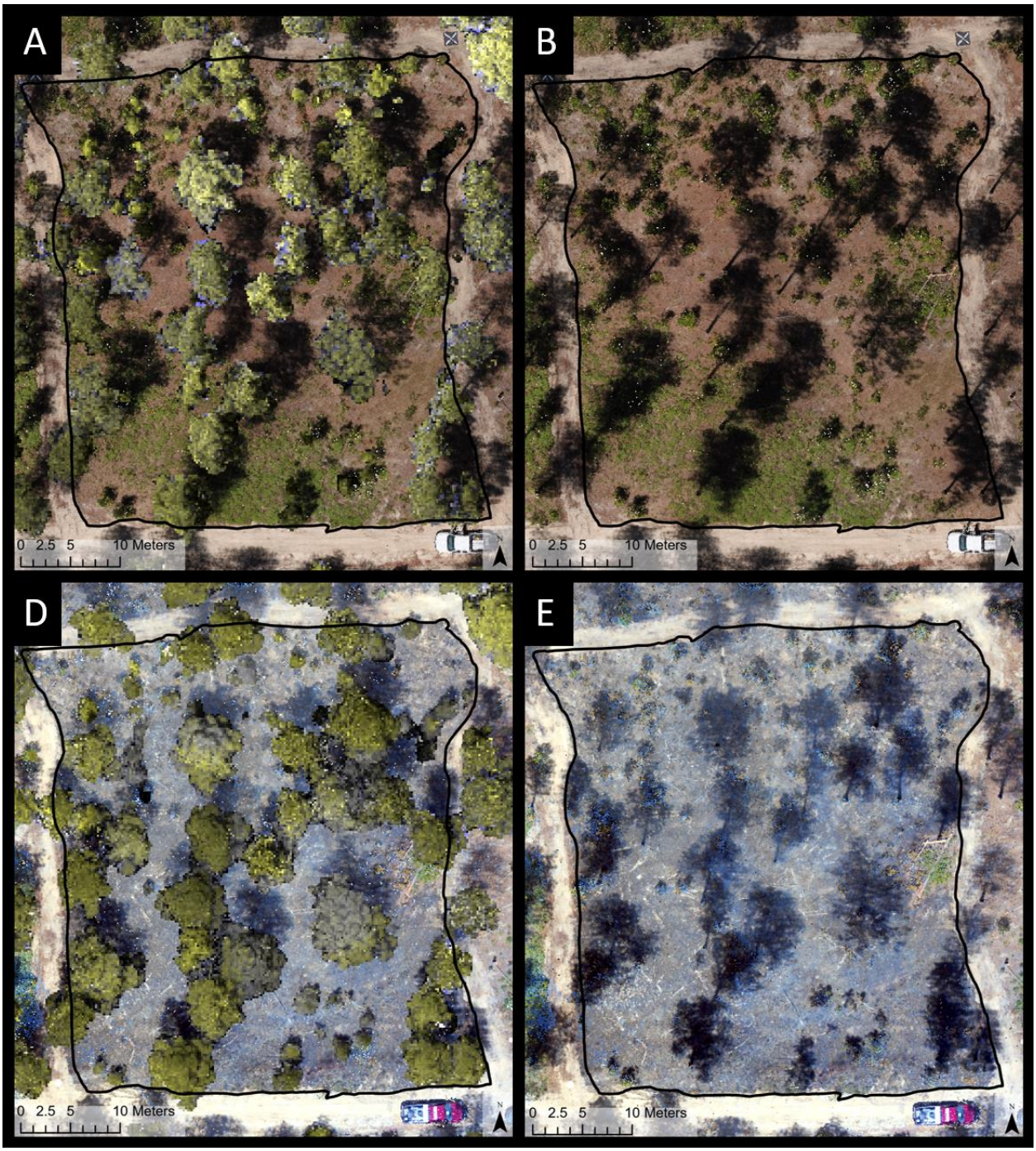

Figure 3.6. *Plot 6 as an example of a 5 cm resolution RGB orthoimage produced from a photogrammetric point cloud. A: pre-burn understory only, B: pre-burn top-down (20 cm resolution upper canopy model, C: post-burn understory only, D: post-burn top-down (20 cm resolution upper canopy model). The figures for all plots are provided in the Supplementary Material.*

In addition to the three RGB values of the image, a fourth band was added to the understory orthoimages. This fourth band was the height values from a digital surface model created from the 0 m – 2 m RGB photogrammetric point clouds (Figure 3.7). This additional band of height values aided in differentiating between herbaceous ground cover vegetation and shrubs greater than 0.5 m in height.

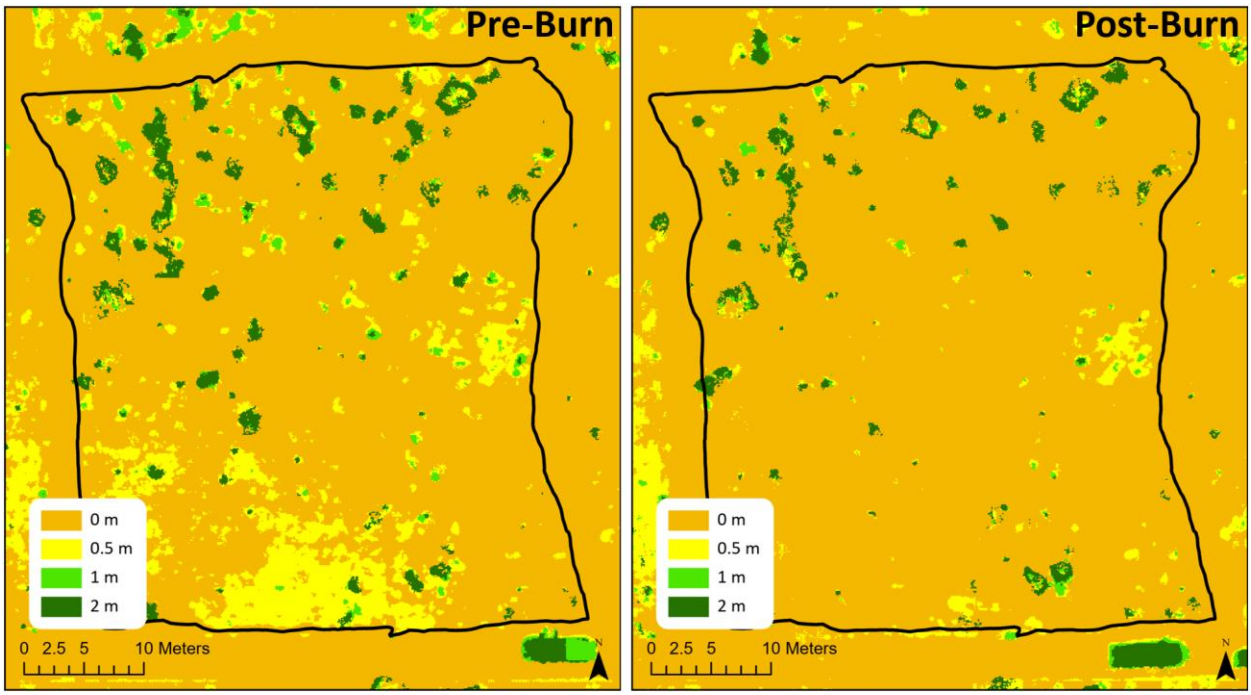

Figure 3.7. *Pre-Burn and Post-burn Digital Surface Models from Plot 6 showing changes in vegetation height. This allowed for a class of vegetation to be partitioned into two categories of 'tall vegetation' and 'low vegetation.'*

3.3.4.1 RGB Orthoimage analysis

RGB understory orthoimages and digital surface models were used to create pre-burn ground-cover classification maps with the following classes: bare ground, leaf litter, herbaceous vegetation (0-0.5m), shrub vegetation (taller than 0.5 m), and woody debris. Post-burn classification maps were also produced with the same classes and additional classes of black char (areas of incomplete combustion) and white ash (areas of complete combustion). Object-based supervised classification (support vector machine) was used to classify each image.

Accuracy assessment was performed using a 'ground truth' point density of 500 points per hectare. Points were placed in the classified images using a stratified random placement strategy.

The ground truth was established by visual examination of the images. A confusion matrix was produced to assess the accuracy rates of each class per plot as well as all plots combined.

3.3.5 *Multispectral dDAP dNDVI Comparison to Satellite dNDVI*

With understory, overstory, and top-down dNDVI rasters produced using multispectral dDAP data, comparison with satellite-derived dNDVI values was possible. The pre- and post-burn satellite imagery from both Sentinel 2 (10 m resolution) and Landsat 8 (30 m resolution) sensors was acquired, and the dNDVI values were calculated (Table 3.3). Satellite dNDVI values for the control and burned plots were compared with the dNDVI values for the burned and control plots from understory-only and top-down dDAP NDVI images. The effect size was measured using Cohen's d test.

Table 3.2. *Dates of the Sentinel and Landsat imagery used to derive NDVI values. The image dates used were based on data availability and lack of cloud cover.*

Pre-Burn Sentinel Date	Post-Burn Sentinel Date	Pre-Burn Landsat Date	Post-Burn Landsat Date
29/4/2018	9/5/2018	14/4/2018	12/5/2018

3.4 Results

3.4.1 *dDAP Point Clouds*

Violin plots of the distribution of NDVI values are presented in Figure 3.8 for aggregated burned and control plots. Height strata comparisons were performed for all 2 m strata up to 18 m. Vegetation in the plots was either sparse or non-existent above 18 m. The samples were individual points within the generated multispectral photogrammetric point clouds, so the sample sizes were very large. The aggregated burned plots had 7,088,516 points, with the majority concentrated at the ground level. The aggregated control plots had 2,136,420 points, with the majority concentrated at the ground level. Subsequently, all z-tests indicated a significant change in the mean NDVI value for all pre-/ post-fire comparisons at all height strata (p-value < 2.2e-16). Cohen's d values indicated either a small or very small effect size on the pre- and post-fire collected imagery in the control plots that were not burned, medium or small effect size in the burned plots above 10 m, and a very large effect size in burned plots blow 10 m (Figure 3.8).

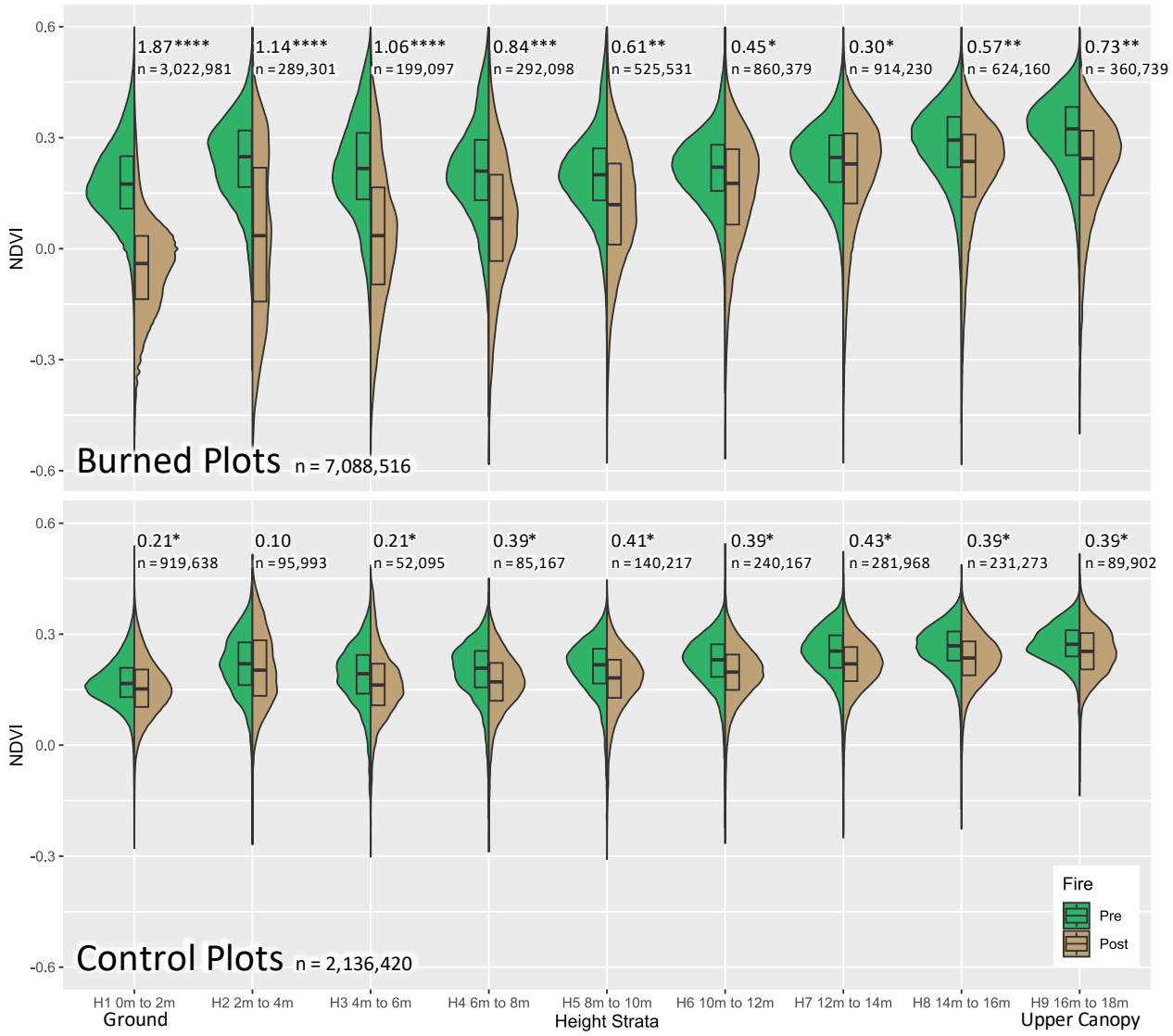

Figure 3.8. *Pre- and post-burn NDVI value violin plots for burned (top) and control units (bottom). The green side of the violins is the distribution of NDVI values pre-fire, with the brown side indicating the NDVI values post-fire. The numbers at the top of each violin are Cohen's d values, which quantify the effect size of the fire on NDVI values. Asterisks indicate: ****, very large effect; ***, large effect; **, medium effect; *, small effect; no asterisk, very small effect. Note that the control plots were not burned, but were labeled as pre- and post-fire to indicate the time the images were taken. The violins on the left represent the ground level, increasing in height to the right, up to 18 m. n indicates the number of points from the photogrammetric point clouds used to generate the plots, with most of the points being at the ground level. The median is indicated by the centerline in the box with one quantile above and below contained within the range of the rectangle.*

3.4.2 *Multispectral Orthoimage*

All z-tests comparing the burned plots to the control plots indicated a significant change in the mean NDVI value ($p < 2.2e\text{-}16$). All z-tests comparing pre-fire to post-fire plot NDVI values indicated a significant change in the mean (p-value < 2.2e-16). The samples were the individual pixels within the orthoimages for the probability density plots and the matched pre- and post-fire pixels for the scatter plots. The sample sizes were between 52,000 and 241,000 pixels (Figure 9).

The scatter and density plots for the aggregated burned and control plots are presented in Figure 3.9. Scatter plots were divided into four quadrants with a one-to-one line added. If the NDVI value before and after the burn were similar, the points should cluster around the one-to-one line. If points are in the upper left quadrant, then a positive NDVI value changed to a negative value. Upper right quadrant, a positive NDVI value stayed positive. Lower right quadrant, a negative NDVI value changed to a positive value. Lower left quadrant, a negative NDVI value stayed negative. Density plots indicate the probability that any randomly selected pixel will have the indicated NDVI value. Cohen's d values for the effect size indicated a small or medium effect for the pre and post imagery in the control plots as well as the top-down and tree only imagery in the burned plots. The understory-only orthoimages from the burned plots had a very high effect size between the pre- and post-fire imagery (Figure 3.9).

Unlike the RGB orthoimages, the understory multispectral orthoimages did not have complete coverage. In areas with larger continuous tree clumps (e.g., the east side of plot 24A (see supplemental material figure 6.S3.1)), some gaps in coverage occurred. There was an increase in the gaps when the continuous canopy coverage increased to over 100 m^2. Individual trees did not cause occlusion of the ground, but clumps of trees did. The percentage of each plot captured in the understory-only multispectral orthoimages, and the percentage of the area occluded by trees for each plot are presented in Table 3.3. There was variation in the area of the upper canopy as measured from pre- and post-fire imagery. The values given as canopy % are the average and range between the two.

Table 3.3. *Percentage of the ground that could be modeled using multispectral orthoimages for each plot, both pre-burn (Pre %) and post-burn (Post %). The percentage of the ground occluded from nadir by vegetation over 2 m (i.e., trees) is given as Canopy %.*

Plot	*Pre %*	*Post %*	*Canopy %*
1	86	81	67± 5
2	94	93	55± 2
3	90	92	55± 1
5	99	93	44 ± 5
6	98	91	43 ± 5
24A	87	70	70 ± 6
24B	95	86	47 ± 5

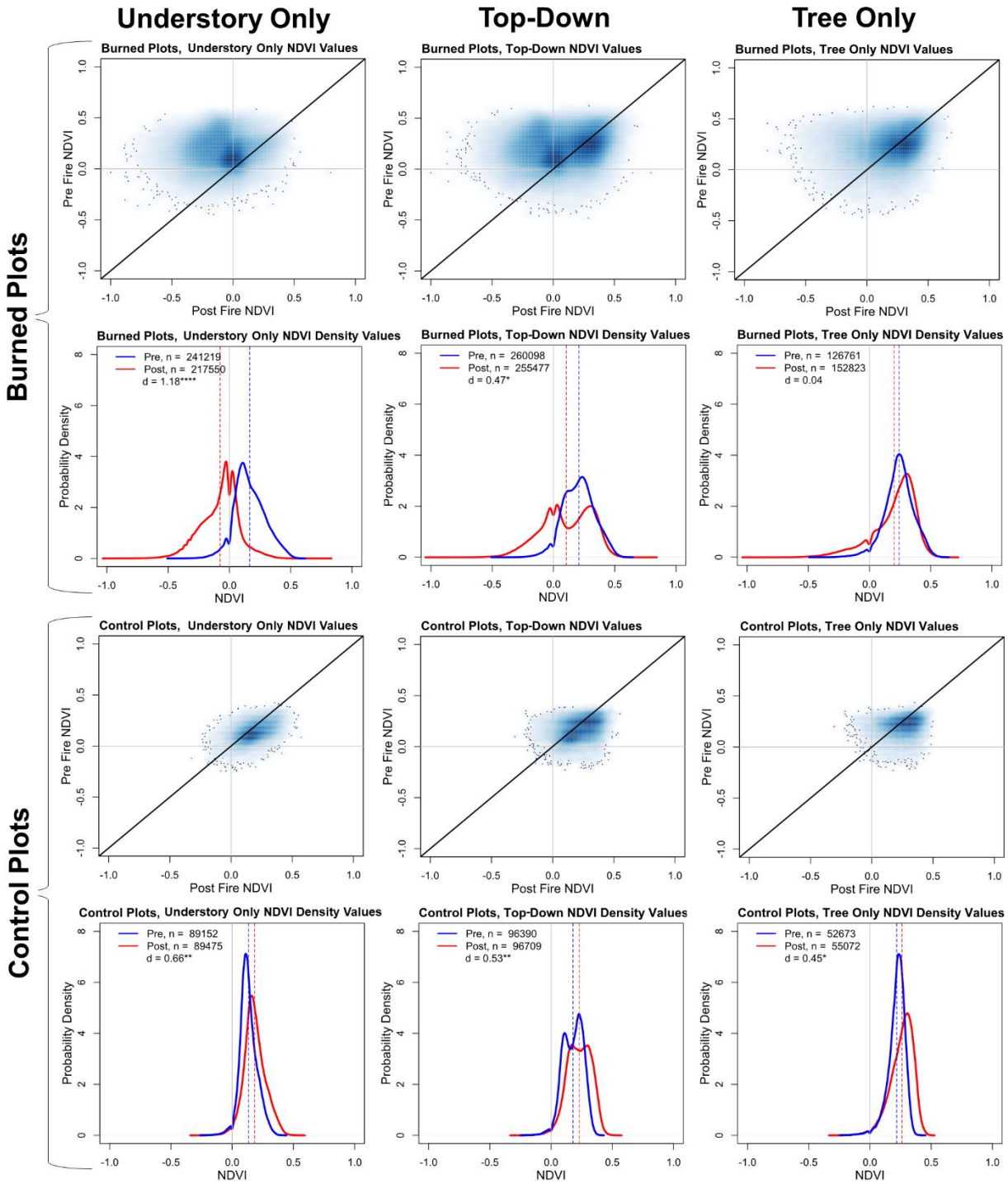

Figure 3.9. *Scatter and density plots comparing all burned plots (1, 5, 6, 24A, and 24B) pre- and post-fire with control plots (2 and 3). Scatter plots are matched pixels before and after the burn. The black one-to-one line indicates where points should cluster if no change has taken place. If points are spread into the upper-left quadrant of the scatter plot, there is a decrease in the NDVI values post-fire. The density plots indicate the probability that a random pixel will have the*

*indicated value. Dotted lines indicate mean values. The number of pixels used to generate the density plot is denoted as n. Cohen's d values quantifying the effect size of the fire on orthoimage NDVI values is given as d with asterisks indicating effect size. **** very large effect, *** large effect, ** medium effect, * small effect, no asterisk: very small effect.*

3.4.3 *RGB Orthoimage Classification*

Of the 1.44 hectare total area of all plots, 0.88 hectares had occluding vegetation above 2 m (61% ground occlusion). Ground cover was classified with an overall accuracy of 87% (Figure 3.10, Table 3.4, and Supplementary Material chapter 6.2). Tall vegetation was not included in the accuracy assessment, as it was determined by the DSM height layer, and vegetation height could not be corroborated by simple visual examination of the orthoimages. The ground vegetation included scorched vegetation for accuracy assessment.

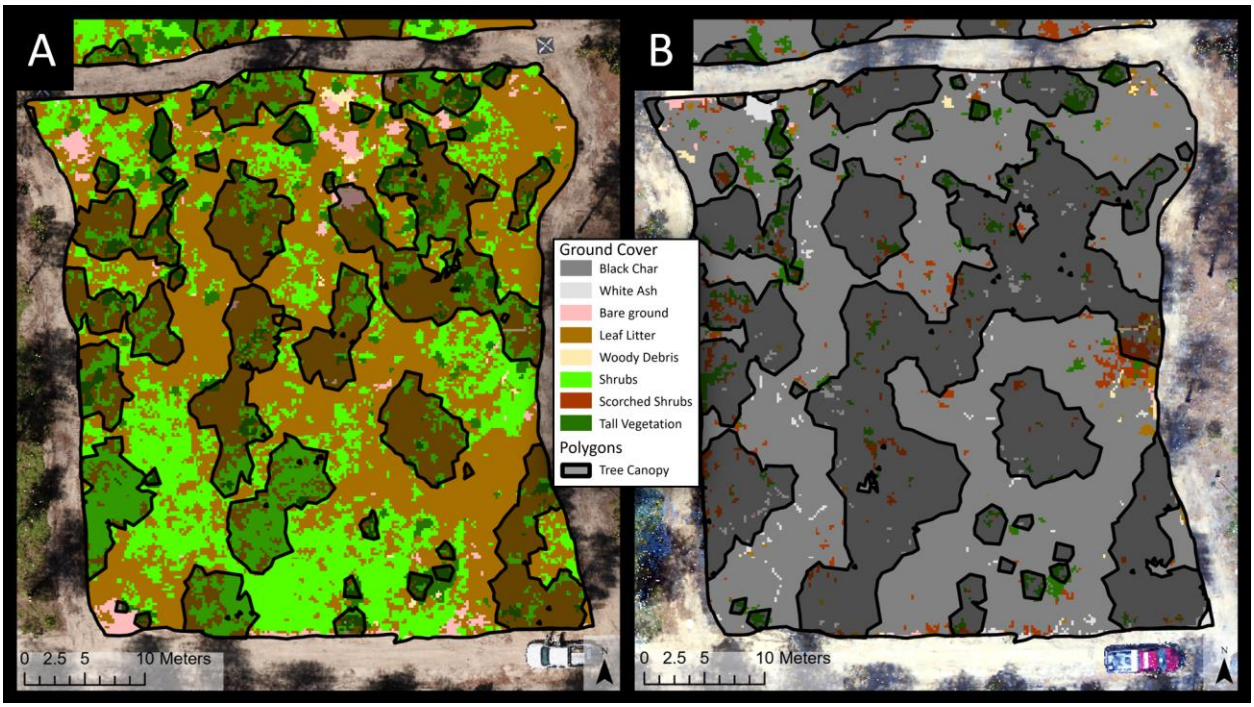

Figure 3.10. *Classification of Plot 6: pre-burn (A) and post-burn (B). The shaded polygons with black outlines indicate the locations of tree canopies or vegetation greater than 2 m in height. Classified images for all plots are provided in the Supplementary Material.*

Table 3.4. *Confusion matrix for all plots pre- and post-burn. The total accuracy was 87% (kappa =0.84).*

Class Value	*Black Char*	*White Ash*	*Bare Ground*	*Leaf Litter*	*Woody Debris*	*Ground Vegetation*	*Total*	*Users Accuracy*
Black Char	**166**	1	1	0	0	12	180	0.92
White Ash	2	**29**	8	0	0	1	40	0.73
Bare Ground	0	1	**99**	2	6	3	111	0.89
Leaf Litter	0	0	5	**192**	0	23	220	0.87
Woody Debris	0	1	19	3	**24**	1	48	0.5
Ground Vegetation	2	0	0	11	2	**194**	209	0.93
Total	170	32	132	208	32	234	**808**	
Producers Accuracy	0.98	0.91	0.75	0.92	0.75	0.83		**0.87**

3.4.4 *Multispectral dDAP dNDVI comparison to satellite dNDVI*

The number of samples from each image source reflects the resolution of the images. The dDAP imagery had a 20 cm resolution, Sentinel imagery had a 10 m resolution, and Landsat imagery had a 30 m resolution. The number of samples for each imagery source and the Cohen's d value for the effect size are presented in the boxplot in Figure 3.11. The difference in the n value for the dDAP understory compared to the dDAP top-down is due to some gaps present in the multispectral understory only orthoimages as discussed in section 3.4.2 (Table 3.3).

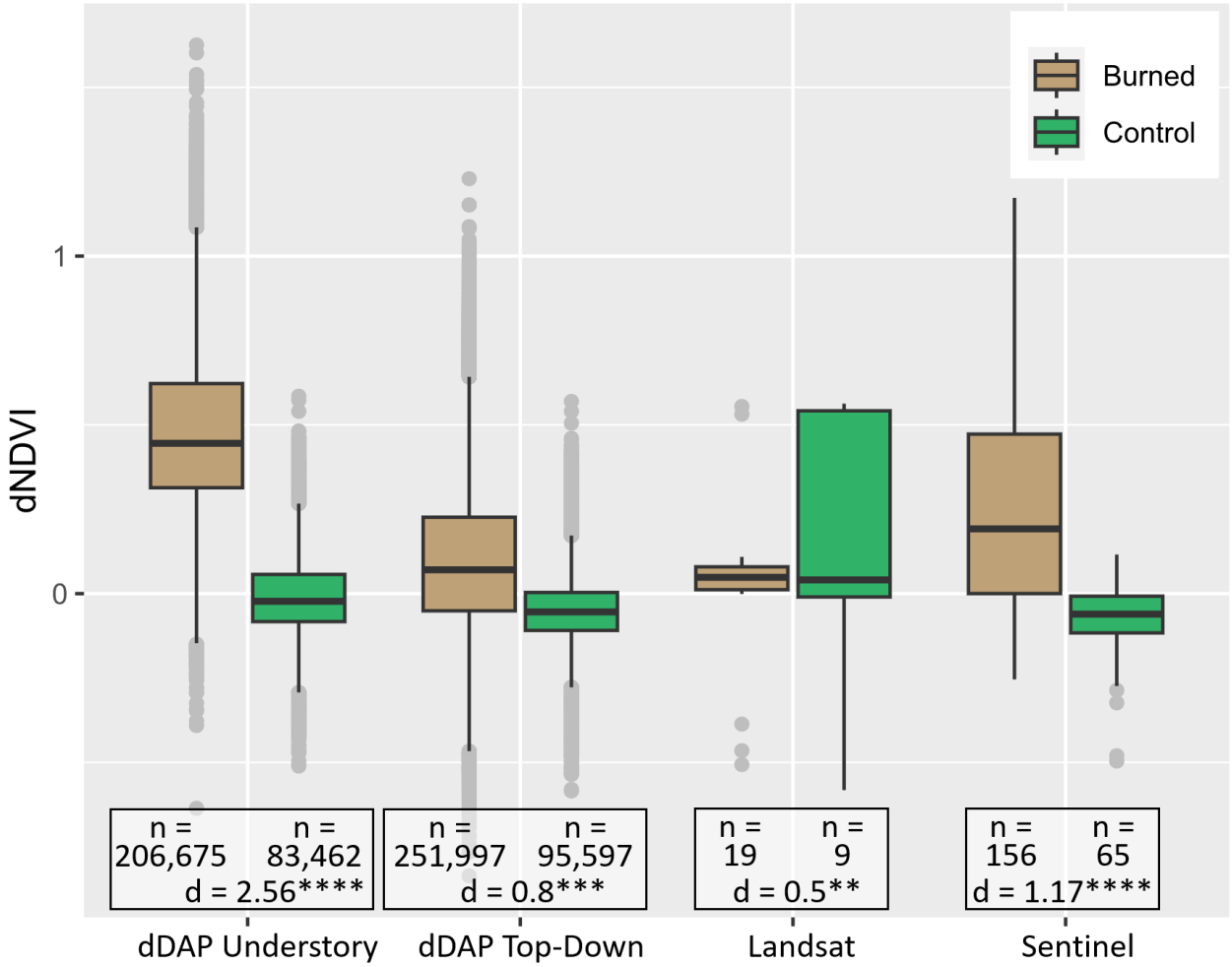

Figure 3.11. *Distribution of the dNDVI values for the four comparison groups. The fire had a medium and small effect on the measured dNDVI values of the dDAP top-down and Landsat imagery, respectively. There was a very large effect on the recorded dNDVI values of dDAP Understory and Sentinel imagery. Although both effects were categorized as very large, the effect size was more than double when quantifying dNDVI values using dDAP understory imagery.*

3.5 Discussion

3.5.1 *dDAP Point Clouds*

Our measured effect size was very large for strata lower than 6 m in our burned plots and was small in our control plots, indicating that our methodology quantifies the difference in fire effect size between burned and unburned plots. The effect size was larger in the 16–18 m strata

(0.73) in our burned plots than in the strata between 8 and 16 m. There are several potential reasons for this difference. The upper strata represented the bulk of the tree canopy, and there could have been crown scorching from lower flames. The strata between 8 m and 16 m were largely comprised of leafless tree trunks that were less likely to have a change in NDVI values. The values are for the aggregated point clouds of all sites, but points associated with individual trees could be segmented out, and potentially deriving a measurement of scorch per tree could be generated.

An area where improvement of the photogrammetric point clouds is needed is that they did not produce a full model of the trees. In the midstory, there were gaps where the upper story was not connected to the ground (Figure 3.4). The severity of the gaps was related to the amount of canopy cover within the plots (Table 3.3). The largest gaps in the midstory point clouds as well as the ground point clouds occurred in plots 1 and 24A where the canopy cover percent was the highest. That point generation was less successful in areas of higher canopy cover and subsequent higher levels of ground occlusion is understandable. Our photogrammetric point clouds also produced a larger area estimate for the upper canopy post-burn than for the pre-burn. It was assumed that if there was a change in the area between post- and pre-burn, there would be a reduction in the area post-burn due to the immolation of smaller trees and lower branches. This increase in canopy area estimates post-burn happened in every plot that was burned. The control plots (2 and 3) had very similar canopy area estimates between the two flights. This was reflected in the error estimations for the canopy cover percentage given in Table 3.3. The reason for the increase in the estimated canopy area in post-burn point clouds should be further examined. It is possible that the change in understory reflectance (from vegetated to charred) affected the image processing, and it would be informative to test whether the band combination of the imagery affects the derived point clouds.

3.5.2 *Multispectral Orthoimage*

The multispectral orthoimages were 20 cm resolution rasters generated from the multispectral point clouds. Conceptually, they represent a 20 × 20 cm column within the point cloud. We used the spectral values of points at the highest elevation within each column to generate top-down and tree-only rasters. This is analogous to taking a photograph from a drone. Similarly, for the understory orthoimages, after removing all points above 2 m, we used the spectral values for the points closest to 2 m to generate the orthoimages. Other options could have been spectral

values for the lowest elevation points, the mean, min, or max values for points, or any other statistical value derived from the points within the collum. Using the points closest to 2 m is the most analogous approach to taking a top-down photo with all vegetation above 2 m removed, but using the lowest elevation points may provide a more accurate representation of ground conditions. We opted for the 2 m point values to include ground vegetation and produce NDVI values that included vegetation in the pre-burn images and to account for the scorching or consumption of that vegetation in the post-burn images.

The probability density plots (Figure 3.9) used all pixels from the three sets of rasters (understory only, tree only, and top-down), whereas the scatter plots (Figure 3.9) used only matched pixels of the pre- and post-burn rasters. The sample sizes were subsequently larger for the density plots, as there were gaps in the output ortho images, preventing matched pre- and post-pixels for the sections of the understory-only images. Our pre- and post-burn sample sizes were too large for a simple comparison of the mean statistical tests that were sensitive to large sample numbers. However, a qualitative assessment of the pre- and post-scatter plots clearly shows that a large number of matched pixel NDVI values decreased in the understory-only images for the burned plots, whereas the control plot values remained relatively clustered around the 1 to 1 line. We can clearly see the effect of the burn lowering the understory NDVI value, while the upper canopy values showed less change by comparing the burned understory only scatter plot with the top-down and tree-only plots in Figure 3.9. There is a separation between the clusters of points in the burned top-down scatter plot that corresponds to the cluster of points in the understory only, and the tree-only burned scatter plots. This magnitude of separation was not observed in the scatter plot of the control plots.

The only plots that had a negative NDVI value among the six comparison sets in Figure 3.9 were the understory-only images of the burned plots. The effects of including the upper canopy in the top-down imagery brought the mean NDVI value from negative to positive and also reduced the effect size from being very large ($d = 1.18$) to small ($d = 0.47$). There was a medium effect size in the pre- and post-burn imagery collected in the control plots. With these plots having not been burned, a medium effect size was measured, indicating that the measured effect size can be caused by something other than a burn. Inconsistencies in the image acquisition locations during drone flights or image collection at different times of the day may contribute to changes in the NDVI values derived from multispectral drone imagery.

3.5.3 *RGB Orthoimage Classification*

We were able to classify the fine-scale understory land cover with a high level of accuracy (87%, Table 3.4). Some classes, such as woody debris and bare ground, had relatively low user accuracy (50%), largely owing to the spectral similarity between light-colored downed wood and sandy soil. Other classes, such as black char, had extremely high levels of accuracy (92% users and 98% producers) because of its unique appearance. In our classification, we included shadowed areas, as it was still possible to visually identify the classes for the accuracy assessment, even when they were in shadow. The determination of tall vegetation from ground vegetation was dependent on the accuracy of digital surface models derived from photogrammetric point clouds using points below 2 m. We believe that these DSMs likely underestimated the amount of tall vegetation due to dDAPs difficulties in modeling small branches and finer shrubs. Similar approaches combining photogrammetric DSMs with spectral information from drone imagery have similarly shown an increase in classification accuracy when only spectral information is used (Cunliffe et al., 2016; Prošek and Šímová, 2019).

We believe that our approach could aid in fine-scale mapping of vegetation cover changes in areas that would normally be occluded from overhead imagery. How vegetation recovers post-disturbance events (including, but not limited to, fire) at a fine scale has been the subject of much research (Robinson et al., 2022; Rydgren et al., 1998; Samiappan et al., 2019). While drones are increasingly used for this process, most of the applications so far have not utilized the ability to digitally remove the overstory for understory classification.

3.5.4 *Multispectral dDAP dNDVI Comparison to Satellite dNDVI*

While limited in scale, our initial findings on how dDAP can quantify understory and overstory fire effects compared to the top-down abilities of satellite imagery reinforces previous research conclusions that satellite imagery burn indices do not always accurately capture fire effects compared to field observations (Miller et al., 2023; Parks et al., 2019; Saberi et al., 2022). With our plots being relatively small in relation to the pixel sizes of Landsat and Sentinel data, there would be considerable spectral mixing of unburned and burned forested areas. The nineteen 30 m Landsat pixels used to derive dNDVI values were sampling areas outside the burn perimeter, which likely contributed to the Landsat data only detecting a medium effect size, while the Sentinel

data at 10 m resolution had 156 pixels within our burn parameters (Figure 3.11). For such a small fire area, using coarse-resolution imagery will inevitably not produce a satisfactory estimation of fire effects, but our drone imagery can derive dNDVI values for the understory only and measure a fire effect size more than double that of the Sentinel data produced, illustrating the tendency of satellite burn indices to underestimate the burn severity of ground fires.

3.5.5 *Future Research*

This research could be foundational for future studies on the use of multispectral photogrammetric point clouds for fire effect quantification. One limitation of this study that should be addressed in future research is how camera resolution, flight patterns, and processing affect point cloud generation. These topics for generalized dDAP acquisition have been addressed in numerous previous studies (Iglhaut et al., 2019; Kameyama and Sugiura, 2021; Koci et al., 2017; Westoby et al., 2012), but only in broader terms of the performance of structure-from-motion to produce reliable vegetation models. This study uses a novel approach of orthoimage generation that would be more robust if a more complete 3D model of tree stems could be produced. The ability to produce more complete multispectral photogrammetric point clouds from drone imagery is likely to increase as both drone and camera technologies advance. With increased modeling performance and longer drone flights, repeating this research across larger areas post-fire could also aid in the fine-scale mapping of revegetation or the tracking of the post-fire upper canopy die off. Having a quantified value for the area of understory vegetation consumed by fire can also improve models that use area consumed for estimations (e.g., smoke emission modeling). Furthermore, it could be informative to test how well the three-dimensional characterization of fire effects from drone imagery compared to field estimations, such as the CBI.

3.6 Conclusion

Drones have become indispensable tools in ecological monitoring. The utility and application of drones will continue to expand as the technology develops. In this study we explored the possibility of generating full three-dimensional models of forests with multispectral imagery. Our methodology requires a relatively open overstory to allow for the capture of the ground and understory vegetation but the ability to isolate understory vs overstory fire effects with spatial precession of a few centimeters will allow for fine scale quantification and monitoring of change

post disturbance. Furthermore, this process of isolating understory-only dNDVI orthoimages with the removal of live upper canopy foliage will aid in a much more robust and fine-scale assessment of fire severity than is possible using top-down imagery, such as that produced by satellites.

3.7 References

Agee, J.K., 1996. The influence of forest structure on fire behavior, in: Proceedings of the 17th Annual Forest Vegetation Management Conference. pp. 16–18.

Agisoft, 2014. Metashape 2020 [WWW Document]. URL https://www.agisoft.com/ (accessed 10.5.23).

Banach, C.A., Bradley, A.M., Tonkyn, R.G., Williams, O.N., Chong, J., Weise, D.R., Myers, T.L., Johnson, T.J., 2021. Dynamic infrared gas analysis from longleaf pine fuel beds burned in a wind tunnel: observation of phenol in pyrolysis and combustion phases. Atmospheric Meas. Tech. 14, 2359–2376.

Batchelor, J.L., Hudak, A.T., Gould, P., Moskal, L.M., 2023. Terrestrial and Airborne Lidar to Quantify Shrub Cover for Canada Lynx (Lynx canadensis) Habitat Using Machine Learning. Remote Sens. 15, 4434. https://doi.org/10.3390/rs15184434

Beaty, R.M., Taylor, A.H., 2001. Spatial and temporal variation of fire regimes in a mixed conifer forest landscape, Southern Cascades, California, USA. J. Biogeogr. 28, 955–966. https://doi.org/10.1046/j.1365-2699.2001.00591.x

Ben-Shachar, M., Lüdecke, D., Makowski, D., 2020. effectsize: Estimation of Effect Size Indices and Standardized Parameters. J. Open Source Softw. 5, 2815. https://doi.org/10.21105/joss.02815

Bessie, W.C., Johnson, E.A., 1995. The Relative Importance of Fuels and Weather on Fire Behavior in Subalpine Forests. Ecology 76, 747–762. https://doi.org/10.2307/1939341

CloudCompare [Computer Software]; Version 2.11; 2019. Available online: http://www.cloudcompare.org (accessed on 1 March 2021)., 2019. . (GPL software).

Cohen, J., 2013. Statistical power analysis for the behavioral sciences. Academic press.

Colomina, I., Molina, P., 2014. Unmanned aerial systems for photogrammetry and remote sensing: A review. ISPRS J. Photogramm. Remote Sens. 92, 79–97. https://doi.org/10.1016/j.isprsjprs.2014.02.013

Cunliffe, A.M., Brazier, R.E., Anderson, K., 2016. Ultra-fine grain landscape-scale quantification of dryland vegetation structure with drone-acquired structure-from-motion photogrammetry. Remote Sens. Environ. 183, 129–143. https://doi.org/10.1016/j.rse.2016.05.019

DJI, 2016. Mavic Pro 2016 [WWW Document]. URL https://www.dji.com/mavic (accessed 10.5.23).

Escuin, S., Navarro, R., Fernández, P., 2008. Fire severity assessment by using NBR (Normalized Burn Ratio) and NDVI (Normalized Difference Vegetation Index) derived from LANDSAT TM/ETM images. Int. J. Remote Sens. 29, 1053–1073. https://doi.org/10.1080/01431160701281072

Fawcett, D., Panigada, C., Tagliabue, G., Boschetti, M., Celesti, M., Evdokimov, A., Biriukova, K., Colombo, R., Miglietta, F., Rascher, U., 2020. Multi-scale evaluation of drone-based multispectral surface reflectance and vegetation indices in operational conditions. Remote Sens. 12, 514.

Filippelli, S.K., Lefsky, M.A., Rocca, M.E., 2019. Comparison and integration of lidar and photogrammetric point clouds for mapping pre-fire forest structure. Remote Sens. Environ. 224, 154–166. https://doi.org/10.1016/j.rse.2019.01.029

Franklin, S.E., Hall, R.J., Moskal, L.M., Maudie, A.J., Lavigne, M.B., 2000. Incorporating texture into classification of forest species composition from airborne multispectral images. Int. J. Remote Sens. 21, 61–79. https://doi.org/10.1080/014311600210993

French, N.H., Kasischke, E.S., Hall, R.J., Murphy, K.A., Verbyla, D.L., Hoy, E.E., Allen, J.L., 2008. Using Landsat data to assess fire and burn severity in the North American boreal forest region: an overview and summary of results. Int. J. Wildland Fire 17, 443–462.

Hansen, M.C., DeFries, R.S., Townshend, J.R., Sohlberg, R., 2000. Global land cover classification at 1 km spatial resolution using a classification tree approach. Int. J. Remote Sens. 21, 1331–1364.

Hardin, P.J., Hardin, T.J., 2010. Small-scale remotely piloted vehicles in environmental research. Geogr. Compass 4, 1297–1311.

Hauglin, M., Lien, V., Næsset, E., Gobakken, T., 2014. Geo-referencing forest field plots by co-registration of terrestrial and airborne laser scanning data. Int. J. Remote Sens. 35, 3135–3149. https://doi.org/10.1080/01431161.2014.903440
Herzog, M.M., Hudak, A.T., Weise, D.R., Bradley, A.M., Tonkyn, R.G., Banach, C.A., Myers, T.L., Bright, B.C., Batchelor, J.L., Kato, A., 2022. Point cloud based mapping of understory shrub fuel distribution, estimation of fuel consumption and relationship to pyrolysis gas emissions on experimental prescribed burns. Fire 5, 118.
Hoe, M.S., Dunn, C.J., Temesgen, H., 2018. Multitemporal LiDAR improves estimates of fire severity in forested landscapes. Int. J. Wildland Fire 27, 581–594.
Homer, C.H., Fry, J.A., Barnes, C.A., 2012. The national land cover database. US Geol. Surv. Fact Sheet 3020, 1–4.
Huang, S., Tang, L., Hupy, J.P., Wang, Y., Shao, G., 2021. A commentary review on the use of normalized difference vegetation index (NDVI) in the era of popular remote sensing. J. For. Res. 32, 1–6. https://doi.org/10.1007/s11676-020-01155-1
Hudak, A.T., Kato, A., Bright, B.C., Loudermilk, E.L., Hawley, C., Restaino, J.C., Ottmar, R.D., Prata, G.A., Cabo, C., Prichard, S.J., 2020. Towards spatially explicit quantification of pre-and post-fire fuels and fuel consumption from traditional and point cloud measurements. For. Sci. 66, 428–442.
Hudak, A.T., Ottmar, R.D., Vihnanek, R.E., Brewer, N.W., Smith, A.M.S., Morgan, P., Hudak, A.T., Ottmar, R.D., Vihnanek, R.E., Brewer, N.W., Smith, A.M.S., Morgan, P., 2013. The relationship of post-fire white ash cover to surface fuel consumption. Int. J. Wildland Fire 22, 780–785. https://doi.org/10.1071/WF12150
Iglhaut, J., Cabo, C., Puliti, S., Piermattei, L., O'Connor, J., Rosette, J., 2019. Structure from Motion Photogrammetry in Forestry: a Review. Curr. For. Rep. 5, 155–168. https://doi.org/10.1007/s40725-019-00094-3
Kameyama, S., Sugiura, K., 2021. Effects of differences in structure from motion software on image processing of unmanned aerial vehicle photography and estimation of crown area and tree height in forests. Remote Sens. 13, 626.
Kane, V.R., Lutz, J.A., Roberts, S.L., Smith, D.F., McGaughey, R.J., Povak, N.A., Brooks, M.L., 2013. Landscape-scale effects of fire severity on mixed-conifer and red fir forest structure in Yosemite National Park. For. Ecol. Manag. 287, 17–31.
Kato, A., Moskal, L.M., Batchelor, J.L., Thau, D., Hudak, A.T., 2019. Relationships between Satellite-Based Spectral Burned Ratios and Terrestrial Laser Scanning. Forests 10, 444. https://doi.org/10.3390/f10050444
Keeley, J.E., 2009. Fire intensity, fire severity and burn severity: a brief review and suggested usage. Int. J. Wildland Fire 18, 116–126.
Key, C.H., Benson, N.C., 2006. Landscape Assessment (LA). Lutes Duncan C Keane Robert E Caratti John F Key Carl H Benson Nathan C Sutherl. Steve Gangi Larry J 2006 FIREMON Fire Eff. Monit. Inventory Syst. Gen Tech Rep RMRS-GTR-164-CD Fort Collins CO US Dep. Agric. For. Serv. Rocky Mt. Res. Stn. P -1-55 164.
Koci, J., Jarihani, B., Leon, J.X., Sidle, R.C., Wilkinson, S.N., Bartley, R., 2017. Assessment of UAV and ground-based structure from motion with multi-view stereo photogrammetry in a gullied savanna catchment. ISPRS Int. J. Geo-Inf. 6, 328.
Kolarik, N.E., Ellis, G., Gaughan, A.E., Stevens, F.R., 2019. Describing seasonal differences in tree crown delineation using multispectral UAS data and structure from motion. Remote Sens. Lett. 10, 864–873. https://doi.org/10.1080/2150704X.2019.1629708
Kolden, C.A., Smith, A.M., Abatzoglou, J.T., 2015. Limitations and utilisation of Monitoring Trends in Burn Severity products for assessing wildfire severity in the USA. Int. J. Wildland Fire 24, 1023–1028.
Larrinaga, A., Brotons, L., 2019. Greenness Indices from a Low-Cost UAV Imagery as Tools for Monitoring Post-fire Forest Recovery. Drones 3, 6.
Li, L., Chen, J., Mu, X., Li, W., Yan, G., Xie, D., Zhang, W., 2020. Quantifying Understory and Overstory Vegetation Cover Using UAV-Based RGB Imagery in Forest Plantation. Remote Sens. 12, 298. https://doi.org/10.3390/rs12020298
Lydersen, J.M., Collins, B.M., Miller, J.D., Fry, D.L., Stephens, S.L., 2016. Relating Fire-Caused Change in Forest Structure to Remotely Sensed Estimates of Fire Severity. Fire Ecol. 12, 99–116. https://doi.org/10.4996/fireecology.1203099

McCarley, T.R., Kolden, C.A., Vaillant, N.M., Hudak, A.T., Smith, A.M.S., Wing, B.M., Kellogg, B.S., Kreitler, J., 2017. Multi-temporal LiDAR and Landsat quantification of fire-induced changes to forest structure. Remote Sens. Environ. 191, 419–432. https://doi.org/10.1016/j.rse.2016.12.022
Miller, C.W., Harvey, B.J., Kane, V.R., Moskal, L.M., Alvarado, E., Miller, C.W., Harvey, B.J., Kane, V.R., Moskal, L.M., Alvarado, E., 2023. Different approaches make comparing studies of burn severity challenging: a review of methods used to link remotely sensed data with the Composite Burn Index. Int. J. Wildland Fire 32, 449–475. https://doi.org/10.1071/WF22050
Miller, J.D., Knapp, E.E., Key, C.H., Skinner, C.N., Isbell, C.J., Creasy, R.M., Sherlock, J.W., 2009. Calibration and validation of the relative differenced Normalized Burn Ratio (RdNBR) to three measures of fire severity in the Sierra Nevada and Klamath Mountains, California, USA. Remote Sens. Environ. 113, 645–656. https://doi.org/10.1016/j.rse.2008.11.009
Parks, S.A., Holsinger, L.M., Koontz, M.J., Collins, L., Whitman, E., Parisien, M.-A., Loehman, R.A., Barnes, J.L., Bourdon, J.-F., Boucher, J., Boucher, Y., Caprio, A.C., Collingwood, A., Hall, R.J., Park, J., Saperstein, L.B., Smetanka, C., Smith, R.J., Soverel, N., 2019. Giving Ecological Meaning to Satellite-Derived Fire Severity Metrics across North American Forests. Remote Sens. 11, 1735. https://doi.org/10.3390/rs11141735
Parrot, n.d. Sequoia 2016 [WWW Document]. URL https://www.parrot.com/en/support/documentation/sequoia (accessed 10.5.23).
Perry, D.A., Hessburg, P.F., Skinner, C.N., Spies, T.A., Stephens, S.L., Taylor, A.H., Franklin, J.F., McComb, B., Riegel, G., 2011. The ecology of mixed severity fire regimes in Washington, Oregon, and Northern California. For. Ecol. Manag. 262, 703–717.
Pettorelli, N., Vik, J.O., Mysterud, A., Gaillard, J.-M., Tucker, C.J., Stenseth, N.Chr., 2005. Using the satellite-derived NDVI to assess ecological responses to environmental change. Trends Ecol. Evol. 20, 503–510. https://doi.org/10.1016/j.tree.2005.05.011
Prošek, J., Šímová, P., 2019. UAV for mapping shrubland vegetation: Does fusion of spectral and vertical information derived from a single sensor increase the classification accuracy? Int. J. Appl. Earth Obs. Geoinformation 75, 151–162.
Puliti, S., Talbot, B., Astrup, R., 2018. Tree-stump detection, segmentation, classification, and measurement using unmanned aerial vehicle (UAV) imagery. Forests 9, 102.
Robinson, J.M., Harrison, P.A., Mavoa, S., Breed, M.F., 2022. Existing and emerging uses of drones in restoration ecology. Methods Ecol. Evol. 13, 1899–1911. https://doi.org/10.1111/2041-210X.13912
Rothermel, R.C., 1991. Predicting behavior and size of crown fires in the Northern Rocky Mountains. US Department of Agriculture, Forest Service, Intermountain Research Station.
Running, S.W., Loveland, T.R., Pierce, L.L., Nemani, R.R., Hunt, E.R., 1995. A remote sensing based vegetation classification logic for global land cover analysis. Remote Sens. Environ., Remote Sensing of Land Surface for Studies of Global Chage 51, 39–48. https://doi.org/10.1016/0034-4257(94)00063-S
Rydgren, K., Hestmark, G., Økland, R.H., 1998. Revegetation following experimental disturbance in a boreal old-growth *Picea abies* forest. J. Veg. Sci. 9, 763–776. https://doi.org/10.2307/3237042
Saberi, S.J., Agne, M.C., Harvey, B.J., 2022. Do you CBI what I see? The relationship between the Composite Burn Index and quantitative field measures of burn severity varies across gradients of forest structure. Int. J. Wildland Fire 31, 112–123.
Samiappan, S., Hathcock, L., Turnage, G., McCraine, C., Pitchford, J., Moorhead, R., 2019. Remote sensing of wildfire using a small unmanned aerial system: Post-fire mapping, vegetation recovery and damage analysis in Grand Bay, Mississippi/Alabama, USA. Drones 3, 43.
Scharko, N.K., Oeck, A.M., Myers, T.L., Tonkyn, R.G., Banach, C.A., Baker, S.P., Lincoln, E.N., Chong, J., Corcoran, B.M., Burke, G.M., 2019. Gas-phase pyrolysis products emitted by prescribed fires in pine forests with a shrub understory in the southeastern United States. Atmospheric Chem. Phys. 19, 9681–9698.
Sun, Z., Wang, X., Wang, Z., Yang, L., Xie, Y., Huang, Y., 2021. UAVs as remote sensing platforms in plant ecology: review of applications and challenges. J. Plant Ecol. 14, 1003–1023.
Szpakowski, D.M., Jensen, J.L., 2019. A review of the applications of remote sensing in fire ecology. Remote Sens. 11, 2638.

Viana-Soto, A., García, M., Aguado, I., Salas, J., 2022. Assessing post-fire forest structure recovery by combining LiDAR data and Landsat time series in Mediterranean pine forests. Int. J. Appl. Earth Obs. Geoinformation 108, 102754.
Wagner, C.E.V., 1977. Conditions for the start and spread of crown fire. Can. J. For. Res. 7, 23–34. https://doi.org/10.1139/x77-004
Wallace, L., Lucieer, A., Malenovský, Z., Turner, D., Vopěnka, P., 2016. Assessment of Forest Structure Using Two UAV Techniques: A Comparison of Airborne Laser Scanning and Structure from Motion (SfM) Point Clouds. Forests 7, 62. https://doi.org/10.3390/f7030062
Weise, D.R., Hao, W.M., Baker, S., Princevac, M., Aminfar, A.-H., Palarea-Albaladejo, J., Ottmar, R.D., Hudak, A.T., Restaino, J., O'Brien, J.J., 2022. Comparison of fire-produced gases from wind tunnel and small field experimental burns. Int. J. Wildland Fire 31, 409–434.
Westoby, M.J., Brasington, J., Glasser, N.F., Hambrey, M.J., Reynolds, J.M., 2012. 'Structure-from-Motion' photogrammetry: A low-cost, effective tool for geoscience applications. Geomorphology 179, 300–314. https://doi.org/10.1016/j.geomorph.2012.08.021
Wright, C.S., Agee, J.K., 2004. Fire and Vegetation History in the Eastern Cascade Mountains, Washington. Ecol. Appl. 14, 443–459. https://doi.org/10.1890/02-5349

Chapter 4. Terrestrial and Airborne Lidar to Quantify Shrub Cover for Canada Lynx (Lynx Canadensis) Habitat Using Machine Learning.

Batchelor, J.L.; Hudak, A.T.; Gould, P.; Moskal, L.M. Terrestrial and Airborne Lidar to Quantify Shrub Cover for Canada Lynx (Lynx Canadensis) Habitat Using Machine Learning. *Remote Sensing* **2023**, *15*, 4434, doi:10.3390/rs15184434.

4.1 Abstract

Canada lynx is listed as a threatened species, and as such, the identification and conservation of lynx habitat is of significant concern. Lynx require areas with high amounts of horizontal cover made up of ground vegetation. Lidar offers a robust method of quantifying vegetation structure and airborne lidar has been acquired across large areas of potential lynx habitat. Unfortunately, airborne lidar is often not able to directly measure understory horizontal cover due to occlusion from the upper branches. Terrestrial lidar does directly measure understory horizontal cover and can be used as training data for larger area models using airborne lidar. In this study, we acquired 168 individual terrestrial lidar scans (TLS) across 42 sites in north central Washington state. We generated metrics from the single scan TLS plots using depth maps, a digital coverboard, and voxels. Using our TLS metrics as training data for airborne lidar acquired for the entire Loomis State Forest, we were able to produce a model using xgboost with 85% accuracy. We believe our study shows that single scan TLS plots can be used effectively to quantify fine scale forest structure elements relevant to species habitat, to then inform larger area models using airborne lidar.

4.2 Introduction

4.2.1 *Canada Lynx*

The Canada lynx (*Lynx canadensis*) is listed as a threatened species in the conterminous United States (US Fish Wildlife Service, 2017). As such, the identification and conservation of lynx habitat is of significant concern. Canada lynx are considered to be specialist predators relying on

snowshoe hares (*Lepus americanus*) as their main prey source. The Canada lynx, snowshoe hare relationship is well documented (Elton and Nicholson, 1942; Koehler, 1990) with lynx location and hunting dictated by snowshoe hair abundance. The preferred lynx habitat is habitat that supports high numbers of snowshoe hares.

Lynx tend to avoid open and lightly forested areas, preferring areas with high amounts of both vertical and horizontal cover (Koehler et al., 1979; Murray et al., 1994; Parker et al., 1983; Poole, 2003, 1994). While lynx occupy a wide variety of forest types, they prefer mid-successional forests with moderate to high stem densities (Fuller and Harrison, 2010; Ivan and Shenk, 2016). Canada lynx habitat requires high levels of cover with that cover extending above 1.5 m to ensure sufficient vegetation and forage availability for snowshoe hares in winter months when snow covers lower vegetation (Ivan and Shenk, 2016; Maletzke et al., 2008). Many habitat sampling techniques to identify appropriate Canada lynx habitat rely on the metrics of visual occlusion and forage availability above typical snow depths.

4.2.2 *Habitat Sampling Methods*

The Washington State Department of Natural Resources (WA DNR) is mandated to manage habitat for Canada lynx under the 2006 Lynx Habitat Management Plan (Quade and Minkova, 2006), which was developed as a revision of its original 1996 Lynx Habitat Management Plan. An element of the plan is to maintain forage habitat on DNR-managed lands within lynx management zones. The lynx management zones in Washington state are primarily in the northeast of the state with the largest state-managed forest within the management zones being the Loomis State Forest. The DNR lynx management plan calls for measuring understory horizontal cover using a 2 m x 30 cm cover board at a distance of 15 m at a height of 1.5 m to 2 m from the ground. Stands are measured at 10 points on a transect and 4 cover estimates are made at each point. Stand with 4 or fewer open views out of the 40 observations are considered to have sufficient cover for forage habitat.

Similar sampling techniques are used throughout the range of Canada lynx habitat in the conterminous United States to identify areas for conservation. Aside from coverboards, other methods are also used for determining understory horizontal cover such as a staff-ball, cover pole, or profile tube. The resultant estimated cover can vary significantly depending on the method used (Collins and Becker, 2001). The determination if a coverboard as open or not is normally a subjective

assessment done in the field and is prone to observer bias. Cameras and post field work digital processing of imagery can remove some of that observer bias (Campbell et al., 2018; Jorgensen et al., 2013); however, the use of active remote sensing technologies such as lidar may provide a better alternative for arriving at an objective measurement of forest and ground vegetation structure.

4.2.3 *Lidar*

Airborne laser scanning (ALS) has become a standard tool for forest mensuration. It is well established in its use for quantifying forest structure (Beland et al., 2019; Coops et al., 2021). Spatial models predicting forest structure from lidar data are well established. Multiple linear regression (MLR) models providing estimates of basal area, tree heights, canopy closure, gap fractions, and leaf area index are all possible using airborne lidar (Bouvier et al., 2015; Hudak et al., 2012, 2009; Zhao et al., 2011; Zheng et al., 2017). Machine learning regression models have been shown to outperform MLR models for predicting forest metrics from lidar data such as biomass (García-Gutiérrez et al., 2015; Gleason and Im, 2012) and machine learning using categorical data have been employed for tree location and species identification, point classification, stand heights, and other forest structure parameters (Farhani et al., 2021; Lee et al., 2018; Marrs and Ni-Meister, 2019; Weiss et al., 2010). Common machine learning techniques for forest metrics from lidar data are random forest and support vector machine, which gradient boosting methods such as xgboost becoming more common (Chen and Guestrin, 2016; Teri and Musliman, 2019). Further, deep learning techniques are also becoming more common to be applied to lidar data to predict forest characteristics (Liu et al., 2020, 2021; Marinelli et al., 2022). Machine learning techniques can improve results beyond MLR analysis and allow for the modeling of ordinal data beyond what regression analysis is capable of.

While aerial lidar has successfully been used to identify important habitat characteristics such as height of dominate trees and mid-canopy forest structure (Blomdahl et al., 2019; Johnston and Moskal, 2017; North et al., 2017), the occlusion from overstory branches and leaves makes accurate prediction of understory metrics such as horizontal cover more difficult. Work has been done modeling understory conditions from aerial lidar, including using horizontal cover estimated in the field from coverboards to train landscape level airborne lidar models to predict horizontal cover specifically for lynx habitat (Fekety et al., 2019; Tymen et al., 2017; Venier et al., 2019; Wing et al., 2012). In this study, we seek to demonstrate that horizontal cover metrics derived from terrestrial lidar

scanning (TLS) can be used in place of field coverboard estimates of horizontal cover to train landscape level airborne lidar machine learning models.

TLS has been used in previous wildlife studies to characterize levels of concealment and predator sightlines (Olsoy et al., 2015). TLS is well suited to determine understory vegetation characteristics such as density of foliage and amount of open area (Ashcroft et al., 2014; Huang et al., 2009; Wallace et al., 2020). Depth of view and openness of a location can be quantified by looking at how far each pulse travels, and if a pulse is not returned at all (Batchelor et al., 2023; Richardson et al., 2014). TLS can replicate the use of a coverboard at fixed locations in a non-subjective manner, as well as return a robust estimate of total depth and openness of a plot. TLS offers many advantages over cover boards. It produces an accurate, high-resolution point cloud of forest vegetation that allows understory horizontal cover to be estimated over a large area. It can also produce consistent horizontal cover estimates by eliminating the subjectivity of ocular estimates with a cover board. TLS measurements are also likely to be considerably faster to complete compared to a large number of cover-board measurements at each sample point.

4.2.4 *Objectives*

The goal of this study is to produce a model and raster map of understory horizontal cover estimates across the entirety of the Loomis State Forest, as a proxy for Canada lynx habitat. The study has two main objectives:

- To generate a range of metrics that quantify understory horizontal cover from single point TLS scans, and to determine which of these horizontal cover metrics best differentiates low from high horizontal cover.
- To use TLS-derived understory horizontal cover metrics to train a model predicting horizontal cover from a host of ALS metrics at plot scale, that can then be applied to the rasterized ALS metrics to map horizontal cover across the landscape.

A large portion of this study is an exploration of what reasonable metrics can be derived from TLS for understory horizontal cover and, in turn, identify which metrics can be derived from ALS to produce a high performing model. The outcomes of this research will aid in creating robust

models of habitat conditions that can be used by land managers to identify areas of special conservation concern.

4.3 Methods

4.3.1 *Study Area*

This study was conducted primarily in the Loomis State Forest with additional study sites in the nearby Little Pend Oreille State Forest in north-central Washington State, USA (Figure 4.1). Both forests are managed by the WA DNR. The Loomis state forest occupies just over 54,000 hectares in northern Washington with the northernmost boundary abutting the Canadian border. There are several vegetation zones within the Loomis forest, with the two most common zones being dominated by Douglas-fir (*Pseudotsuga menziesii*) and subalpine fir (*Abies lasiocarpa*) tree species (Washington State Department of Natural Resources, n.d.). The other vegetation zones are shrub steppe, ponderosa pine (*Pines ponderosa*), lodgepole pine (*Pinus contorta*), and alpine. The western side of the Loomis tends to be higher in elevation and hence more heavily forested than the east side. Much of the forest within the Loomis is fragmented due to logging activity and past fires. Active cattle grazing also occurs on a large percentage of the forest.

4.3.2 *Site Selection*

The WA DNR uses the Remote Sensing Forest Inventory System (RS-FRIS) to characterize forest lands on state trust lands (Gould et al., n.d.). RS-FRIS includes a grid of 0.04 ha sample plots that are used both for statistical estimates and to train predictive models. Existing RS-FRIS plots were used as study sites for this study. Plots were broadly characterized by the WA DNR into 4 categories based on past measurements: low cover, young forest, normal, and mature forest. Sites from the existing pool of RS-FRIS plot locations were chosen for this study based on three criteria: 1) within 2 km of a road for ease of access, 2) no significant disturbances (such as fire or logging) at the site since the most recent ALS acquisition, and 3) good representation of the 4 RS-FRIS categories. In total, 40 sites were selected with 4 TLS scans acquired at each site for a total of 160 scan plots.

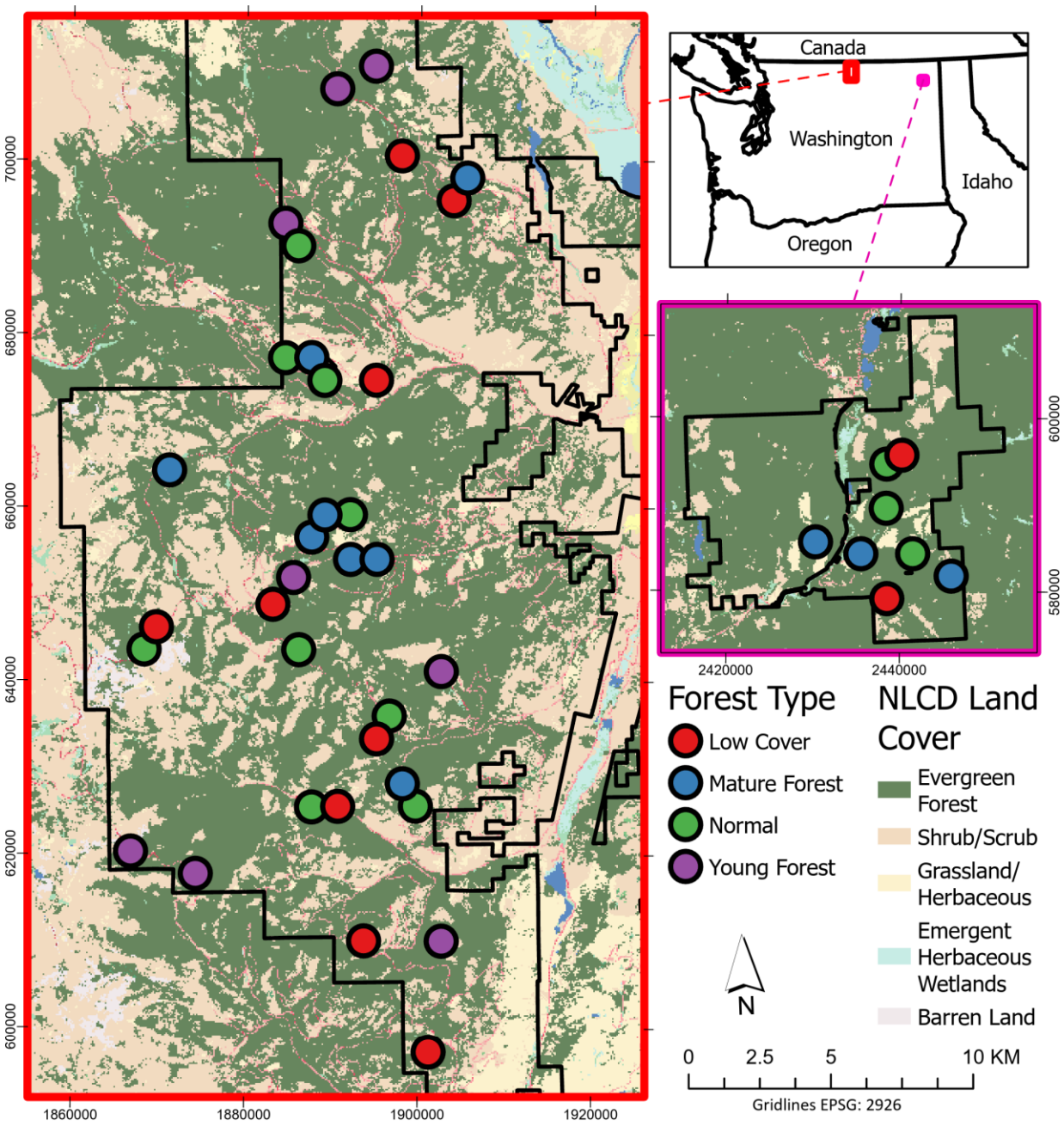

Figure 4.1 *Map of study sites within the Loomis State Forest (red frame) and the Little Pend Oreille State Forest (pink frame). 42 sites were sampled with each site consisting of 4 TLS scan plots (168 plots total). Land cover classification from the National Land Cover Database added to provide vegetation cover context.*

4.3.3 *TLS Acquisition*

A FARO s350 TLS unit was used for this study. The FARO uses 1550 nm laser light and a phase shift sampling process. Scan line resolution was set at 0.035° for both horizontal and vertical scanlines, and full 360° horizontal scans including color photos were taken at each scan location. Scan line density was 164 per meter at 10 m from scanner and 109 per meter at 15 m from scanner. Vertically, the FARO scans from 30° to 180°, with 180° being straight up (overhead) and 0° being straight down (nadir).

Scanning was done between October 2021 and September 2022. Scanning was only done in summer and early Fall. Each site had a center monumented for the RS-FRIS program. TLS scanning was done with a central scan (scan 1) placed 1 m north of the monumented site center unless that location was heavily occluded by vegetation in which case the location within 1 m of the site center with the best visibility was used. A TLS target sphere was placed at the site center with three other spheres placed at ~10 m distance from the center in the general directions of 60°, 180°, and 300° magnetic north. Scans 2, 3, and 4 had a generally similar distribution placed at ~10 m distance from the center in the general directions of 0°, 120°, and 240° magnetic north (Figure 4.2). Each scan location is considered a plot for the TLS metrics derived from a single scan. The edge scans and sphere placement had to have a significant amount of leniency in the actual location. If extremely dense vegetation or a large tree occupied the preferred location of placement, the closest location to the preferred location that allowed for the surveying of the largest amount of the site was chosen. This scanning location selection criteria inevitably biased the scans against locations with near total occlusion, but that bias was deemed better than potentially missing as much as 50% of an area due to the scanner being placed directly next to a large tree.

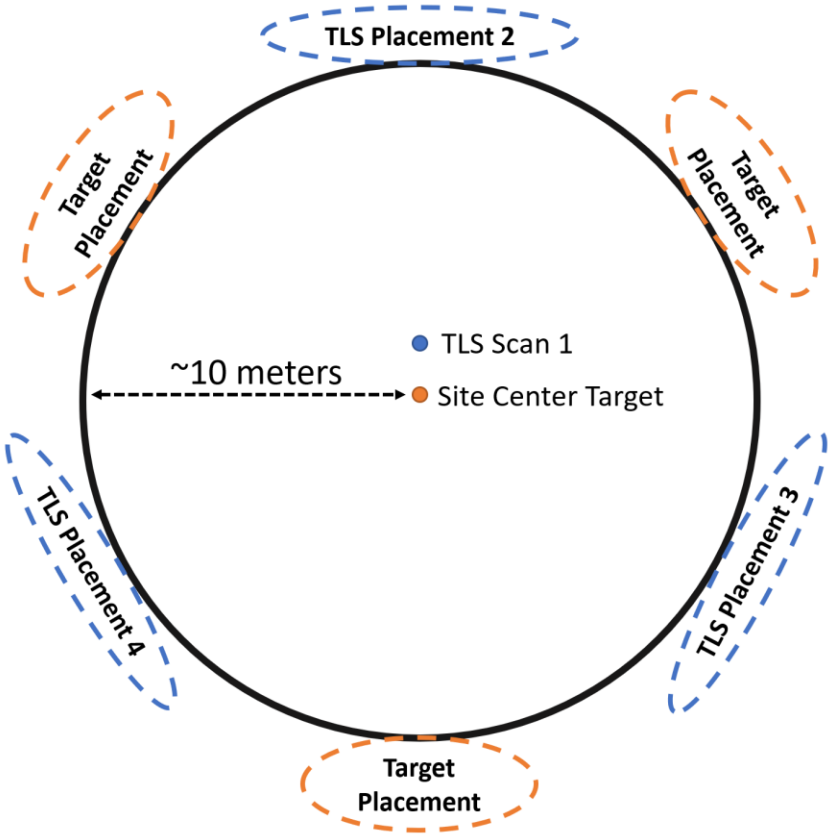

Figure 4.2 *Diagram of TLS scanning locations and target spheres used for co-registration of the scans. Each site had 4 TLS scans (plots). The oblong shape of the exterior sphere and scan locations is because precise placement was often not possible due to vegetation occlusion.*

2.4 TLS Pre-processing and Georectification

The pre-processing of the scans was performed in the program FARO Scene (FARO, n.d.). Two different processing workflows were used depending on if the scans were to be used for "Digital Cover Board" (DCB) or "Voxelization". For the DBC, scans had all position data removed ensuring that the scan center was at a 0, 0, 0 positional index. No point filtering was done on the scans to ensure that all potentially valid points were included. TLS noise and edge effects have little effect on the DBC process, as a 2D depth map is created from the point cloud and trailing points from an object due to the inherent edge effects of TLS aren't visible when creating a raster of the view from the scanner. Removing points through filtering, however, can create gaps in the depth raster giving an impression of increased openness. A las output file was created from the FARO scene and brought into the opensource lidar processing program Cloud Compare

(CloudCompare 2019). Cloud Compare was used to generate a depth map from each TLS scan using the scanning resolution to define the number of rows and columns in the output raster. ASCI image files were produced for each scan.

Pre-processing for the voxelization technique was also done in FARO Scene. Colorization of the point cloud was done by applying the color captured by the lidar unit camera to the point clouds. Edge effect filtering as well as removing scan points with exceedingly low reflectance values was also done. Las files were exported from FARO Scene and brought into Cloud Compare. Co-registration of scans was done within Cloud Compare. Target spheres, tree branches, and ground features were used to place the scans in correct alignment relative to each other. Scans had a rough approximation of location and elevation from the GPS receiver and altimeter on the FARO unit. The coordinate system was converted to the projection Washington State Plane south (EPSG:2927) to match the coordinate system of the airborne lidar data of the area. The initial approximate location of the TLS scans was used to aid the manually conducted fine registration of the TLS scans to the ALS data. Priority was given to matching the ground points of the TLS and ALS scans rather than the points from the vegetation. X and y coordinates of the TLS scans were determined by matching a minimum of 10 shared tree locations between the point clouds, then the z coordinate was determined by matching ground points. Ground models of sites were created using joined TLS and ALS point clouds. These ground models were used to normalize the height of both the TLS scans and the corresponding ALS point cloud tiles. Lidar point cloud normalization removes elevation from the z values of the points, so the z values then reflect the height above ground. 10 m radius point cloud clips were taken at each scan plot location from the individual TLS point clouds and the ALS point cloud.

2.5 TLS Digital Cover Board (DCB)

The DBC method is the process of determining, at a defined height increment at the plot, how far each pulse traveled before coming into contact with a surface (depth), as well as determining if a pulse interacted with a surface at all (openness) (Batchelor et al., 2023). A 2D depth map of TLS scans can be created by generating a raster where each pixel represents a location where a laser pulse was sent. This is determined by the scan line resolution when the scan was taken. With a scan line resolution of 0.035° in both the vertical and horizontal axis of the scanner, the resulting raster will have ~10,286 columns (360° / 0.035°) and ~4,286 rows (150° / 0.035°). Each pixel represents the distance traveled by the laser pulse at the angle increment, with a null

value returned at locations where there was no pulse return (Figure 4.3). The value of each pixel is the distance from the scanner. A basic raster analysis can determine which pixels were within a set distance of the scanner, and which pixels exceeded that distance. In areas where there is a constant gradient of distances (i.e., line of sight not occluded by close vegetation), it is possible to identify the location on the horizon of the image a set distance away from the scanner (Figure 4.3).

We generated two distinctly different sets of metrics from the DBC. The first set used a distance threshold of 10 m radius from the scan position and the second used a distance threshold of 15 m. The 10 m distance was used to match the desired model output resolution of 20 m pixels. The 15 m distance was used to replicate as closely as possible the coverboard transect method currently used to assess lynx habitat suitability. For both methods, a vertical swath (ribbon) of pixels, from the 2D depth rasters, contoured to the plot topography was created (Figure 4.3). A simple horizontal ribbon is not possible unless the scan was taken on a perfectly flat plane. The ribbon will have a high side and a low side in a depth map if the scan was taken on a hill.

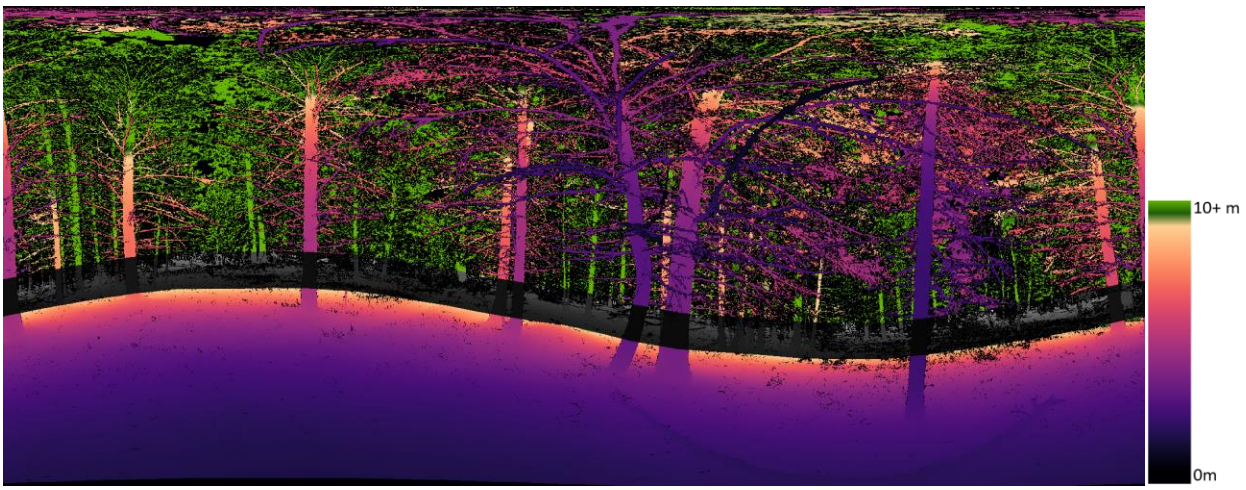

Figure 4.3 *A 2D depth map of a TLS scan. This is a 2D representation of the full 360° scan; i.e., the left and right of the image are the same location in space. The wave like contour of the land in the image is actually looking uphill (the high point on the left), and downhill (the low point on the right). All point returns more than 10 m from the scanner are colored green. The ground level at 10 m is determined and a "digital cover board" (DBC) is placed, represented here by the points colored as grey scale.*

With this horizon line identified, a continuous "digital cover board" can be ribboned around the entire 360° view from the scanner. For the 10 m distance threshold, the height of the ribbon used to represent a 2 m tall cover board was ~326 pixels. The angular increment from the scanner to a height of 2 m from a distance of 10 m is 11.42° (Figure 4.4). With every pixel representing a 0.035° scan line, the number of pixels a 2 m tall coverboard would occupy is 11.42° / 0.035°, approximately 326. There was some variation in the total number of pixels per digital cover board based on the amount of curvature in the ribbon. This was due to clipping square pixels to fit a curved line. Statistics of this 326-pixel wide, wave-like ribbon were calculated for the DBC metrics. The metrics derived from this DBC method were: total number of pixels within the ribbon, number of pixels with some value other than null which represents total cover, total percent cover, number of pixels with a value equal or less than 10, percentage of pixels with a value less than 10 (i.e., percentage of view with cover within 10 m of plot center), mean distance to cover, and standard deviation of distance to cover.

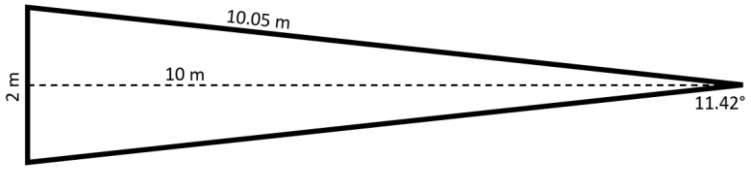

Figure 4.4 *The dimensions of the view area of an object 2 m tall, 10 m away from the TLS. The number of pixels within the depth raster representing 2 m is calculated by dividing the angular view (11.42°) by the scan angle increment (0.035°).*

Similarly, for the 15 m distance threshold digital coverboard, the horizon line was identified, and a ribbon placed. To mimic the current coverboard protocols (Quade and Minkova, 2006), we placed a 2 m tall ribbon 1.5 m above the ground and then subdivided the ribbon into 0.3 m sections as if there were individual 2 m x 0.3 m coverboards surrounding the center scan location. The number of these "coverboards" that had no vegetation occluding them were counted for each scan (Figure 4.5).

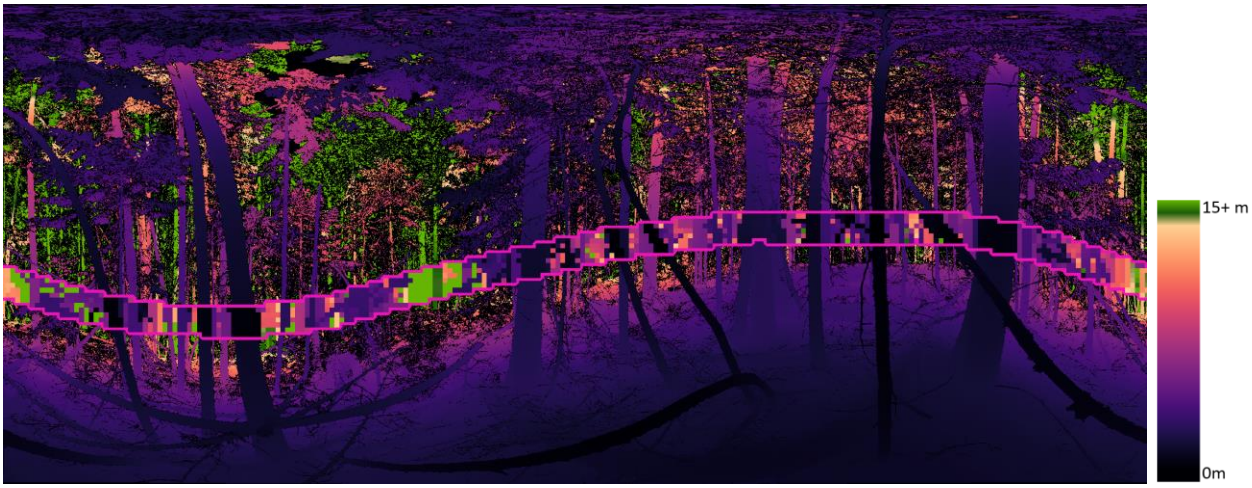

Figure 4.5 *A depth raster of a scan with all pixels further than 15 m colored green. The down sampled pixel ribbon in the image (outlined in magenta) represents a series of 2 m x 0.3 m coverboards surrounding the central viewpoint at 15 m distance and 1.5 m above ground. A clear coverboard as defined by the lynx survey protocols would be the bottom two cells in the line all colored green.*

4.3.4 *TLS Voxelization*

Voxelization is the three-dimensional gridding of the total extent of a point cloud at a defined resolution. To indicate occupancy, a voxel was given a value of 1 if at least one lidar point is within the voxel, and a 0 if no points are within the voxel. A voxel is given a value of 1 whether there is 1 point or 1,000+ points within the cell area. This is a method of normalizing the point density across an area as point density is inherently higher the closer to the scanner the grid cell is. For all metrics derived from point clouds, the R package lidR was used (Roussel et al., 2020; Roussel and Auty, 2021). We chose a voxel size of 10 cm x 10 cm x 10 cm (1000 cm^3) (hereafter referred to as simply 10 cm voxel) for each height normalized point cloud. A 10 cm voxel size has previously been shown to be an optimal size for quantifying viewsheds from TLS and canopy gap estimates (Ross et al., 2022; Zong et al., 2021). Voxelization was done on each individual scan clipped at 10 m from plot center. Volatilization was not done on the mosaiced scans, as the variable amount of occlusion at each site would have biased voxel counts toward relatively open areas. The open areas had near-perfect capture of vegetation from the TLS while sites with dense understory had a large amount of occlusion present. Creating voxel counts from a single point scan slightly changed

the metric measured by the voxelization to the area occupied by vegetation seen from the scanner rather than a true measure of area occupied by vegetation.

The 10 cm voxels were then summarized into 0.5 m resolution cubes (Figure 4.6). Voxel metrics were stratified into 0.5 m height bins so the resulting metrics were expressed in half meter increments above ground. Voxel statistics were calculated for all 0.5 m height strata from the ground to 3 m (Table 4.1).

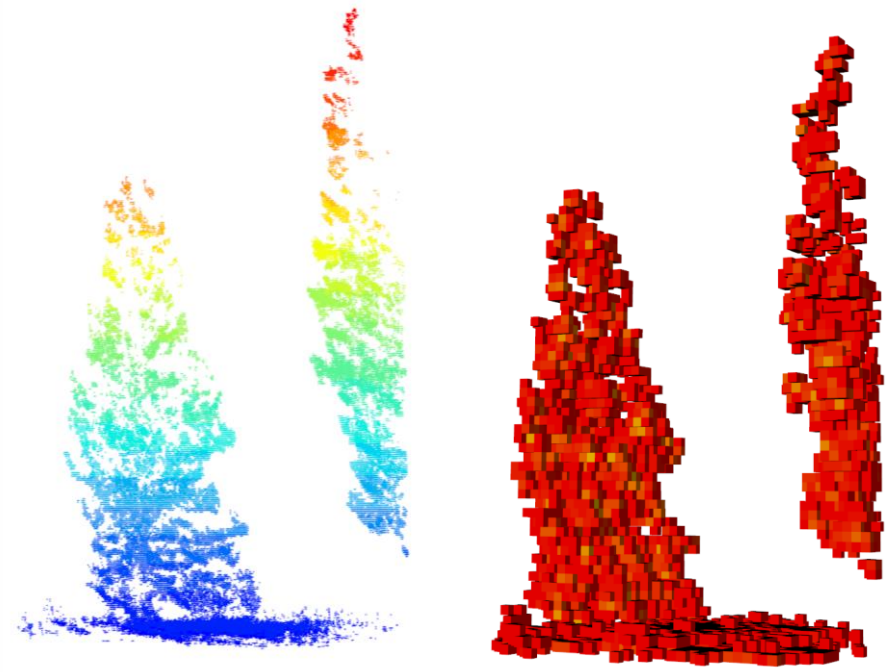

Figure 4.6 *A voxelized and normalized TLS point cloud (left) with each point representing centroid of a 10 cm cube. A voxel summary model (right) where each 0.5 m resolution cube is colored by the number of occupied 10 cm voxels contained within it.*

Table 4.1 *Summary table of the metrics derived from the terrestrial lidar point clouds. In total, 42 metrics were created from the digital cover board (DCB) depth maps and voxelization approaches.*

TLS METRICS	
10 M DCB	Total percentage of cover, number of pixels, percentage of cover within 10 m, mean distance and standard deviation to all pixels and cover pixels at 10 m (7 of the 42 metrics)
15 M DCB	Percentage of cover within 15 m per down sampled pixel, percentage of cover within 15 m per vertical column of pixels, percentage of vertical columns with no cover, mean distance and standard deviation to all pixels and cover pixels at 15 m. (8 of the 42 metrics)
VOXELIZATION	Total count of 10 cm voxels per 0.5 m height stratum, mean count of 10 cm voxels per 0.5 m cube, count of 0.5 m cubes with 1 or more 10 cm voxels per height stratum. (27 of the 42 metrics)

4.3.5 *ALS Data*

The airborne lidar data covering the entire Loomis state forest were collected in early June 2016. Data was collected using an Optech Galaxy Lidar System with an average pulse density of ~12 pulses/m2 and minimum 50% overlap. RGB imagery was used to color the ALS point cloud. The airborne lidar data for the Little Pend Oreille Forest were collected in July 2016 also using an Optech Galaxy Lidar System with an average pulse density of ~3 pulses/m2 and minimum 50% overlap. The 2016 data was the only ALS available for the study area resulting in a 5 to 6-year difference between the acquisition of the ALS data and the TLS data; however, good point matching between ALS and TLS scans was still possible.

ALS point clouds were subdivided to test if a partial cloud produced a better model. Along with the full ALS point cloud, subdivisions using only the first returns, only the last returns, all points less than 2 m above ground, and all points less than 2 m above ground but higher than 0.5 m above ground (Figure 4.7). Typical ALS metrics using z values and intensity values were created

for each grouping of ALS points (Table 4.2). In addition to direct measurements of point distributions, ratios of points were also calculated. For each of the point sets, the cumulative percentage of returns (CPR) at 9 defined height strata relative to the local z maximum was calculated (Woods et al., 2008). The overall relative point density (ORD) each point set and normalized relative point density (NRD) were also calculated (Campbell et al., 2018)

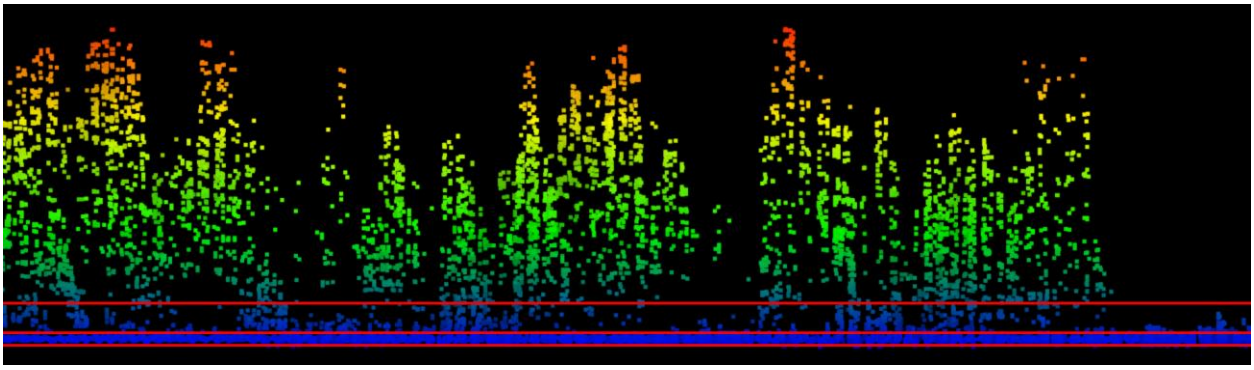

Figure 4.7 *Normalized ALS point cloud with ground, 0.5 m above ground, and 2 m above ground denoted with the red lines. These lines illustrate the subdivisions of the ALS point cloud that were used for ALS metric generation. First and last return sub selections were also created for ALS metric generation (not shown).*

Table 4.2 *Summary table of the metrics derived from the airborne lidar point clouds. In total 286 metrics were created from the ALS data.*

ALS METRICS	
POINTS USED	All points, only first returns, only last returns, all points < 2 m in height, points > 0.5 m and < 2 m in height. (5 groups of points)
Z AND INTENSITY METRICS	Count, sum, max, mean, standard deviation, skew, kurtosis, percentage above mean, 19 height percentiles (5^{th} to 95^{th} percentile), & mean intensity at height percentiles. (47 per group, 235 total)
RATIOS	CPR for each point group (9 per group, 45 total), and ORD and NRD (6 total)

4.3.6 *Statistical Analysis*

An overabundance of metrics was produced from both the TLS and ALS data. Exploratory analysis was done to determine: 1) What TLS metrics best described the variation among plots, 2) If regression models or categorical data and machine learning modeling produced the best results, and 3) What subset of ALS metrics either had the highest correlation with TLS data or were the best performing predictors in a machine learning approach.

A principal components analysis was performed on the 42 TLS metrics to determine which metrics best described the variation between plots. All metrics were normalized before PCA analysis. TLS metrics that contributed highly to the first principal component (PC1) were used for a full stepwise regression analysis with all derived ALS metrics. They were also broken into ordinal categories of high and low understory cover to be used in training and testing the machine learning algorithms random forest and extreme gradient boosting (xgboost) using a 70% training 30% testing split (Chen and Guestrin, 2016).

4.4 Results

4.4.1 *TLS PCA*

Of the 42 TLS metrics that were used for the PCA, the four metrics that most contributed to principle components axis 1 were: Voxel Count 1.5 to 2 m, Voxel Count 2 to 2.5 m, Voxel Cubes at 1.5 m, and Digital Cover Board. These four metrics will be refered to as “PC1 Metrics” hereinafter. The four metrics that most contributed to the principle components axis 2 was the mean for the height stratas of 2.5 m to 3 m, 2 m to 2.5 m, 1.5 to 2 m, and 3 m to 3. 5 m (Figures 4.8 and 4.9).

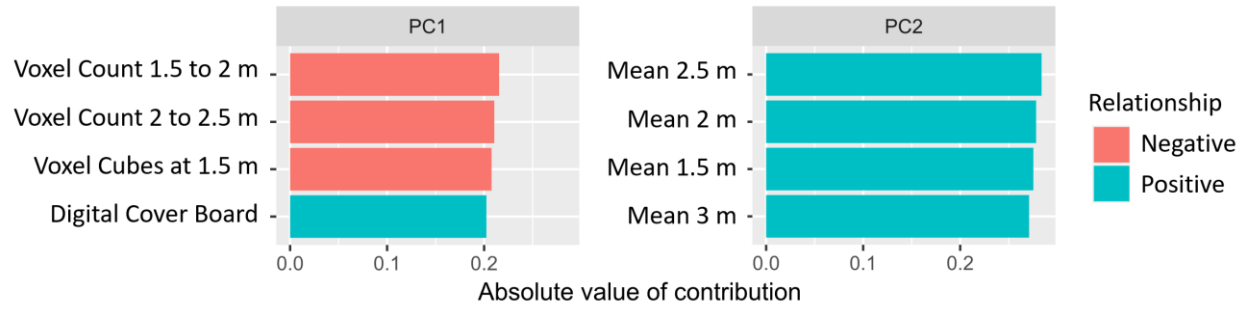

Voxel Count: The total number of 10 cm voxels at defined height

Voxel Cubes: The total number of 50 cm cubes that contained at least one 10 cm voxel at defined height.

Digital Cover Board: The percentage of open cells from the DCB at 1.5 to 2 m

Mean: The average number of 10 cm voxels per 50 cm cube at defined height.

Figure 4.8 *The top four contributors to PC axis 1 and 2 with their absolute value of contribution amongst the 42 metrics reported. 7 of the 8 metrics were products of voxelization with only 1 being a digital cover board metric.*

Our 15 m DCB metic that followed current lynx management criteria of determining percentage of fully visible coverboard quadrants at 1.5 m to 2 m height was not a significant contributor to PC 1 or 2, however, the count of DCB cells visable at 15 m was the 4th contributor to PC 1.

The PCA plot of the TLS metics is presented in Figure 4.9. High cover and low cover classes were determined by using the DCB percentage metric with plots with more than 90% of DCB occluded cells counting as cover. There was an even split of plots that were High Cover (80 plots) vs Low Cover (80 plots) in our data.

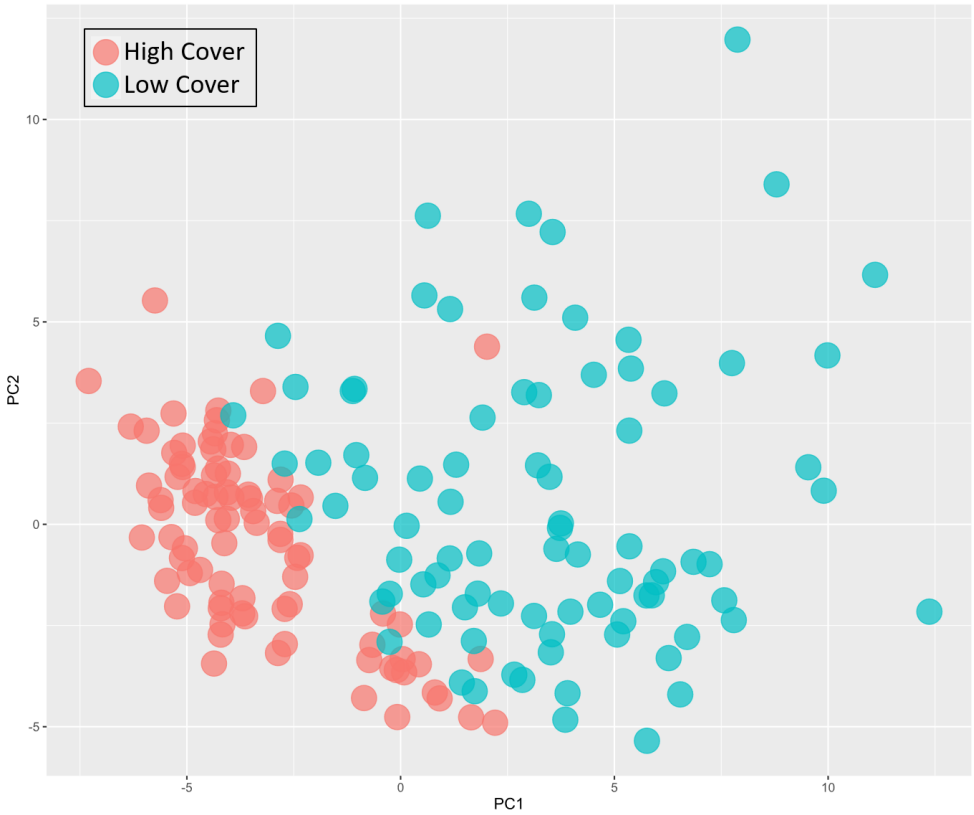

Figure 4.9 *The PCA plot of the TLS metrics. Points are colored by TLS digital coverboard metrics considering "High Cover" to be a plot where only 10% of the digital cover board pixels are visible.*

4.4.2 *Models*

Models were developed to predict TLS cover metrics from ALS metrics to produce area-wide rasters of predicted TLS cover metrics. All models performed worse when combining the data from the Loomis State Forest with the data from Little Pend Oreille State Forest. For all the final models, the Loomis State Forest data was run alone. The Loomis State Forest had 32 of the 40 total sites. With each site comprised of 4 scan plots, 128 plots were used for the modeling. Using a 70% training, 30% testing split, 90 plots were used for training with 38 plots used for testing.

4.4.2.1 Regression

Stepwise regression analysis was done using each of the individual TLS understory horizontal cover metrics that most contributed to PC1, and the collection of ALS metrics. While there were statistically significant relationships between each of the four TLS cover metrics and a collection of the ALS metrics using a forward and backwards stepwise regression analysis ($P<0.05$), R^2 values did not increase above 0.3. We were not able to find a satisfactory regression model to predict any of the TLS horizontal cover metrics from ALS.

3.2.2 Machine Learning

The 4 PC1 metrics were converted into ordinal data of High Cover and Low Cover with 50% of the training data (45 plots) assigned the high cover label and the other half assigned the low cover label. For the DCB metric, the high cover class was comprised of plots with greater than 90% cover and the low cover class were plots that had less than 90% cover. This threshold of 90% cover corresponds to the WA DNR protocols of 4 or fewer open views out of the 40 observations are considered to have sufficient cover for forage habitat.

XgBoost produced higher accuracy models than random forest. The xgboost models using ALS data to predict the ordinal cover class from TLS data had a total accuracy of less than 70% when using the high cover / low cover split as determined from each of the 3 voxel based PC1 metrics (Voxel Count 1.5 to 2 m, Voxel Count 2 to 2.5 m, Voxel Cubes at 1.5 m). However, using the DCB PC1 metric, a model accuracy of 85% was achieved with the testing data, with area under the ROC Curve set at 0.92. Of the 284 ALS metrics that were used in the model, 279 were removed from the final model, as only 5 ALS metrics were needed to produce our final model <2 m 95p, <2 m SD, <2 m I 70%, All SD, All 95p (Figure 4.10).

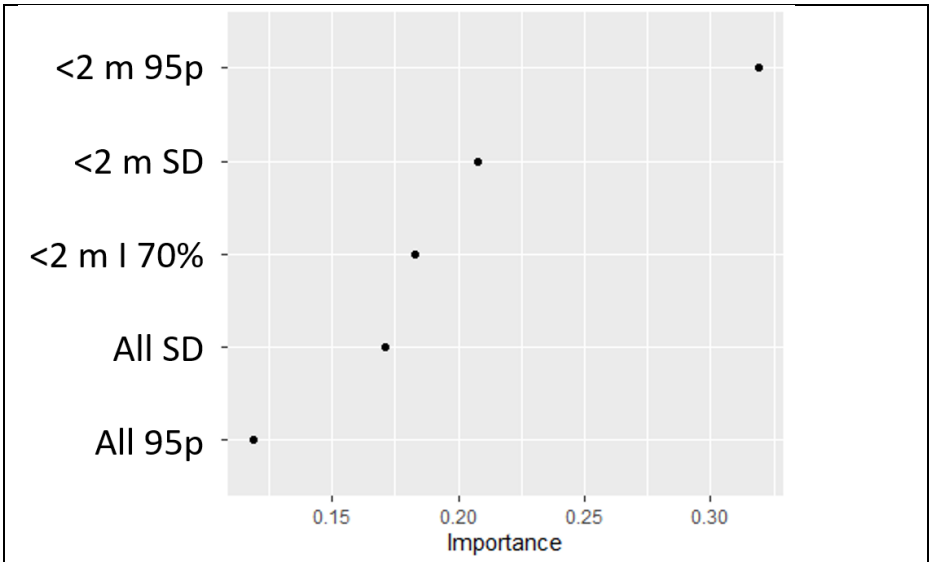

<2 m 95p: The height of the 95th percentile of all points below 2 m.

<2 m SD: The Standard deviation of all points below 2 m.

<2 m I 70%: Mean intensity of points located in the lower 70% of 2 m (1.4 m)

All SD: The Standard deviation of all points

All 95p: The height of the 95th percentile of all points

Figure 4.10 *The relative importance of each of our 5 ALS model inputs for our final xgboost model. The final model had a testing accuracy of 85% with the 2 class ordinal data of 'High Cover', 'Low Cover' being determined by the TLS DCB method.*

4.4.2.2 Model Output

The xgboost model produced a binary model of low cover / high cover. A third category was added to the final model output of 'No Cover' (Figure 4.11). This third category was created by labeling all areas with no ALS returns greater than 2 m as no cover. This would account for the area within the Loomis that were not forested.

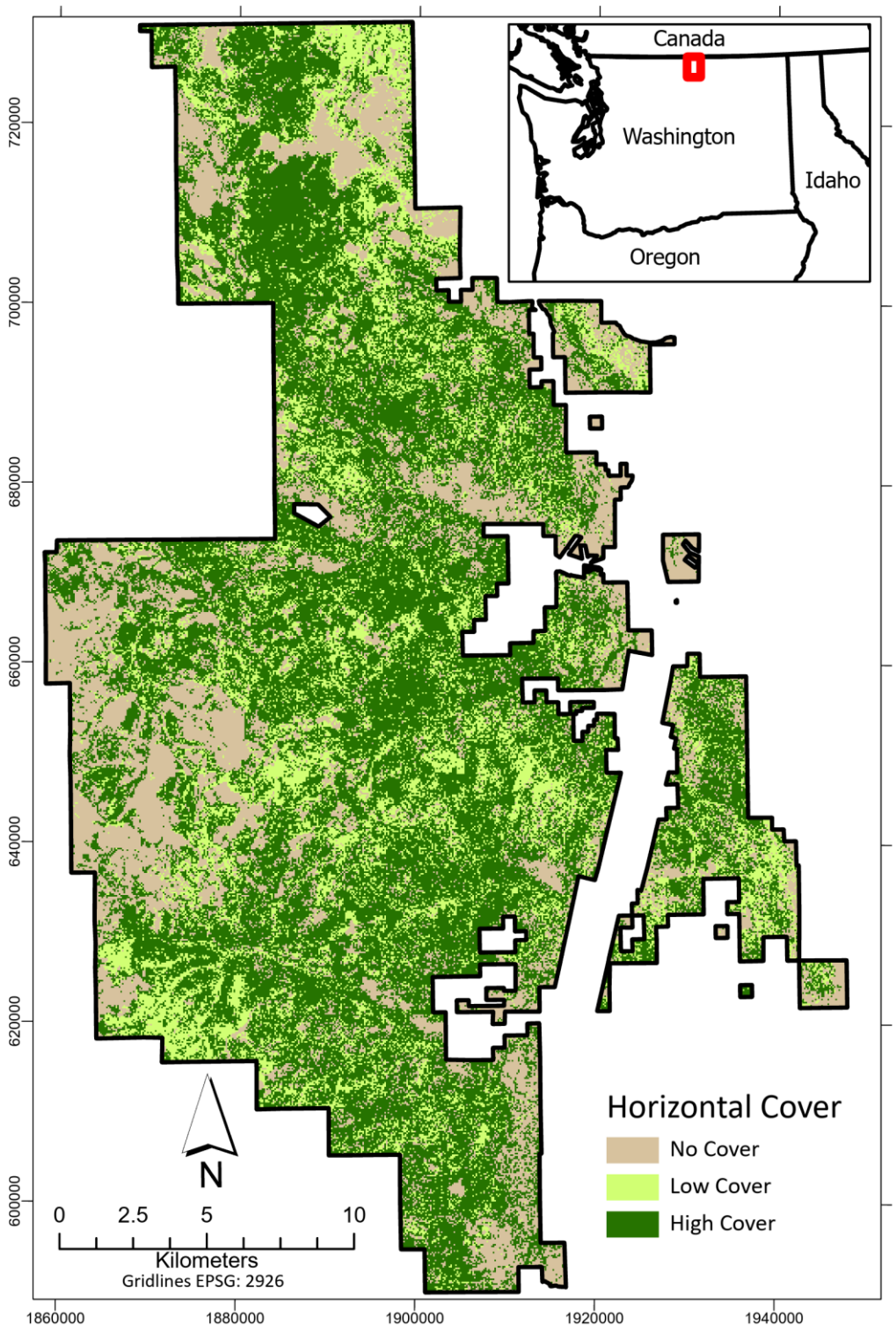

Figure 4.11 *The xgboost model output for the Loomis State Forest. Low and High cover categories were created using the machine learning approach with an 85% accuracy. The no cover class are areas that had no ALS returns over 2 m. This map was derived using 2016 ALS data.*

4.5 Discussion

4.5.1 *TLS Metrics*

The TLS metrics that accounted for the greatest amount of variation between plots all related to vegetation structure between 1.5 to 2 m above ground level (Figure 4.7). This corresponds to the vegetation height stratum that is considered important for snowshoe hare and thus lynx habitat (Koehler, 1990; Litvaitis et al., 1985; Vanbianchi et al., 2017). This validates our TLS metrics as ecologically meaningful for quantifying a difference between poor habitat structure and preferred habitat structure. Of the 4 metrics that accounted for the greatest plot variability, our digital coverboard metric produced the best model. Terrestrial lidar has been shown to be effective at quantifying horizontal cover (Batchelor et al., 2023; Olsoy et al., 2015; Zong et al., 2021) so we did not directly compare our metrics with traditional methods such as coverboards. While we believe our metrics are robust measurements of horizontal cover, more research should be conducted to explore relationships between TLS metrics and population data for snowshoe hare beyond a quantification of cover.

The number of studies using TLS for habitat characterization is increasing as well as the sophistication of the approaches. For example, a form of the DCB metric has been previously used to quantify forest structure (Batchelor et al., 2023; Richardson et al., 2014), but this study is the first we are aware of that directly applies this approach to habitat quantification. There has been previous work using TLS for understory habitat classification (Burgett et al., 2021; Galluzzi et al., 2022) as well as excellent R packages that have been developed to quantify viewshed specifically for habitat characterization (Lecigne et al., 2020). The advantage of our metrics is the ability to be applied to single point TLS scans as well as account for slope. This work and others speak to the utility of this technology to produce high fidelity and objective estimates of forest structure related to habitat requirements for numerous different species.

One limitation of the TLS voxel methods is that the voxel counts were derived from a single point scan. The final voxel counts are measurements of "How much stuff is visible from the scanner location" and not a true measurement of "How much stuff is there". While there are drawbacks to single-point scans, they are similar to ocular estimates of cover done by an observer at a single point. To fully utilize a voxelization method, multiple scans stitched together must be used for a near complete scan of all vegetation structure (Béland et al., 2014; Soma et al., 2021). Having

a near complete scan of all vegetation from multiple scans is relatively easy in open stands, however, many of our stands had dense understory vegetation with high amounts of occlusion. In such areas, the amount of single point scans that would have been required for a complete sampling was infeasible to collect. Further, with every additional scan compiled into a stitched together TLS scene, the likelihood of error increases due to either slight misalignments between scans or some environmental factor such as wind actually moving the vegetation. Using single scans allowed for the method to be applied universally across stands. Using a mobile terrestrial lidar unit such as a backpack or wand device may allow for better data collection in regards to voxelization, but it would be unlikely that quality depth rasters could be produced given the lower level of point accuracy inherent in mobile lidar units (Bauwens et al., 2016; Donager et al., 2021).

4.5.2 *ALS Metrics*

The ALS data were collected in 2016 while the TLS data were collected in 2022. This 6-year time gap, a common occurrence in remote sensing research, presented some additional challenges beyond a normal ALS / TLS alignment. While the 2016 ALS data was the most recent lidar data available, there were areas where significant disturbances occurred (e.g., logging & fire) in the interim and had to be removed from analysis. That we were still able to produce a model with 85% accuracy despite this age gap indicates the utility of lidar acquisitions for forest structure characterization years after the initial lidar acquisition where tree growth rates are relatively slow, as in this study area.

ALS area-based metrics typically look at the vertical arrangement of points within a defined plot size. Characterizing the vertical arrangement of points using simple metrics has been the subject of extensive research. Percentile heights of points is one of the most common metrics derived from lidar along with ratios of points below and above a defined threshold (Coops et al., 2021; Gobakken and Næsset, 2005; Qu et al., 2018; Simonson et al., 2014). For our study we derived 286 different metrics from ALS informed by reviewing methods used in previous forest structure research. We identified 5 metrics from the 286 that allowed for a high model fit using xgboost. Three of the 5 metrics used a subset of the point cloud of points below 2 m while the other 2 metrics used all point returns. The 95th percentile height and the SD of points are lidar metrics that have been shown to be useful when modeling forest structural elements such as tree height, biomass, basal area, and quadratic mean diameter (Estornell et al., 2011; Giannico et al., 2016; Kane et

al., 2010). It is unsurprising that these metrics that are commonly used for modeling biomass are also useful when modeling horizontal cover. The combination of using these metrics from both the full point cloud as well as the points below 2 m may indicate that for future studies utilizing ALS for forest structure characterization, combining subsets of the data along with the full point cloud may provide more robust models. The fifth metric used was the mean intensity of points located in the lower 70% of 2 m (1.4 m). An important caveat when using intensity values from aerial lidar is that they are usually not calibrated to permit comparison between acquisitions (Fritzmann et al., 2011; Yan et al., 2012). Intensity values vary depending on the distance, angle, and surface that is reflecting the lidar pulse (Kashani et al., 2015; Song et al., 2002). That different surfaces return different lidar intensity is likely key to why it is an important predictor of understory vegetation conditions. If in the lower 1.4 m of a forest there is a lot of vegetation, a different intensity value should be received than if there is a lack of vegetation and more visible soils or duff. When working within a single ALS acquisition, lidar intensity without calibration can still be effectively used to aid in differentiation between ground cover classes (Reymann and Lacroix, 2015; Simoniello et al., 2022).

4.5.3 *Model Fit*

Our 85% accuracy rate was achieved when only using the Loomis State Forest plots and the Loomis ALS data. We had to remove our Little Pend Oreille plots from the analysis. We felt it was important to include the mention that both study areas were initially collected for analysis because it illustrates that a model generated using lidar data from one lidar acquisition may not be applicable to a different lidar data set collected with a different pulse density in a different forest. A model could not be generated that performed well for both forests. With only 8 sites located within the Little Pend Oreille State Forest, it is reasonable to assume that our poor model fits for the area were partially due to the small sample size.

Our model also did not consider spatial autocorrelation between plots. Previous work producing landscape models from remote sensing data leveraged spatial autocorrelation to improve overall model fits (Xu et al., 2023). Our methods were not reliant on spatial interpolation to derive a final model but were rather depending on the vertical distribution of lidar points for model fit regardless of the x, y location of the raster cell. Errors or enhancements for model fits due to spatial

autocorrelation are of most concern when using interpolation methods (Aulló-Maestro et al., 2021; Gilbert and Lowell, 1997).

4.6 Conclusion

Our final model output was a 20-m resolution raster of 3 horizontal-cover classes (no cover, low cover, and high cover). No filtering was done to identify contiguous areas of high cover large enough to meet lynx habitat requirements. Our model outputs show whether each individual 20 m grid cell had ALS point values that were likely to be indicative of high or low horizontal cover. We conclude that our model of understory horizontal cover could be used in conjunction with other key habitat considerations to inform a more holistic and connectivity sensitive habitat model.

Beyond the utility of TLS to generate an objective measurement of understory horizontal cover, we believe that other important forest metrics could also be modeled with our TLS metrics. TLS is already widely used to quantify biomass, map tree stems, determine tree diameters, and other forest metrics (Demol et al., 2022; Holopainen et al., 2011; Raumonen et al., 2015; Xu et al., 2021), but the utility of single point TLS scans for forest mensuration needs more research. We feel that our approach to spatial modeling from single point TLS scans will be of great interest to forest managers and conservationists in need of an objective and time efficient method to quantify horizontal cover as it relates to habitat suitability for other wildlife species, among broader applications such as forest inventory and carbon storage.

4.7 References

Ashcroft, M.B., Gollan, J.R., Ramp, D., 2014. Creating vegetation density profiles for a diverse range of ecological habitats using terrestrial laser scanning. Methods Ecol. Evol. 5, 263–272.

Aulló-Maestro, I., Gómez, C., Marino, E., Cabrera, M., De La Cueva, A.V., Montes, F., 2021. Integration of field sampling and LiDAR data in forest inventories: comparison of area-based approach and (lognormal) universal kriging. Ann. For. Sci. 78, 39. https://doi.org/10.1007/s13595-021-01056-1

Batchelor, J.L., Wilson, T.M., Olsen, M.J., Ripple, W.J., 2023. New Structural Complexity Metrics for Forests from Single Terrestrial Lidar Scans. Remote Sens. 15, 145. https://doi.org/10.3390/rs15010145

Bauwens, S., Bartholomeus, H., Calders, K., Lejeune, P., 2016. Forest Inventory with Terrestrial LiDAR: A Comparison of Static and Hand-Held Mobile Laser Scanning. Forests 7, 127. https://doi.org/10.3390/f7060127

Béland, M., Baldocchi, D.D., Widlowski, J.-L., Fournier, R.A., Verstraete, M.M., 2014. On seeing the wood from the leaves and the role of voxel size in determining leaf area distribution of forests with terrestrial LiDAR. Agric. For. Meteorol. 184, 82–97.

Beland, M., Parker, G., Sparrow, B., Harding, D., Chasmer, L., Phinn, S., Antonarakis, A., Strahler, A., 2019. On promoting the use of lidar systems in forest ecosystem research. For. Ecol. Manag. 450, 117484.

Blomdahl, E.M., Thompson, C.M., Kane, J.R., Kane, V.R., Churchill, D., Moskal, L.M., Lutz, J.A., 2019. Forest structure predictive of fisher (Pekania pennanti) dens exists in recently burned forest in Yosemite, California, USA. For. Ecol. Manag. 444, 174–186. https://doi.org/10.1016/j.foreco.2019.04.024

Bouvier, M., Durrieu, S., Fournier, R.A., Renaud, J.-P., 2015. Generalizing predictive models of forest inventory attributes using an area-based approach with airborne LiDAR data. Remote Sens. Environ. 156, 322–334. https://doi.org/10.1016/j.rse.2014.10.004

Burgett, S., Rachlow, J., Stein, R., 2021. Unexpected Properties of Habitat Altered by Ecosystem Engineers: A Pygmy Rabbit Case Study [WWW Document]. Boise State Univeristy. URL https://scholarworks.boisestate.edu/icur/2021/poster_session/12/ (accessed 12.16.22).

Campbell, M.J., Dennison, P.E., Hudak, A.T., Parham, L.M., Butler, B.W., 2018. Quantifying understory vegetation density using small-footprint airborne lidar. Remote Sens. Environ. 215, 330–342.

Chen, T., Guestrin, C., 2016. Xgboost: A scalable tree boosting system, in: Proceedings of the 22nd Acm Sigkdd International Conference on Knowledge Discovery and Data Mining. pp. 785–794.

CloudCompare [Computer Software]; Version 2.11; 2019. Available online: http://www.cloudcompare.org (accessed on 1 March 2021)., 2019. . (GPL software).

Collins, W.B., Becker, E.F., 2001. Estimation of horizontal cover. 54. https://doi.org/10.2458/azu_jrm_v54i1_collins

Coops, N.C., Tompalski, P., Goodbody, T.R., Queinnec, M., Luther, J.E., Bolton, D.K., White, J.C., Wulder, M.A., van Lier, O.R., Hermosilla, T., 2021. Modelling lidar-derived estimates of forest attributes over space and time: A review of approaches and future trends. Remote Sens. Environ. 260, 112477.

Demol, M., Verbeeck, H., Gielen, B., Armston, J., Burt, A., Disney, M., Duncanson, L., Hackenberg, J., Kükenbrink, D., Lau, A., 2022. Estimating forest above-ground biomass with terrestrial laser scanning: Current status and future directions. Methods Ecol. Evol. 13, 1628–1639.

Donager, J.J., Sánchez Meador, A.J., Blackburn, R.C., 2021. Adjudicating Perspectives on Forest Structure: How Do Airborne, Terrestrial, and Mobile Lidar-Derived Estimates Compare? Remote Sens. 13, 2297. https://doi.org/10.3390/rs13122297

Elton, C., Nicholson, M., 1942. The ten-year cycle in numbers of the lynx in Canada. J. Anim. Ecol. 215–244.

Estornell, J., Ruiz, L.A., Velázquez-Martí, B., Fernández-Sarría, A., 2011. Estimation of shrub biomass by airborne LiDAR data in small forest stands. For. Ecol. Manag. 262, 1697–1703.

Farhani, G., Sica, R.J., Daley, M.J., 2021. Classification of lidar measurements using supervised and unsupervised machine learning methods. Atmospheric Meas. Tech. 14, 391–402. https://doi.org/10.5194/amt-14-391-2021

FARO, n.d. Scene [Computer Software]; Version 2019.2 (7.5.5.4303); FARO: Lake Mary, FL, USA. 2021. Available online: http://www.faro.com (accessed on 25 August 2023).

Fekety, P.A., Sadak, R.B., Sauder, J.D., Hudak, A.T., Falkowski, M.J., 2019. Predicting forest understory habitat for Canada lynx using LIDAR data. Wildl. Soc. Bull. 43, 619–629.

Fritzmann, P., Höfle, B., Vetter, M., Sailer, R., Stötter, J., Bollmann, E., 2011. Surface classification based on multi-temporal airborne LiDAR intensity data in high mountain environments, A case study from Hintereisferner, Austria. Z. Für Geomorphol. Suppl. Issues 105–126. https://doi.org/10.1127/0372-8854/2011/0055S2-0048

Fuller, A.K., Harrison, D.J., 2010. Movement paths reveal scale-dependent habitat decisions by Canada lynx. J. Mammal. 91, 1269–1279.

Galluzzi, M., Puletti, N., Armanini, M., Chirichella, R., Mustoni, A., 2022. Mobile Laser Scanner understory characterization: an exploratory study on hazel grouse in Italian Alps. bioRxiv.

García-Gutiérrez, J., Martínez-Álvarez, F., Troncoso, A., Riquelme, J.C., 2015. A comparison of machine learning regression techniques for LiDAR-derived estimation of forest variables. Neurocomputing 167, 24–31. https://doi.org/10.1016/j.neucom.2014.09.091

Giannico, V., Lafortezza, R., John, R., Sanesi, G., Pesola, L., Chen, J., 2016. Estimating stand volume and above-ground biomass of urban forests using LiDAR. Remote Sens. 8, 339.

Gilbert, B., Lowell, K., 1997. Forest attributes and spatial autocorrelation and interpolation: effects of alternative sampling schemata in the boreal forest. Landsc. Urban Plan. 37, 235–244. https://doi.org/10.1016/S0169-2046(97)80007-2

Gleason, C.J., Im, J., 2012. Forest biomass estimation from airborne LiDAR data using machine learning approaches. Remote Sens. Environ. 125, 80–91. https://doi.org/10.1016/j.rse.2012.07.006
Gobakken, T., Næsset, E., 2005. Weibull and percentile models for lidar-based estimation of basal area distribution. Scand. J. For. Res. 20, 490–502.
Gould, P., Strunk, J., Tenneson, K., n.d. Introducing the Remote Sensing Forest Inventory System (RS-FRIS). Version 1.0. Revision 1, June 11, 2015. Internal document. Washington State Department of Natural Resources. Olympia, WA 98506.
Holopainen, M., Vastaranta, M., Kankare, V., Räty, M., Vaaja, M., Liang, X., Yu, X., Hyyppä, J., Hyyppä, H., Viitala, R., 2011. Biomass estimation of individual trees using stem and crown diameter TLS measurements. ISPRS-Int. Arch. Photogramm. Remote Sens. Spat. Inf. Sci. 3812, 91–95.
Huang, H., Gong, P., Cheng, X., Clinton, N., Cao, C., Ni, W., Li, Z., Wang, L., 2009. Forest structural parameter extraction using terrestrial LiDAR. Proc. SilviLaser 2009, 9th.
Hudak, A.T., Evans, J.S., Stuart Smith, A.M., 2009. LiDAR utility for natural resource managers. Remote Sens. 1, 934–951.
Hudak, A.T., Strand, E.K., Vierling, L.A., Byrne, J.C., Eitel, J.U., Martinuzzi, S., Falkowski, M.J., 2012. Quantifying aboveground forest carbon pools and fluxes from repeat LiDAR surveys. Remote Sens. Environ. 123, 25–40.
Ivan, J.S., Shenk, T.M., 2016. Winter diet and hunting success of Canada lynx in Colorado. J. Wildl. Manag. 80, 1049–1058.
Johnston, A.N., Moskal, L.M., 2017. High-resolution habitat modeling with airborne LiDAR for red tree voles. J. Wildl. Manag. 81, 58–72. https://doi.org/10.1002/jwmg.21173
Jorgensen, C.F., Stutzman, R.J., Anderson, L.C., E. Decker, S., Powell, L.A., Schacht, W.H., Fontaine, J.J., 2013. Choosing a DIVA: a comparison of emerging digital imagery vegetation analysis techniques. Appl. Veg. Sci. 16, 552–560. https://doi.org/10.1111/avsc.12037
Kane, V.R., McGaughey, R.J., Bakker, J.D., Gersonde, R.F., Lutz, J.A., Franklin, J.F., 2010. Comparisons between field-and LiDAR-based measures of stand structural complexity. Can. J. For. Res. 40, 761–773.
Kashani, A.G., Olsen, M.J., Parrish, C.E., Wilson, N., 2015. A review of LiDAR radiometric processing: From ad hoc intensity correction to rigorous radiometric calibration. Sensors 15, 28099–28128.
Koehler, G.M., 1990. Population and habitat characteristics of lynx and snowshoe hares in north central Washington. Can. J. Zool. 68, 845–851.
Koehler, G.M., GM, K., MG, H., HS, H., 1979. Lynx movements and habitat use in Montana. Can. Field-Nat. 93, 441–442.
Lecigne, B., Eitel, J., Rachlow, J., 2020. viewshed3d: an R package for quantifying 3D visibility using terrestrial lidar data. Methods Ecol. Evol. 11. https://doi.org/10.1111/2041-210x.13385
Lee, J., Im, J., Kim, K., Quackenbush, L.J., 2018. Machine Learning Approaches for Estimating Forest Stand Height Using Plot-Based Observations and Airborne LiDAR Data. Forests 9, 268. https://doi.org/10.3390/f9050268
Litvaitis, J.A., Sherburne, J.A., Bissonette, J.A., 1985. Influence of Understory Characteristics on Snowshoe Hare Habitat Use and Density. J. Wildl. Manag. 49, 866–873. https://doi.org/10.2307/3801359
Liu, H., Shen, X., Cao, L., Yun, T., Zhang, Z., Fu, X., Chen, X., Liu, F., 2020. Deep learning in forest structural parameter estimation using airborne lidar data. IEEE J. Sel. Top. Appl. Earth Obs. Remote Sens. 14, 1603–1618.
Liu, M., Han, Z., Chen, Y., Liu, Z., Han, Y., 2021. Tree species classification of LiDAR data based on 3D deep learning. Measurement 177, 109301.
Maletzke, B.T., Koehler, G.M., Wielgus, R.B., Aubry, K.B., Evans, M.A., 2008. Habitat conditions associated with lynx hunting behavior during winter in northern Washington. J. Wildl. Manag. 72, 1473–1478.
Marinelli, D., Paris, C., Bruzzone, L., 2022. An approach based on deep learning for tree species classification in LiDAR data acquired in mixed forest. IEEE Geosci. Remote Sens. Lett. 19, 1–5.
Marrs, J., Ni-Meister, W., 2019. Machine Learning Techniques for Tree Species Classification Using Co-Registered LiDAR and Hyperspectral Data. Remote Sens. 11, 819. https://doi.org/10.3390/rs11070819
Murray, D.L., Boutin, S., O'Donoghue, M., 1994. Winter habitat selection by lynx and coyotes in relation to snowshoe hare abundance. Can. J. Zool. 72, 1444–1451.

North, M.P., Kane, J.T., Kane, V.R., Asner, G.P., Berigan, W., Churchill, D.J., Conway, S., Gutiérrez, R.J., Jeronimo, S., Keane, J., Koltunov, A., Mark, T., Moskal, M., Munton, T., Peery, Z., Ramirez, C., Sollmann, R., White, A., Whitmore, S., 2017. Cover of tall trees best predicts California spotted owl habitat. For. Ecol. Manag. 405, 166–178. https://doi.org/10.1016/j.foreco.2017.09.019
Olsoy, P.J., Forbey, J.S., Rachlow, J.L., Nobler, J.D., Glenn, N.F., Shipley, L.A., 2015. Fearscapes: Mapping Functional Properties of Cover for Prey with Terrestrial LiDAR. BioScience 65, 74–80.
Parker, G.R., Maxwell, J.W., Morton, L.D., Smith, G.E.J., 1983. The ecology of the lynx (Lynx canadensis) on Cape Breton Island. Can. J. Zool. 61, 770–786.
Poole, K.G., 2003. A review of the Canada lynx, Lynx canadensis, in Canada. Can. Field-Nat. 117, 360–376.
Poole, K.G., 1994. Characteristics of an unharvested lynx population during a snowshoe hare decline. J. Wildl. Manag. 608–618.
Qu, Y., Shaker, A., Silva, C.A., Klauberg, C., Pinagé, E.R., 2018. Remote sensing of leaf area index from LiDAR height percentile metrics and comparison with MODIS product in a selectively logged tropical forest area in Eastern Amazonia. Remote Sens. 10, 970.
Quade, C., Minkova, T., 2006. 2006 washington DNR lynx management plan. Washington State Department of Natural Resources.
Raumonen, P., Casella, E., Calders, K., Murphy, S., Åkerblom, M., Kaasalainen, M., 2015. Massive-scale tree modelling from TLS data. ISPRS Ann. Photogramm. Remote Sens. Spat. Inf. Sci. 2, 189.
Reymann, C., Lacroix, S., 2015. Improving LiDAR point cloud classification using intensities and multiple echoes, in: 2015 IEEE/RSJ International Conference on Intelligent Robots and Systems (IROS). Presented at the 2015 IEEE/RSJ International Conference on Intelligent Robots and Systems (IROS), pp. 5122–5128. https://doi.org/10.1109/IROS.2015.7354098
Richardson, J.J., Moskal, L.M., Bakker, J.D., 2014. Terrestrial Laser Scanning for Vegetation Sampling. Sensors 14, 20304–20319. https://doi.org/10.3390/s141120304
Ross, C.W., Loudermilk, E.L., Skowronski, N., Pokswinski, S., Hiers, J.K., O'Brien, J., 2022. LiDAR Voxel-Size Optimization for Canopy Gap Estimation. Remote Sens. 14, 1054. https://doi.org/10.3390/rs14051054
Roussel, J.-R., Auty, D., 2021. Airborne LiDAR Data Manipulation and Visualization for Forestry Applications. R package version 3.1. 2.
Roussel, J.-R., Auty, D., Coops, N.C., Tompalski, P., Goodbody, T.R., Meador, A.S., Bourdon, J.-F., De Boissieu, F., Achim, A., 2020. lidR: An R package for analysis of Airborne Laser Scanning (ALS) data. Remote Sens. Environ. 251, 112061.
Simoniello, T., Coluzzi, R., Guariglia, A., Imbrenda, V., Lanfredi, M., Samela, C., 2022. Automatic Filtering and Classification of Low-Density Airborne Laser Scanner Clouds in Shrubland Environments. Remote Sens. 14, 5127. https://doi.org/10.3390/rs14205127
Simonson, W.D., Allen, H.D., Coomes, D.A., 2014. Applications of airborne lidar for the assessment of animal species diversity. Methods Ecol. Evol. 5, 719–729. https://doi.org/10.1111/2041-210X.12219
Soma, M., Pimont, F., Dupuy, J.-L., 2021. Sensitivity of voxel-based estimations of leaf area density with terrestrial LiDAR to vegetation structure and sampling limitations: A simulation experiment. Remote Sens. Environ. 257, 112354.
Song, J.-H., Han, S.-H., Yu, K.Y., Kim, Y.-I., 2002. Assessing the possibility of land-cover classification using lidar intensity data. Int. Arch. Photogramm. Remote Sens. Spat. Inf. Sci. 34, 259–262.
Teri, S.S., Musliman, I.A., 2019. MACHINE LEARNING IN BIG LIDAR DATA: A REVIEW. Int. Arch. Photogramm. Remote Sens. Spat. Inf. Sci. XLII-4-W16, 641–644. https://doi.org/10.5194/isprs-archives-XLII-4-W16-641-2019
Tymen, B., Vincent, G., Courtois, E.A., Heurtebize, J., Dauzat, J., Marechaux, I., Chave, J., 2017. Quantifying micro-environmental variation in tropical rainforest understory at landscape scale by combining airborne LiDAR scanning and a sensor network. Ann. For. Sci. 74, 32. https://doi.org/10.1007/s13595-017-0628-z
US Fish Wildlife Service, 2017. Species status assessment for the Canada lynx (Lynx canadensis) contiguous United States distinct population segment. Version 10 Oct. 2017 Lakewood Colo.
Vanbianchi, C., Gaines, W.L., Murphy, M.A., Pither, J., Hodges, K.E., 2017. Habitat selection by Canada lynx: making do in heavily fragmented landscapes. Biodivers. Conserv. 26, 3343–3361. https://doi.org/10.1007/s10531-017-1409-6

Venier, L.A., Swystun, T., Mazerolle, M.J., Kreutzweiser, D.P., Wainio-Keizer, K.L., McIlwrick, K.A., Woods, M.E., Wang, X., 2019. Modelling vegetation understory cover using LiDAR metrics. PLOS ONE 14, e0220096. https://doi.org/10.1371/journal.pone.0220096

Wallace, L., Hally, B., Hillman, S., Jones, S.D., Reinke, K., 2020. Terrestrial Image-Based Point Clouds for Mapping Near-Ground Vegetation Structure: Potential and Limitations. Fire 3, 59. https://doi.org/10.3390/fire3040059

Washington State Department of Natural Resources, n.d. Loomis State Forest Landscape Plan 1996. Available Online: https://www.dnr.wa.gov/publications/lm_loomis_sec4.pdf (Accessed on 25 August 2023).

Weiss, U., Biber, P., Laible, S., Bohlmann, K., Zell, A., 2010. Plant species classification using a 3D LIDAR sensor and machine learning, in: 2010 Ninth International Conference on Machine Learning and Applications. IEEE, pp. 339–345.

Wing, B.M., Ritchie, M.W., Boston, K., Cohen, W.B., Gitelman, A., Olsen, M.J., 2012. Prediction of understory vegetation cover with airborne lidar in an interior ponderosa pine forest. Remote Sens. Environ. 124, 730–741. https://doi.org/10.1016/j.rse.2012.06.024

Woods, M., Lim, K., Treitz, P., 2008. Predicting forest stand variables from LiDAR data in the Great Lakes – St. Lawrence forest of Ontario. For. Chron. 84, 827–839. https://doi.org/10.5558/tfc84827-6

Xu, D., Wang, H., Xu, W., Luan, Z., Xu, X., 2021. LiDAR applications to estimate forest biomass at individual tree scale: Opportunities, challenges and future perspectives. Forests 12, 550.

Xu, Q., Li, B., McRoberts, R.E., Li, Z., Hou, Z., 2023. Harnessing data assimilation and spatial autocorrelation for forest inventory. Remote Sens. Environ. 288, 113488. https://doi.org/10.1016/j.rse.2023.113488

Yan, W.Y., Shaker, A., Habib, A., Kersting, A.P., 2012. Improving classification accuracy of airborne LiDAR intensity data by geometric calibration and radiometric correction. ISPRS J. Photogramm. Remote Sens. 67, 35–44. https://doi.org/10.1016/j.isprsjprs.2011.10.005

Zhao, K., Popescu, S., Meng, X., Pang, Y., Agca, M., 2011. Characterizing forest canopy structure with lidar composite metrics and machine learning. Remote Sens. Environ. 115, 1978–1996. https://doi.org/10.1016/j.rse.2011.04.001

Zheng, G., Ma, L., Eitel, J.U.H., He, W., Magney, T.S., Moskal, L.M., Li, M., 2017. Retrieving Directional Gap Fraction, Extinction Coefficient, and Effective Leaf Area Index by Incorporating Scan Angle Information From Discrete Aerial Lidar Data. IEEE Trans. Geosci. Remote Sens. 55, 577–590. https://doi.org/10.1109/TGRS.2016.2611651

Zong, X., Wang, T., Skidmore, A.K., Heurich, M., 2021. The impact of voxel size, forest type, and understory cover on visibility estimation in forests using terrestrial laser scanning. GIScience Remote Sens. 58, 323–339. https://doi.org/10.1080/15481603.2021.1873588

Chapter 5. Conclusion

This research utilized fine scale remote sensing techniques to advance research on the quantification of forest structure and condition. Topics of research were: water content of sensed leaf litter measured by terrestrial lidar; using drone digital aerial photogrammetry to construct three dimensional models of fire effects within a forest; and using terrestrial lidar to quantify understory forest structure related to species habitat and to upscale the measurements to landscape level using xgboost machine learning techniques. This work is about the application and use of novel remote sensing techniques from fine scale sensors applied to a variety of cases. Remote sensing as a science can be interdisciplinary, offering infinite collaboration opportunities with researchers across a multitude of disciplines. Understanding and applying remote sensing solutions to ecological questions at different scales can offer important new insights and allow for analysis that would otherwise be impossible. For example, three topics that were not directly related to each other were addressed within this dissertation, but applications of fine scale remote sensing techniques allowed for further investigation into areas that represent current knowledge gaps and advanced the understanding and ability quantify structure and condition.

In chapter 2, terrestrial lidar was used to quantify the moisture content of dead leaf fuel beds using the mean and standard deviation of the intensity values within a defined area. The accuracy of the models varied based on the distance from the scanner and the type of lidar unit used (time-of-flight vs. phaseshift). This method paper was conducted within a laboratory, but the findings show the promise of terrestrial lidar to be used to rapidly sample fuel moisture. While terrestrial lidar units are stationary, the same principles can be applied to mobile lidar units or drone lidar. This research represents advancements in the ability to utilize spectral values from an active sensor to quantify an important condition (i.e., moisture content) of vegetation, while also capturing information about the structural arrangement. Moisture content within this chapter was primarily considered as an indicator for flammability but applications of this work go beyond fire. The use of lidar for evaluation of vegetation health due to water stress and detection of fine variability in water levels across a spatial extent are both future avenues for continued research.

For chapter 3, the creation of multispectral point clouds using dDAP allowed for the quantification of fire effects at strata of different heights based on the change in spectral reflectance values. This work addressed current gaps in knowledge primarily regarding aerial and satellite

imagery's tendency to underestimate fire severity when live overstory vegetation is present. Complete classification of ground cover classes was done with a high level of accuracy and NDVI values from multispectral point clouds were calculated to quantify the change in NDVI pre- and post-fire. Some of the conclusions from this study were that fire effects were greatly diminished above 6 m in the forest canopy, that a comprehensive classification of ground cover below 2 m was possible even in areas directly underneath tree canopies, and that removing overstory vegetation from orthoimages greatly increased the level of fire effects detected. This study was primarily an exploration of methods utilizing multispectral dDAP to quantify fire effects. This research provides a method for quantifying fire effects three-dimensionally with a level of spatial precision that is not possible with traditional field protocols. The next steps in this research could include monitoring vegetation regrowth post-disturbance with centimeter precision to determine the effects of fine-scale differences in fire severity and topography on revegetation. Drone imagery can also be acquired across large areas and be processed to digitally remove the overstory for fine-scale mapping of understory ground cover and to provide a more robust estimate of ground fire effects.

The final research goal in chapter 4 was to utilize terrestrial lidar to quantify understory horizontal cover, and then use that data to inform a landscape model using aerial lidar data. The exploratory methods of this study assessed 42 different metrics from terrestrial lidar and 286 metrics from aerial lidar to determine which model inputs provided the most robust model for determining areas that met habitat requirements for Canada lynx. The ecological applications of these new methods were the production of a map with ordinal classes of high cover, low cover, and no cover, in relation to the viewshed and vegetation structure at 1.5 m above ground. XG boost machine learning algorithms produced a model with 85% accuracy, demonstrating that aerial lidar can effectively be used to quantify understory vegetation structure with a level of precision previously unobtainable.

Novel methods and applied models were developed for moisture content measurements, understory fire effect monitoring, and horizontal cover estimates. The diversity and interdisciplinary nature of the topics addressed in this work demonstrate the broad applicability of remote sensing to quantify ecological processes and changes at a scale where they are directly measurable.

Chapter 6. Appendices

6.1 Chapter 2 Supplemental Material

Table 6.S2.1 *Coefficient (slope) values for all control samples using the linear broken stick model. The break was at 100% moisture content for the fabric mesh and 40% moisture content for the pine board samples. Coefficients that varied significantly from the coefficients of 0o are bolded, with level of significance denoted by number of *.*

Sample	Moisture	FARO 0^o	RIEGL 0^o	FARO 45^o	RIEGL 45^o	FARO 90^o	RIEGL 90^o
FM 3M	<100%	-0.000464	-0.000580	-0.000410	-0.000513	-0.000434	-0.000517
	>100%	-0.000153	-0.000207	-0.000164	-0.000189	-0.000161	**-0.000180***
FM 6M	<100%	-0.000557	-0.000608	-0.000544	-0.000555	**-0.000502***	-0.000519
	>100%	-0.000086	-0.000158	-0.000130	-0.000169	**-0.000132****	**-0.000164****
FM 9M	<100%	-0.000628	-0.000698	-0.000545	-0.000595	-0.000509	-0.000565
	>100%	0.000023	-0.000165	-0.000048	-0.000181	**-0.000062***	**-0.000172***
FM 12M	<100%	-0.000609	-0.000638	-0.000545	-0.000576	-0.000493	-0.000542
	>100%	-0.000022	-0.000157	-0.000115	-0.000184	-0.000109	**-0.000175***
PB 3M	<40%	-0.000906	-0.000547	-0.000733	-0.000443	-0.000727	-0.000470
	>40%	-0.003306	-0.003258	**-0.003135***	-0.003014	-0.003170	-0.002551
PB 6M	<40%	-0.000649	-0.000375	-0.000736	-0.000495	-0.000596	-0.000436
	>40%	-0.003522	-0.003263	-0.003071	-0.002908	**-0.003883****	**-0.003548***
PB 9M	<40%	-0.001110	-0.000468	-0.001155	-0.000571	-0.000801	-0.000288
	>40%	-0.003409	-0.003337	-0.003388	-0.003330	**-0.003370****	**-0.003665****
PB 12M	<40%	-0.001111	-0.000407	-0.001102	-0.000537	-0.000855	**-0.000342***
	>40%	-0.001716	-0.002437	-0.001739	-0.002306	**-0.002567****	**-0.002776****

Table 6.S2.2 *A comprehensive table of the coefficients and R2 values for the non-normalized data.*

Distance	Scanner	Moisture Content	Intensity	DF	PP	LLP	SRO	FM 0	FM 45	FM 90	PB 0*	PB 45*	PB 90*
ALL	FARO	< 100%	Mean	-328.04	121.897	29.99583	-190.408	-68.0624	-69.9728	-159.384	-35.4124	-65.7588	219.5456
			SD	9683.698	1745.224	1726.546	4527.125	4666.219	4790.478	4481.968	137.1439	485.7037	684.8512
			R^2	0.2968	0.07787	0.03368	0.3939	0.5646	0.5785	0.6744	0.2761	0.08249	0.179
		>100%	Mean	-226.853	-166.625	-227.312	-476.774	-205.586	-397.64	-864.387	-18.858	-27.9871	-64.317
			SD	2517.893	339.8042	487.424	-1214.55	1654.981	6068.273	6165.594	321.785	275.6903	231.696
			R^2	0.2488	0.1454	0.1545	0.3904	0.01365	0.328	0.419	0.4251	0.4344	0.4466
	RIEGL	< 100%	Mean	-1482.1	-146.65	-485.4	-1181	-1001	-775.64	-362.525	-83.965	-194.285	-81.53
			SD	8969.6	444.35	-43.06	1885.7	1508.35	3225.215	4534.335	330.445	1118.495	777.17
			R^2	0.4424	0.2287	0.03945	0.3237	0.7867	0.784	0.7576	0.03519	0.1675	0.09777
		>100%	Mean	-595.305	-537.35	-557.57	-1156.85	-2745.5	-2669.2	-1709.1	-32.1	-41.3765	-43.06
			SD	1921.575	-297.65	-146.75	101.51	3279.5	4817.8	5075.1	360.36	318.1845	301.295
			R^2	0.5995	0.5743	0.5605	0.7887	0.4777	0.6476	0.5165	0.4546	0.4797	0.4241
3M	FARO	< 100%	Mean	-1419.31	177.537	165.2163	-337.969	-372.605	-110.592	-170.328	-240.681	-261.063	-178.749
			SD	14743.37	4797.235	9433.907	6387.827	5138.907	4998.693	4803.265	1122.533	922.3864	508.3628
			R^2	0.7544	0.2556	0.5304	0.8111	0.7414	0.5703	0.656	0.1703	0.2145	0.0994
		>100%	Mean	-816.022	-549.945	-740.524	-1171.46	-2316.37	-2342.58	-2357.99	-316.867	-60.7519	-57.3145
			SD	2062.057	546.9962	-1534.26	-296.419	6075.187	6979.584	7215.514	272.4921	239.7635	253.7587
			R^2	0.6844	0.4953	0.5866	0.7819	0.3872	0.6764	0.7345	0.4319	0.4736	0.4426
	RIEGL	< 100%	Mean	-3390.55	-204.05	7441.3	-1419.9	-1368.7	-1284.95	-1426.35	-185.6	-406.7	-259.65
			SD	5222.2	3120.15	7651.1	5392.05	1084.3	1977.7	1380.35	845.45	1894.15	1406.35
			R^2	0.798	0.1274	0.3581	0.7817	0.9076	0.8687	0.906	0.0778	0.2531	0.1245
		>100%	Mean	-901.6	-776.9	-825.55	-1287	-3649.9	-3746.65	-3811.67	-42.005	-63.685	-55.06
			SD	1890.8	-1356.15	-1431.95	-642.45	4701	4439.85	4337.25	316.19	301.46	359.635
			R^2	0.7797	0.7731	0.7575	0.877	0.7644	0.8346	0.8594	0.458	0.5231	0.4917
6M	FARO	< 100%	Mean	-667.288	67.86253	-465.338	-411.959	-354.976	-236.323	-428.311	-187.498	-324.567	-274.235
			SD	14022.05	1679.36	3923.608	4823.613	4279.632	4229.792	3911.811	725.7457	1348.272	859.4391
			R^2	0.508	0.05564	0.1344	0.5169	0.8106	0.6948	0.8232	0.09245	0.3064	0.2087
		>100%	Mean	-687.505	-504.889	-622.264	-1003.88	-1657.41	-2240.02	-2865.56	-34.7275	-52.2486	-80.4782
			SD	953.9748	-470.057	-989.626	-366.674	4842.783	6412.698	6039.142	328.0404	306.2923	265.9779
			R^2	0.5231	0.4723	0.5205	0.7381	0.1843	0.592	0.7069	0.5401	0.5609	0.5887
	RIEGL	< 100%	Mean	-2563.45	-138.05	-747	-1744.3	-1180.35	-1007.45	-1102.1	-168.4	-282.65	-252.95
			SD	10253.65	1034.75	1626.5	3590	1598.7	2581.6	2320.7	784.9	1410.65	1146
			R^2	0.6858	0.03539	0.1171	0.5534	0.925	0.8919	0.8908	0.04901	0.2155	0.1836
		>100%	Mean	-665.25	-655.4	-763.7	-1202.35	-3088.5	-3358.3	-3757.85	-45.205	-52.555	-84.495
			SD	1255.4	-961.95	-1231.2	-166.1	4613	5382.65	4335.65	381.54	336.855	321.83
			R^2	0.6365	0.6653	0.7048	0.8325	0.5157	0.7892	0.8282	0.559	0.5322	0.5931
9M	FARO	< 100%	Mean	-345.833	490.8646	-50.6921	-409.928	-10.4464	20.73887	52.10112	-104.33	-132.874	-190.546
			SD	7636.943	2325.217	640.8438	4211.999	4957.798	5527.962	5322.473	599.022	722.8621	738.263
			R^2	0.2048	0.09837	0.009978	0.3417	0.6161	0.5598	0.6588	0.1015	0.1657	0.2007
		>100%	Mean	-119.341	-215.843	-437.708	-1008.76	214.9908	-578.028	-749.404	-172.36	-38.6662	-72.1224
			SD	2104.001	68.97664	-222.102	1250.918	-296.092	6398.542	5283.185	369.5575	286.7528	204.8
			R^2	0.1366	0.1239	0.2259	0.5474	-0.02204	0.3258	0.2996	0.4879	0.5093	0.426
	RIEGL	< 100%	Mean	62.7	187.7	-704.5	-1468.6	-1160.05	-2518.9	-1121.5	-185.95	-214.685	-417.25
			SD	16086.2	1173.3	-412.25	3703.55	467.15	6701.4	1672.1	884.25	1317.53	1300.15
			R^2	0.3354	0.004904	0.02348	0.3944	0.8527	0.645	0.829	0.07544	0.2004	0.2837
		>100%	Mean	-640.4	-623.45	-715.95	-1150.45	-3216.55	-3356	-3730.15	-29.57	-44.005	-83.35
			SD	468.35	-1016.8	-919.85	-110.7	3975.85	5185	4320.1	397.485	323.915	197.01
			R^2	0.6647	0.6093	0.7434	0.8205	0.5285	0.7729	0.8196	0.4864	0.5027	0.4415
12M	FARO	< 100%	Mean	-227.574	330.3014	12.22574	-197.755	-171.803	-51.5768	-32.0799	-58.5433	-122.946	-188.58
			SD	6751.027	1829.11	-288.234	2615.837	3165.618	5062.263	5510.726	237.5287	847.0528	663.5848
			R^2	0.1452	0.07803	0.00146	0.1662	0.3025	0.5128	0.6545	0.04119	0.162	0.1779
		>100%	Mean	12.77624	-108.298	-358.908	-903.774	-168.002	-929.595	-827.49	-9.73537	-19.8738	-64.1794
			SD	3522.56	407.8305	-348.258	781.6151	343.212	5987.238	5437.26	340.6037	257.2124	210.4492
			R^2	0.2153	0.06623	0.159	0.5263	0.003819	0.3821	0.3579	0.2815	0.3296	0.3628
	RIEGL	< 100%	Mean	-3019	-3.24	-481.75	-1272	-1274.3	-1085.15	-1232.65	-124.05	-209.225	-578.85
			SD	7687.5	509.365	-281.6	647.05	966.95	2449.85	1708.8	524.95	1345.46	1273.8
			R^2	0.5518	0.01399	0.00388	0.19	0.8831	0.8381	0.8492	0.02969	0.1826	0.3304
		>100%	Mean	-738	-600.6	-597.05	-1140.7	-3379.1	-3468.95	-3815.4	-22.13	-26.655	-65.28
			SD	312.75	-779.55	-719.6	-499.2	2577.1	5150.2	4027.5	357.935	302.87	232.7
			R^2	0.728	0.5829	0.7502	0.8099	0.4946	0.7935	0.8226	0.3176	0.3805	0.4197

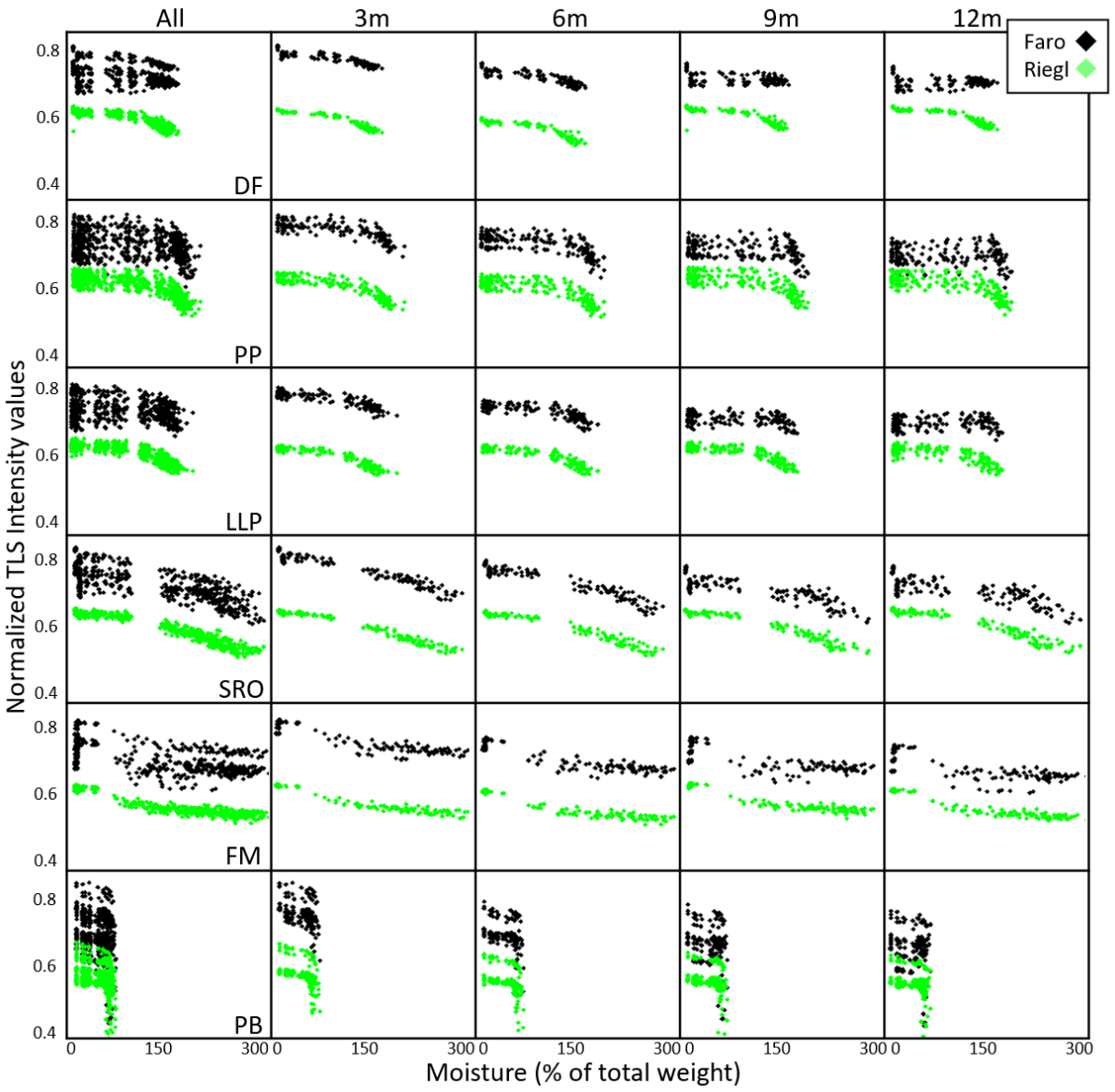

Figure 6.S2.1 *Mean intensity values of all samples across all distances. There was more variability in the intensity returns at different distances with the FARO PS compared to the RIEGL TOF.*

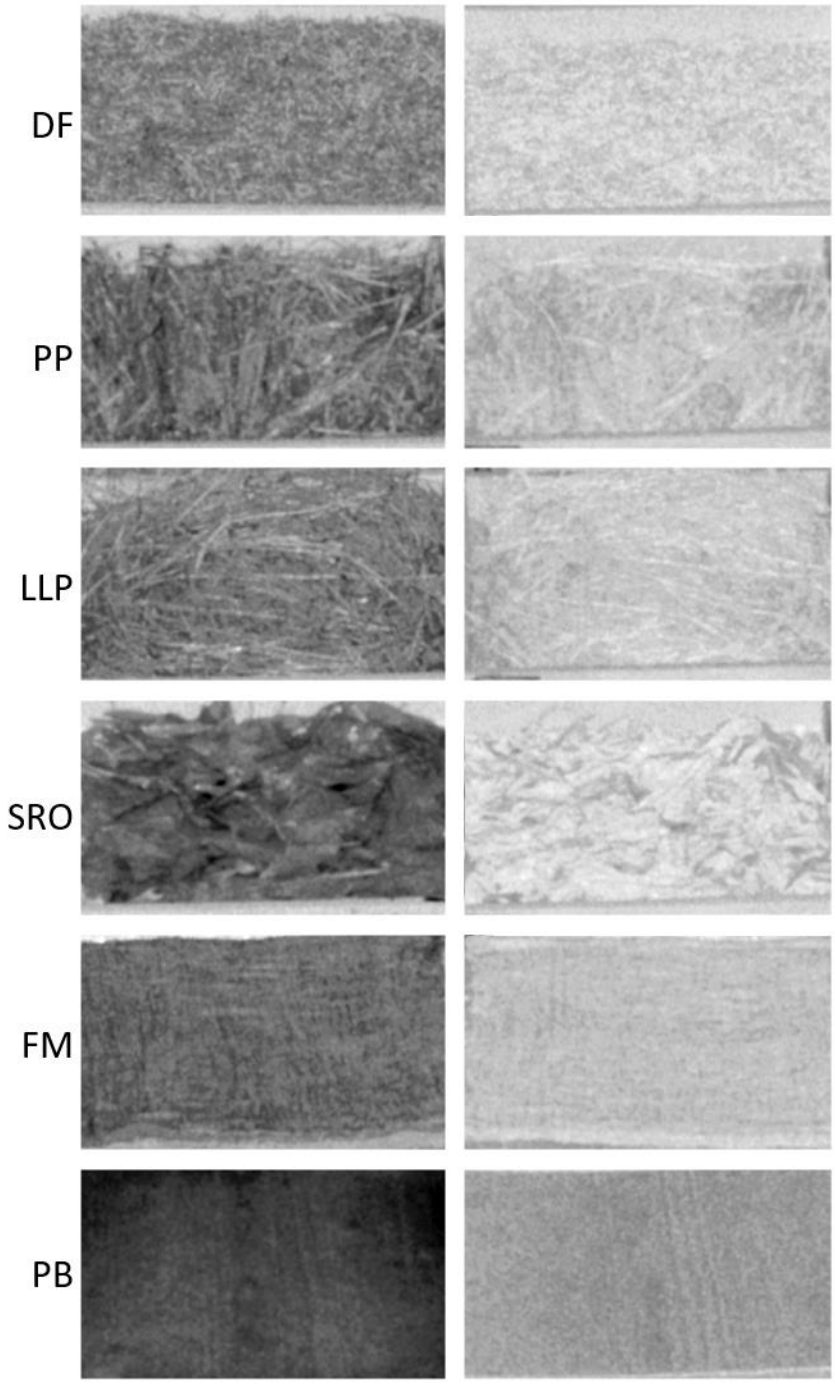

Figure 6.S2.2 *Images produced from the FARO laser scanner of a representative of each sample type fully saturated and after having been oven dried. Samples reflected more energy when dry and were more homogeneous in reflectance values.*

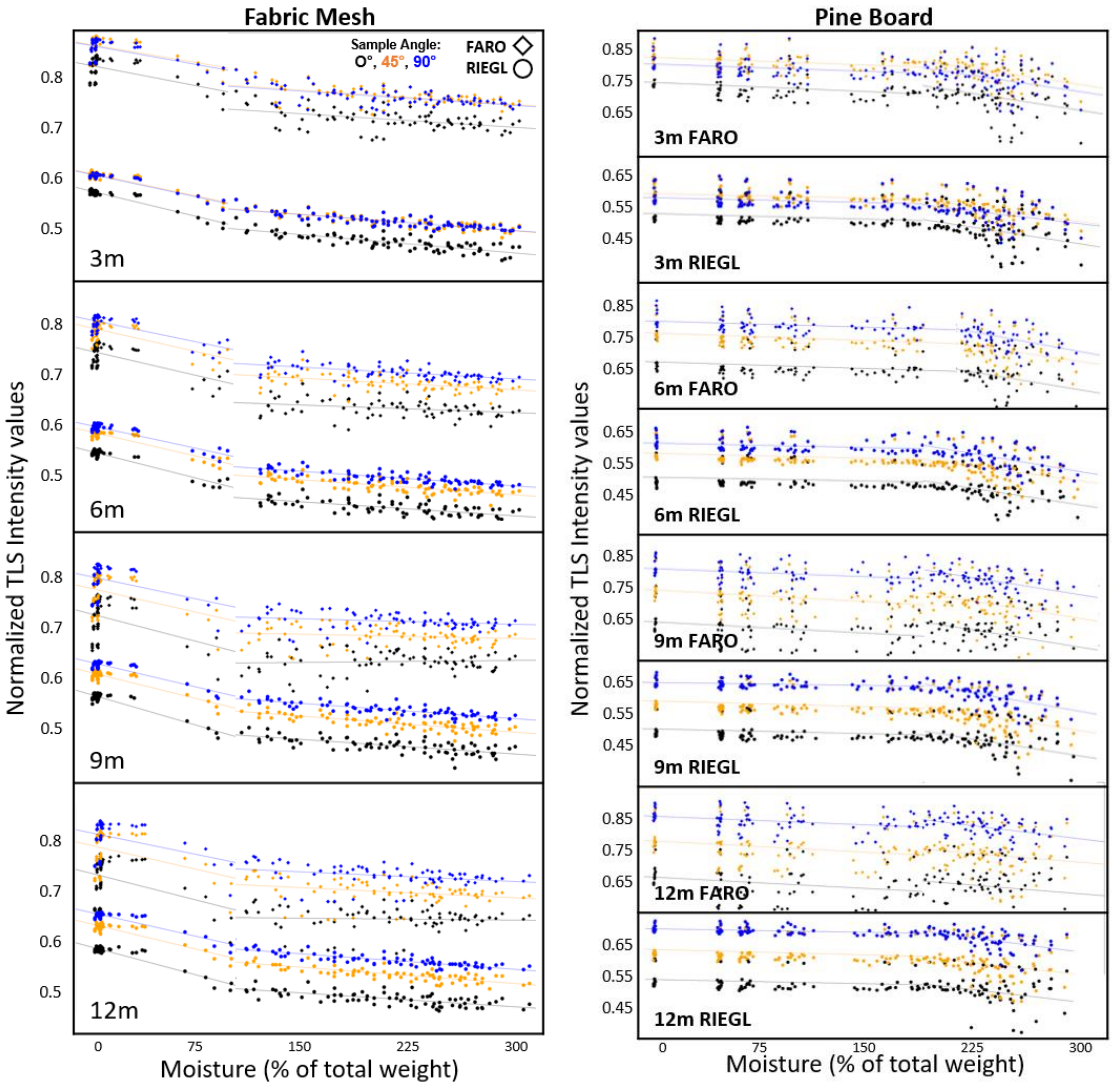

Figure 6.S2.3 *Scatter plot of all control samples at the three different angles relative to the ground. General data trends held for all data with the samples placed at 45o and 90o even though samples at these angles returned a greater amount of energy compared to the samples at 0o. REIGL and FARO fabric mesh samples are plotted on the same y axis as there was a visible separation of the data, while the pine board values were separated due to a large overlap in the points.*

6.2 Chapter 3 Supplemental Material

Plot 1(Burned)

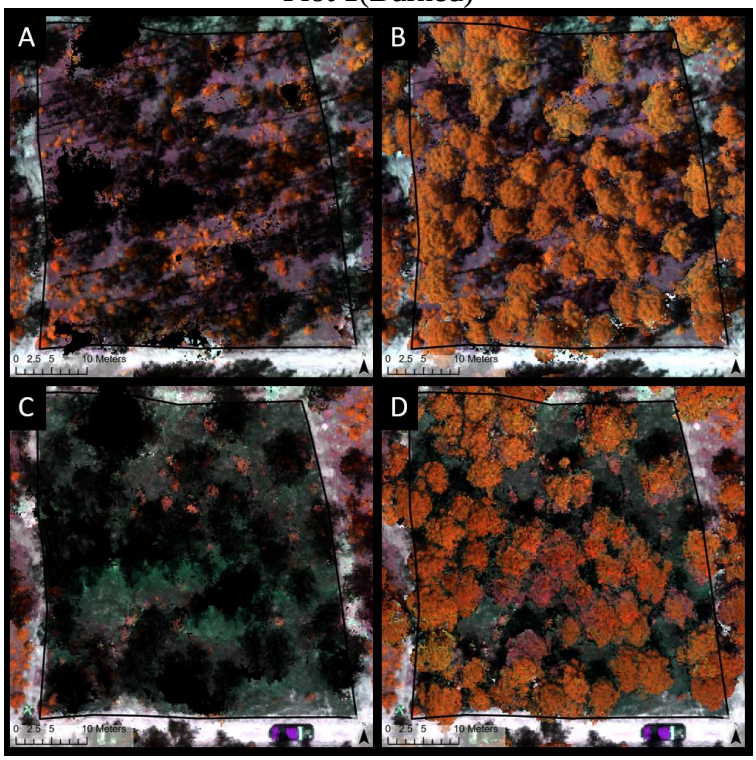

Plot 2 (Control)

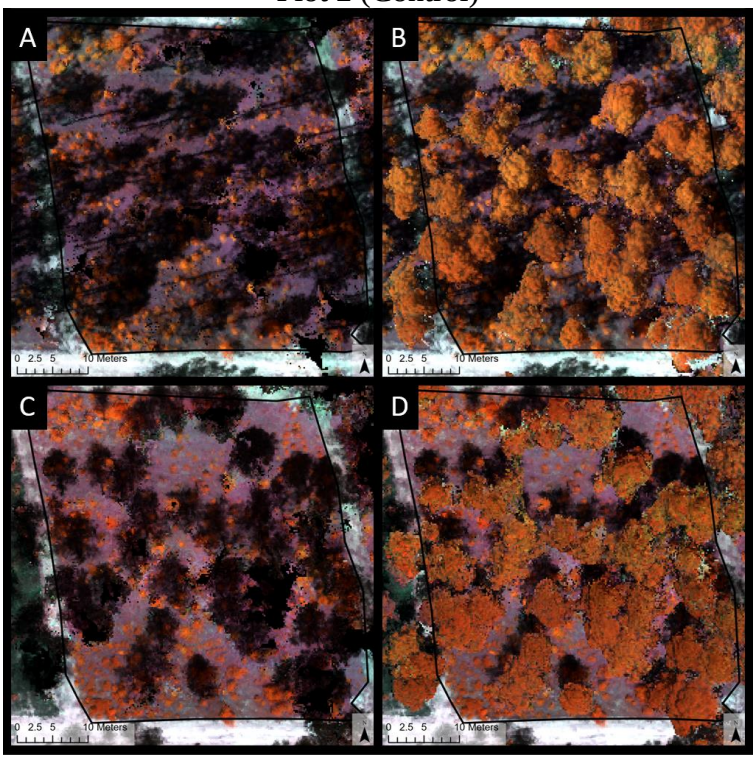

Plot 3 (Control)

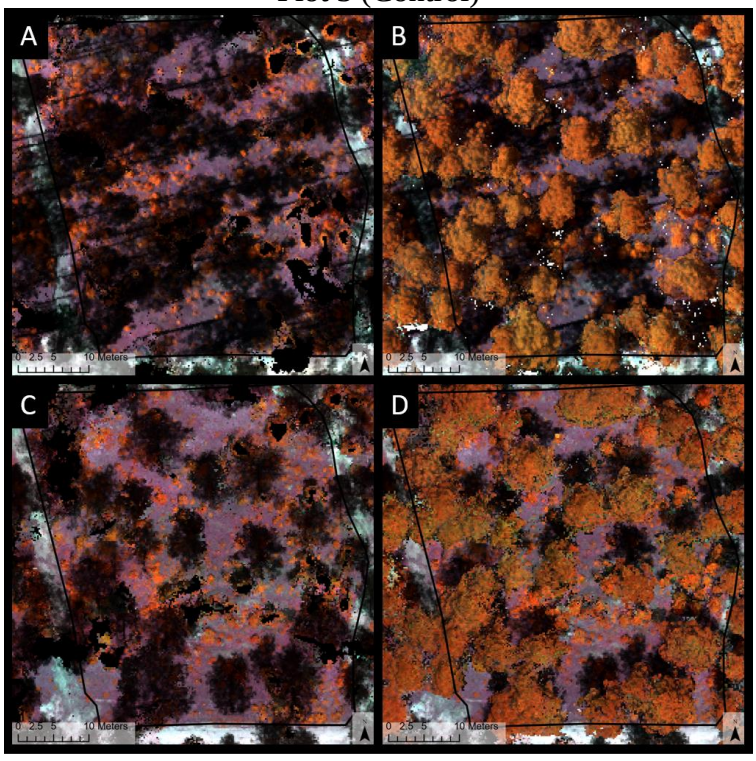

Plot 5 (Burned)

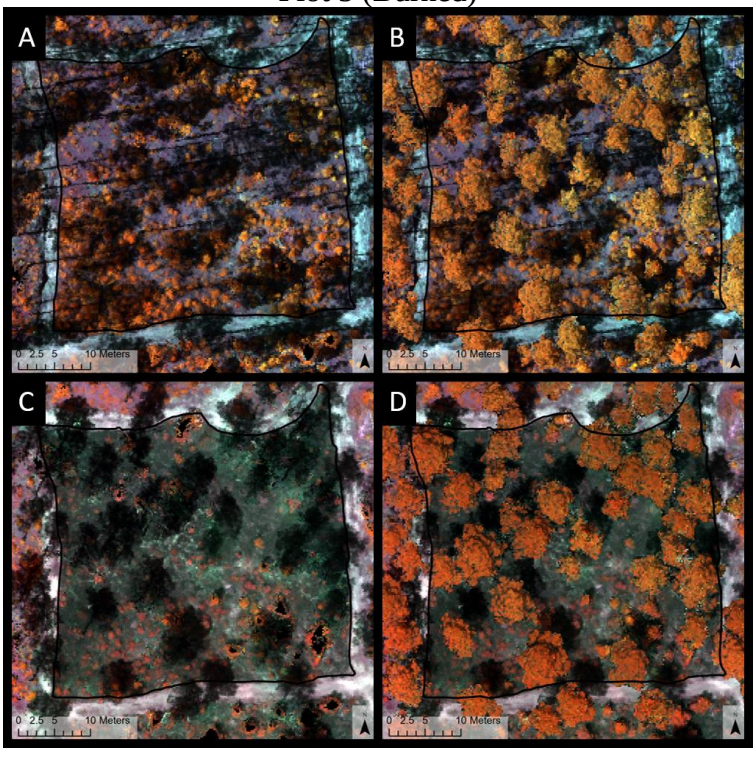

Plot 6 (Burned)

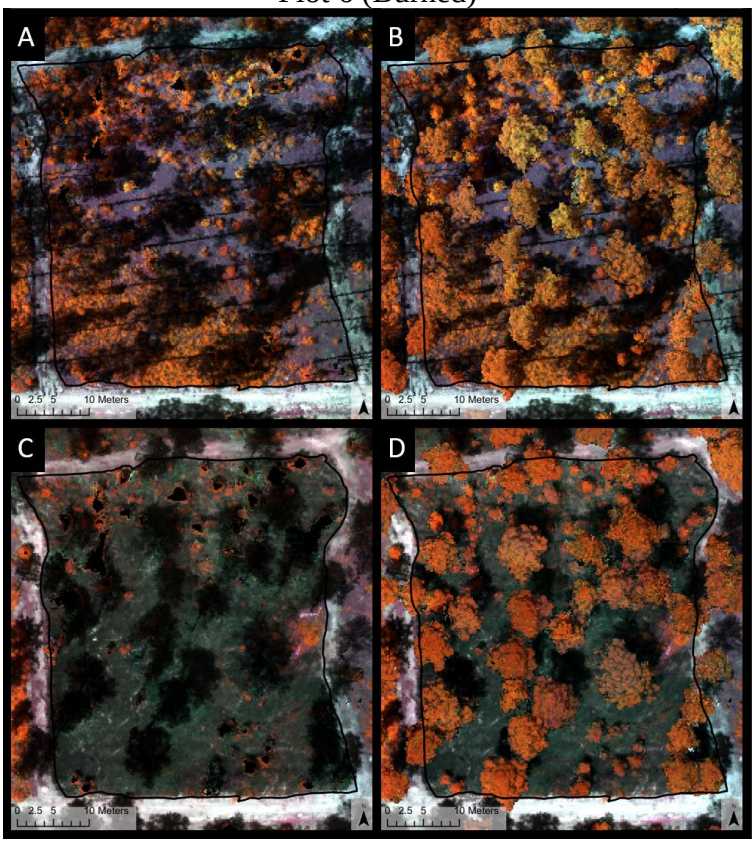

Plot 24A (Burned)

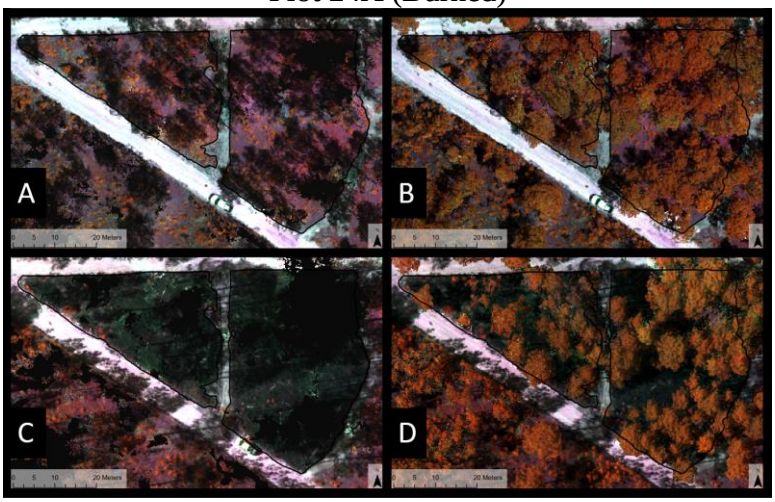

Plot 24B (Burned)

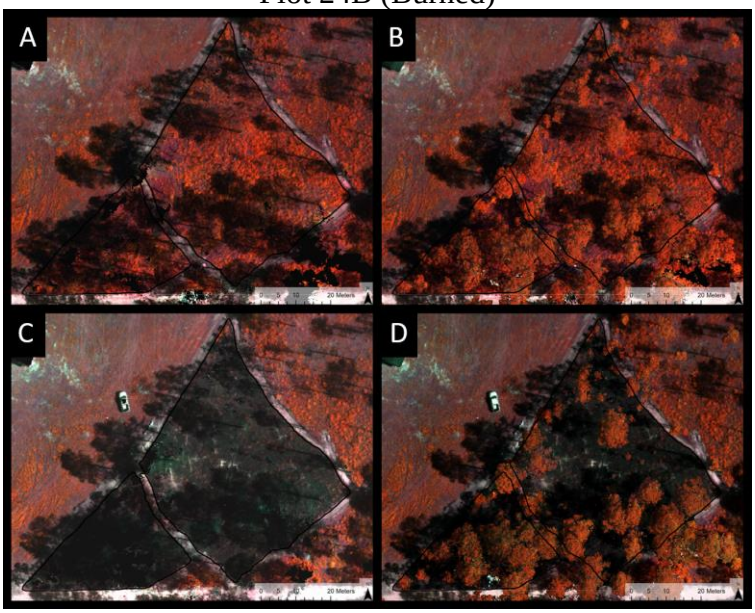

Figure 6.S3.4. *20 cm resolution color infrared orthoimages produced from multispectral photogrammetric point clouds of the 7 plots. A: Understory only pre-burn, B: Top-down pre-burn, C: Understory only post-burn, D: Top-down post-burn.*

Plot 1

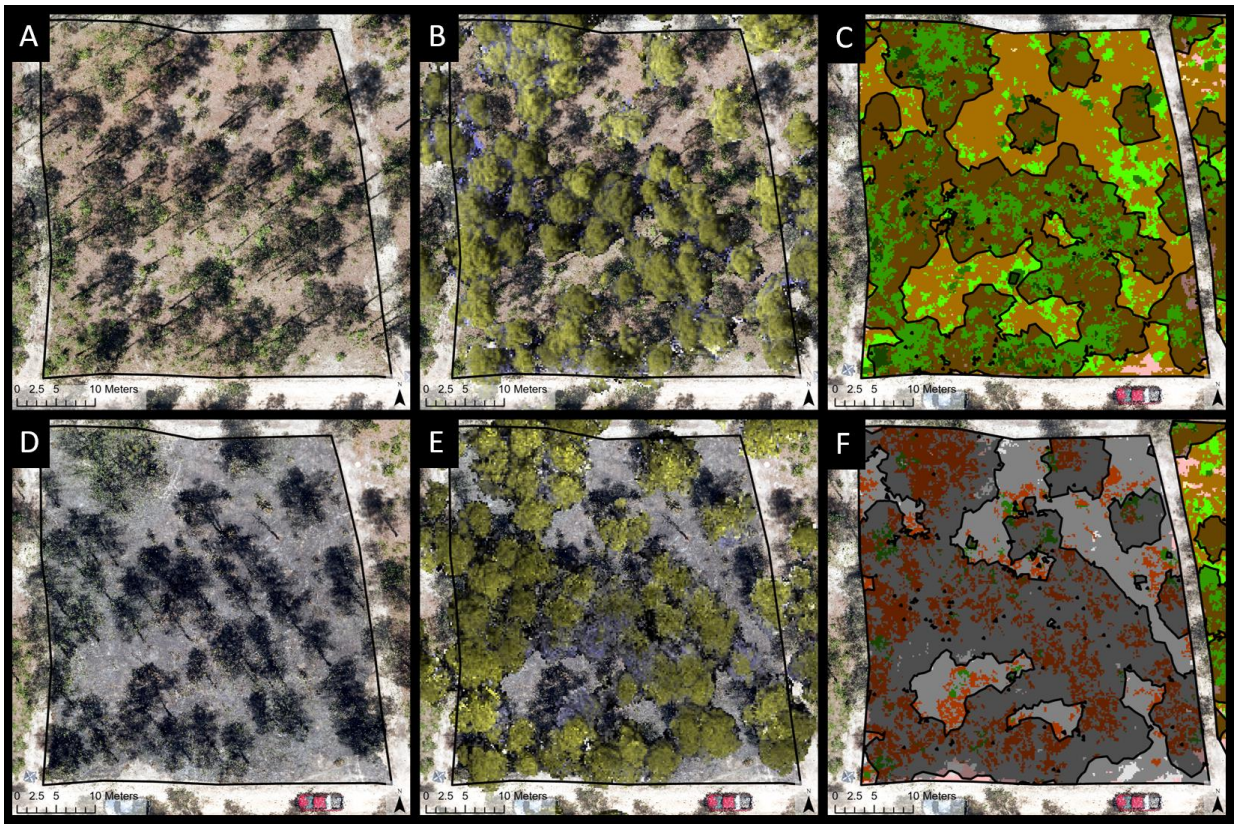

Plot 2

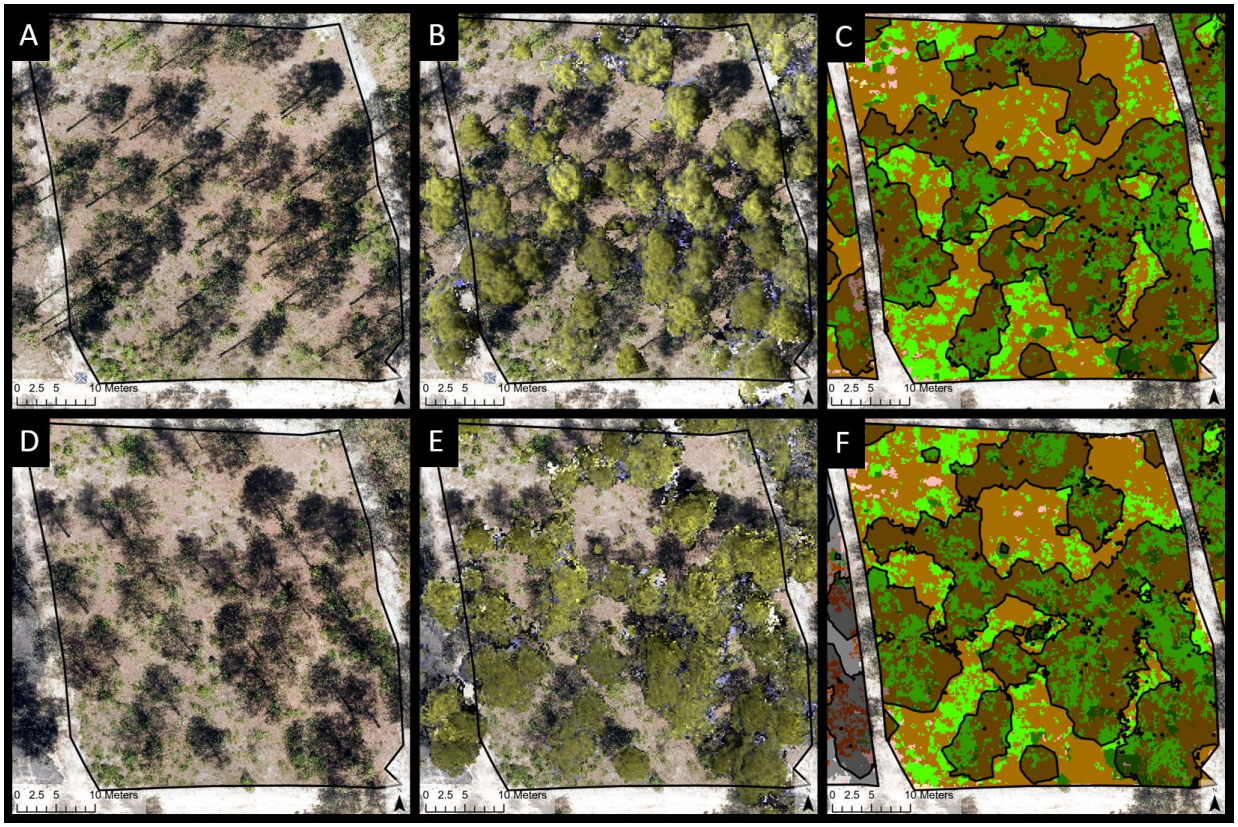

Plot 3

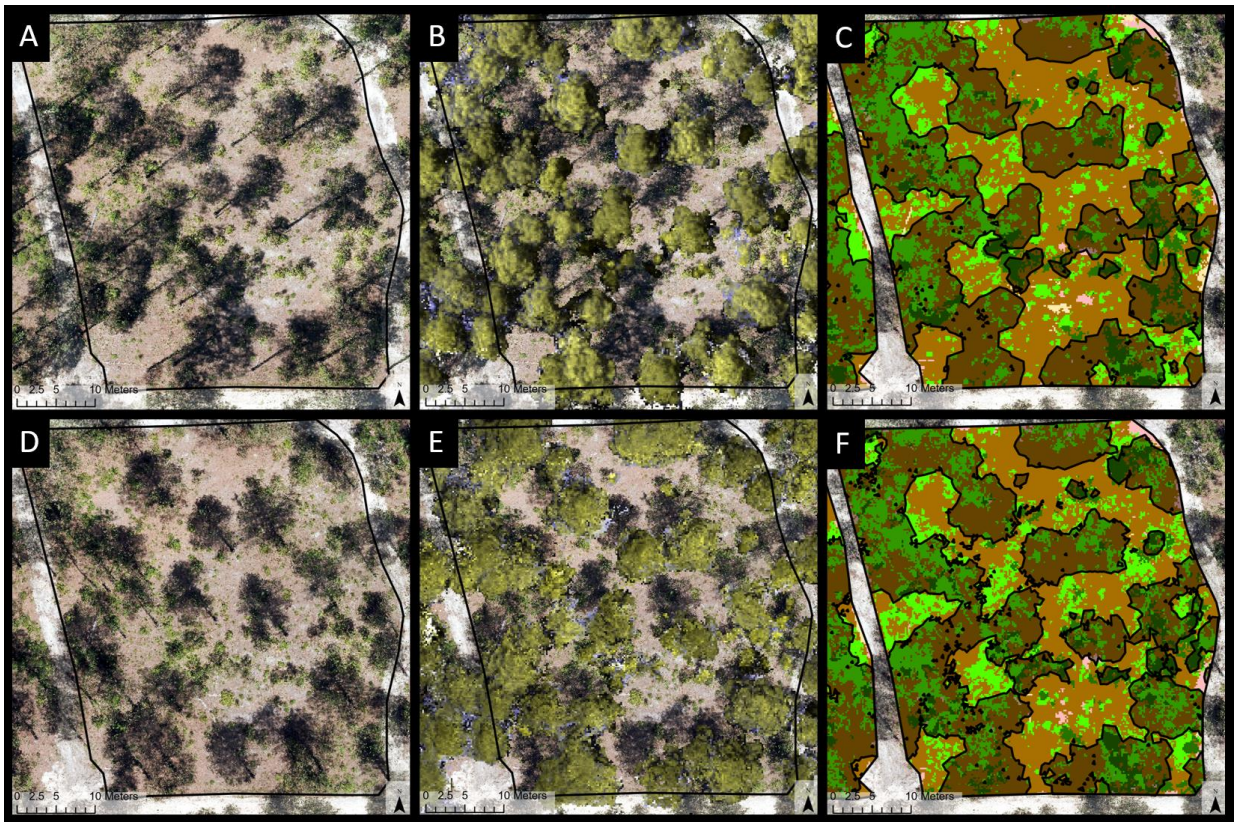

Plot 5

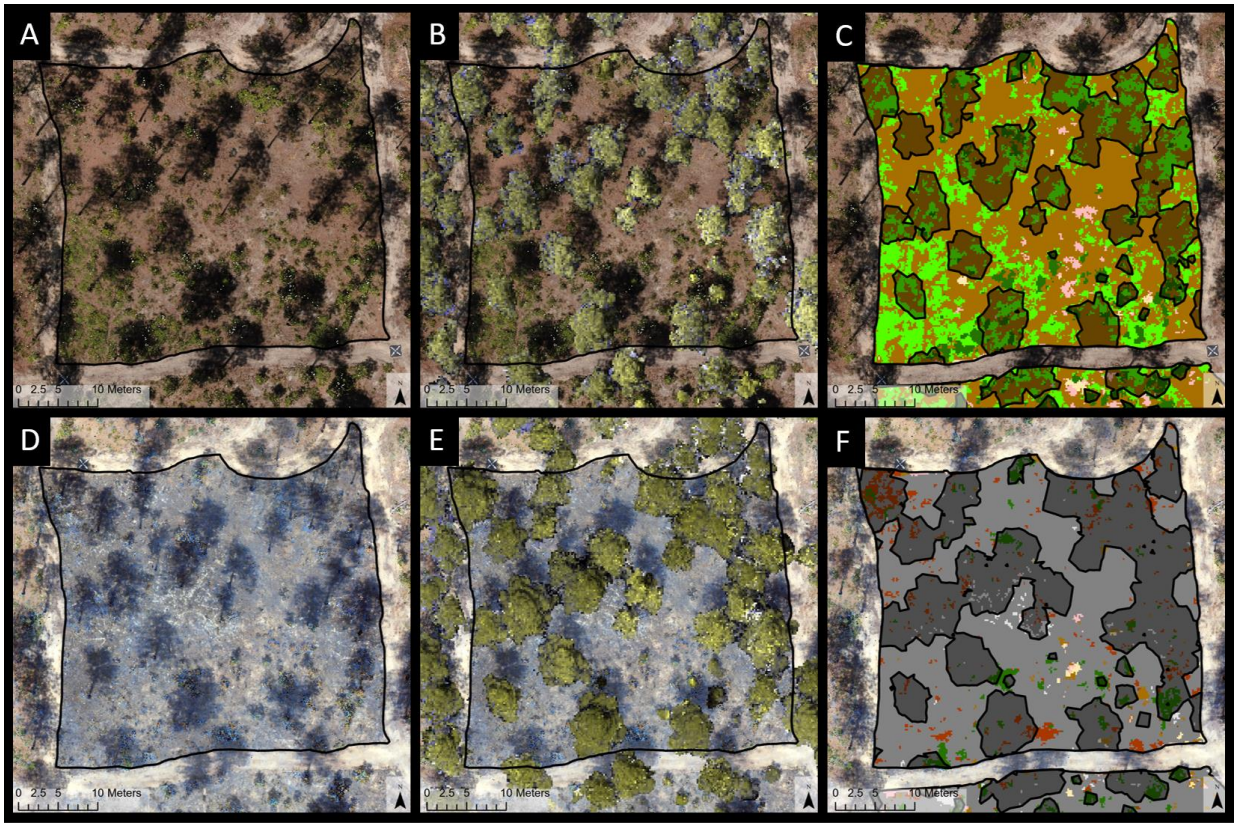

Plot 6

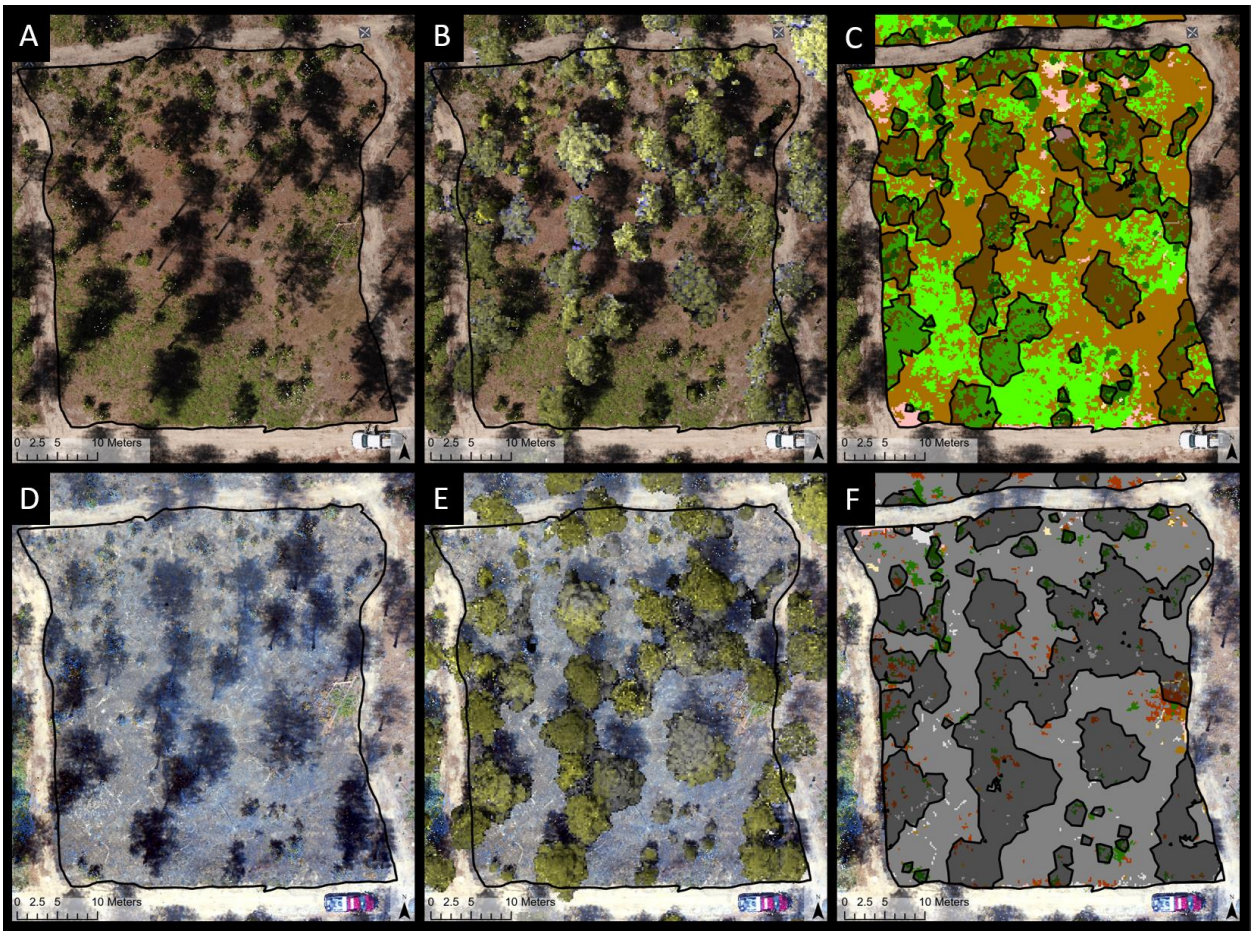

Plot 24A

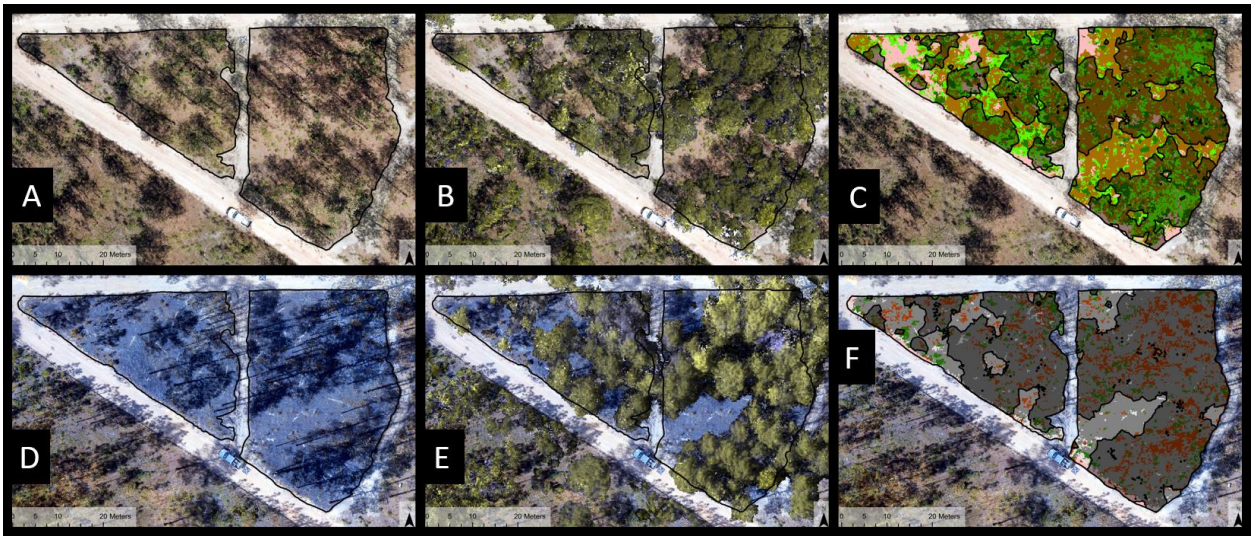

Plot 24B

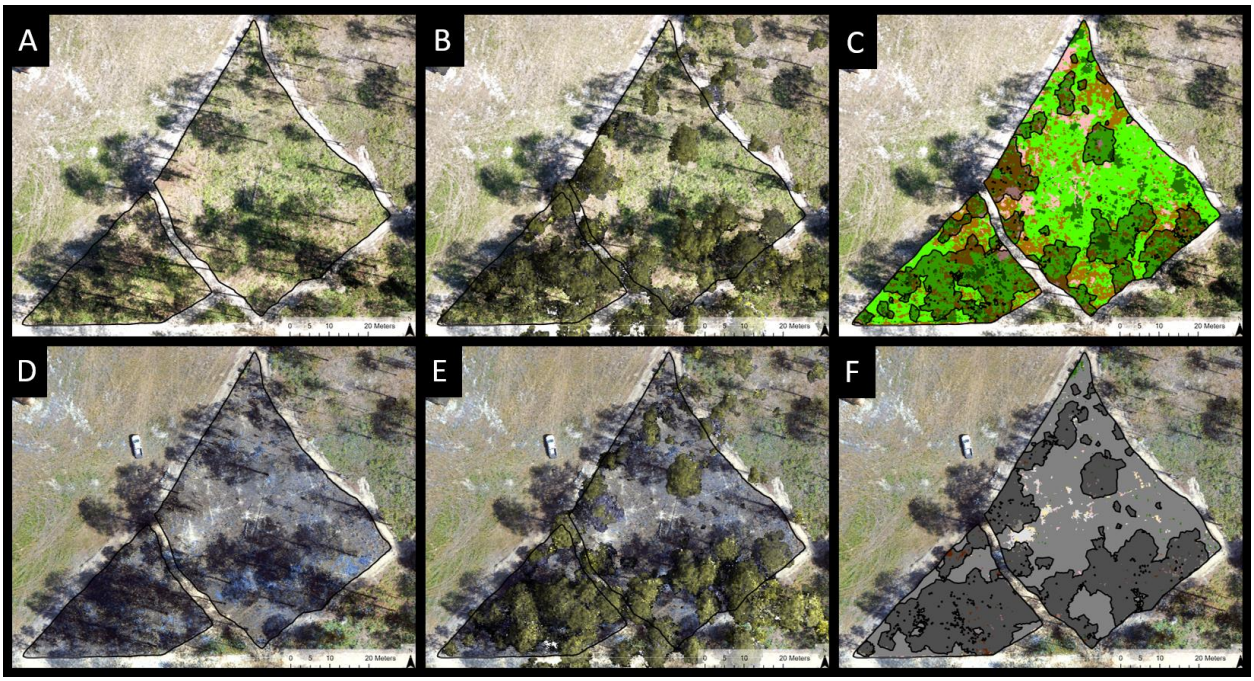

Figure 66.S3.5. *5 cm resolution RGB orthoimages produced from photogrammetric point clouds of the 7 plots. A: Pre-burn below 2m, B: Pre-burn top down (20 cm resolution upper canopy model), C: Classified understory only image from pre-burn orthoimage, D: Post-burn below 2m, E: Post-burn top down (20 cm resolution upper canopy model). F: Classified understory only image from post-burn orthoimage.*

VITA

Jonathan is a self-identified remote sensing nerd that dabbles in fire ecology, wildlife habitat characterizations, and restoration processes. They specialize in fine-scale remote sensing technologies such as drone-based digital aerial photogrammetry and terrestrial lidar. Trees, drones, and lidar points galore! Using fine-scale remote sensing techniques to quantify processes and change at a local level to then develop models for landscape-level characterization of vegetation structure regarding fire effects and habitat. Most of their work is taking characterizations of forest structure from field sampled remote sensing techniques and upscaling them to a landscape level using aerial lidar, aerial imagery, and satellite imagery.

Teaching was a significant part of Jonathan's PhD journey as they did course development and teaching at University of Washington and were faculty at Western Washington University and Evergreen State College. Jonathan has had the honor of teaching well over a thousand students across 16 different courses while working toward this dissertation.